NMR Spectroscopy and Imaging of Hyperpolarized Gases: Fundamental Aspects and Applications

Dissertation zur Erlangung des Grades

"Doktor der Naturwissenschaften"

am Fachbereich Physik
der Johannes Gutenberg-Universität
in Mainz

Paul-Philipp Zänker
geboren in Marburg an der Lahn

Mainz 2007

Tag der mündlichen Prüfung: 17.07.2007

Contents

Abbreviations

BG	**B**uffer **G**as
COSY	**CO**rrelation **S**pectroscop**Y**
CPMG	**C**arr **P**urcell **M**eiboom **G**ill sequence to measure T_2
CRAZED	**C**OSY **R**evamped by **A**symmetric **Z**-Gradient **E**cho **D**etection
DDF	**D**istant **D**ipolar **F**ield
DMSO	**D**i**M**ethyl **S**ulf**O**xide
DQ	**D**ouble **Q**uantum
EPR	**E**lectron **P**aramagnetic **R**esonance
EXSY	**EX**change **S**pectroscop**Y**
FID	**F**ree **I**nduction **D**ecay
FLASH	**F**ast **L**ow **A**ngle **S**hot
FOV	**F**ield **O**f **V**iew
FT	**F**ourier **T**ransformation
HP	**H**yper**P**olarized
iDQC	**I**ntermolecular **D**ouble **Q**uantum **C**oherence
iMQC	**I**ntermolecular **M**ultiple **Q**uantum **C**oherence
MEOP	**M**etastable **E**xchange **O**ptical **P**umping
MRI	**M**agnetic **R**esonance **I**maging
NMR	**N**uclear **M**agnetic **R**esonance
OP	**O**ptical **P**umping
PP	**P**oly**P**ropylene

PU	**P**oly**U**rethane
ppm	**P**arts **P**er **M**illion
r.f.	**R**adio **F**requency
SE	**S**pin **E**cho
SEOP	**S**pin **E**xchange **O**ptical **P**umping
SQC	**S**ingle **Q**uantum **C**oherence
SNR	**S**ignal-to-**N**oise **R**atio
TPPI	**T**ime **P**roportional **P**hase **I**ncrement

Chapter 1

Introduction

Over the 60-year history since the discovery of the *nuclear magnetic resonance* (NMR) phenomenon, by Bloch and Purcell [Bloch 46, Purcell 46], countless NMR techniques have been developed that are considered today as indispensable tools in physics, chemistry, biology, and medicine. The technique best known to the public is *magnetic resonance imaging* (MRI), which has become a standard, noninvasive diagnostic tool in modern hospitals. The contribution of Mansfield and Lauterbur to its development was recognized by the Nobel prize in medicine 2003 [Mansfield 77, Lauterbur 73]. Furthermore, NMR spectroscopy is an essential method to study structure and dynamics of molecules in solution, but also to characterize the bulk and surface properties of materials. With the help of modern Fourier Transform (FT) NMR experiments, structures of large molecules can be determined, e.g. proteins with molecular weights up to 80 kDa [Tugarinov 02]. Ernst and Wüthrich were also awarded the Nobel prizes in chemistry 1991 and 2002, respectively for their contribution to this field [Ernst 92, Wüthrich 03].

However, conventional NMR methods suffer from the drawback of a notorious lack of sensitivity, which limits their applicability in many circumstances. This fundamental insensitivity originates from the minuscule size of the nuclear magnetic moments, resulting in exceedingly small equilibrium spin polarizations, even in the strongest available magnetic fields. Therefore, in recent years several different, *hyperpolarization* (HP) techniques were developed to prepare spin systems in highly polarized spin states. This work focuses on the increasingly applied method of optical pumping of noble gases [Kastler 50, Bouchiat 60], which enhances the sensitivity in NMR

spectroscopy and MRI up to five orders of magnitude.

With ^{3}He and ^{129}Xe, two noble gases with different characteristics are available for various applications in magnetic resonance. ^{3}He is perfectly inert and therefore an ideal contrast agent for imaging of void spaces, especially in physiological environments e.g. in lung imaging [Middleton 95, Ebert 96, Kauczor 96]. Here, the influence of the fast translational diffusion of the ^{3}He particles plays a major role [Kadlecek 05, Conradi 06]. Especially the effect of motion on the *spin echo* (SE) phenomenon in the gas phase has not been studied in detail yet, due to experimental restrictions. The SE was first discovered by Hahn in 1950 [Hahn 50], and provides today the basis of numerous pulse sequences in NMR and MRI. The influence of spin motion on the SE signal, caused by diffusion or other dynamical processes, has already been subject of many studies in liquid and solid state [Carr 54, Stejskal 65, Collignon 81]. In these motional regimes, the effect of dynamics is usually well understood and described within a theoretical framework. By the usage of HP gases and a self-constructed setup, which allows a precise variation of the diffusion coefficient, a detailed examination of the SE signal under the influence of the fast motion in gases is now possible for the first time. The measurements show a strong, time-dependent suppression of the SE signal with increasing diffusion. An extension of the usual theory to arbitrary times, describes the observed effect. The understanding of this phenomenon is of general theoretical interest, also, it is a prerequisite for different applications, e.g. imaging sequences using SEs in MRI of HP gases, for which diffusion suppression used to be one of the major obstacles.

Another fundamental effect, which is reported for the first time in this thesis, is the detection of couplings between distant spins in the gas phase. The existence of such *intermolecular* couplings in liquids was first verified in the early 90's [He 93, Warren 93] and required, in consequence, a correction of the conventional NMR theory at that time. It was shown that the unexpected couplings arise from a *distant dipolar field* (DDF), that a single spin experiences from the sum of the magnetic moments of numerous spins at a certain distance. The resulting *intermolecular multiple-quantum coherences* (iMQCs) have been explored for biomedical spectroscopic and imaging purposes resulting in several novel applications [Warren 98, Zhong 04]. However, both the theoretical basis and issues re-

lated to the practical implementation are fields of current research. Numerous works have been published concerning the effect of diffusion on the iMQCs [Barros Jr. 06, Ardelean 00, Chen 01b]. As diffusion coefficients in liquids are small and cannot be varied easily, studying iMQCs in the gas phase is interesting, because here the diffusivity is much higher and can be changed over several orders of magnitude. Nevertheless, to detect iMQCs in gases, different obstacles have to be overcome. With the employment of HP ^{3}He and the gained knowledge concerning the influence of fast diffusion on echo signals, the first measurements of intermolecular double-quantum coherences (iDQCs) in the gas phase were accomplished.

The second part of this work focuses on the development of a new method to dissolve HP ^{129}Xe, with different possible applications in biomedical MRI and NMR spectroscopy. In contrast to ^{3}He, the highly polarizable electron cloud of the large ^{129}Xe atom brings along two useful properties: First, the chemical shift of ^{129}Xe is extremely sensitive to its environment, second, ^{129}Xe is lipophilic and thereby soluble in different kinds of biologically compatible liquids. Unlike conventional MRI contrast agents, which cannot pass membranes in the body due to their large size [Brasch 83, Sorensen 97, Caravan 99], ^{129}Xe atoms are small enough to pass such barriers, such as the blood-brain barrier or blood-gas barrier in the lung. This makes HP ^{129}Xe an interesting candidate for a new, free diffusive MRI contrast agent [Goodson 99], which can enhance the functional contrast of brain images [Swanson 97, Duhamel 01], and is also suited for angiography [Goodson 97, Möller 99]. On the other hand, NMR spectroscopy of dissolved ^{129}Xe has also gained considerable interest, as ^{129}Xe serves as an extremely sensitive, zero-background probe for studying chemical properties and structures, such as guest-host interactions [Song 97], novel microporous systems [Soldatov 04], surfaces [Raftery 91], and most importantly biomolecules [Rubin 00, Landon 01, Lowery 05]. Most of these studies are carried out in solutions, particularly in aqueous solutions.

In both cases, the dissolution process of HP ^{129}Xe is the main obstacle for the feasibility of these experiments. Therefore, a method was developed in this work, which improves this process, thus simplifying the preparation of contrast agents and permitting new, even two-dimensional spectroscopic experiments. The method also takes advantage of the recently developed

continuous flow gas polarizers [Haake 97, Shah 00].

Therefore, the present thesis covers both new fundamental and applied aspects from the broad field of magnetic resonance in HP gases, hereby also combining different disciplines of research.

Chapter 2

Fundamentals

This chapter describes the theoretical fundamentals which are needed to understand the experiments and results of the presented thesis. The topics are covered in many different text books and further information can be found in [Abragam 61, Ernst 87, Callaghan 91, Haacke 99, Blümich 00, Levitt 01]. The chapter is divided in five subsections. First, the basic principles of nuclear magnetic resonance (NMR) will be explained, as well as the different important interactions on spins in a magnetic field. Section 2.2 deals with one of the most important application of NMR, magnetic resonance imaging (MRI), especially focusing on imaging of gases. The basics of particle diffusion, and its measurement by NMR, will be described in Section 2.3, while Section 2.4 explains the production of hyperpolarized (HP) noble gases, paying special attention to ^{3}He and ^{129}Xe. Section 2.5 will conclude this chapter in describing the effect of large magnetizations in NMR experiments in liquids, which lead to the formation of a distant dipolar field (DDF) between the spins and renders possible the excitation and detection of intermolecular multiple quantum coherences (iMQCs) in liquids and in gases.

2.1 NMR fundamentals

NMR is based upon a quantum mechanical property of the nuclei: the *spin*. The spin is an intrinsic angular momentum of elementary particles which is not produced by a rotation of the particle itself, but is rather a property like the mass or the electric charge. The spin of a nucleus $\mathbf{I}$ results from the

spins of its constituents (protons and neutrons), which have a spin quantum number of 1/2. Each nucleus with a non-zero spin possesses a magnetic moment $\boldsymbol{\mu}$, which is given by

$$\boldsymbol{\mu} = \gamma\hbar\mathbf{I}\,, \tag{2.1}$$

where $\hbar = h/2\pi$ is Planck's constant, and γ is the magnetogyric ratio, which is characteristic for each isotope of every element. The behavior of a spin system is described quantum mechanically by the time-dependent Schrödinger equation

$$\frac{\mathrm{d}}{\mathrm{d}t}|\Psi(t)\rangle = -i\hbar\mathcal{H}(t)|\Psi(t)\rangle\,. \tag{2.2}$$

The evolution of the state $|\Psi(t)\rangle$ is determined by the Hamilton operator $\mathcal{H}(t)$ which describes the energy of the system. For a nucleus in a static magnetic field the majority of the spin interactions can be expressed in terms of the nuclear spin Hamiltonian

$$\mathcal{H} = \mathcal{H}_Z + \mathcal{H}_{rf} + \mathcal{H}_{DD} + \mathcal{H}_{cs} + \mathcal{H}_J + \mathcal{H}_Q\,, \tag{2.3}$$

where $\mathcal{H}_Z$ is the Zeeman interaction with the external magnetic field, and $\mathcal{H}_{rf}$ is the radio frequency interaction, which are both externally applied. $\mathcal{H}_{DD}$ is the direct dipole-dipole coupling between spins, $\mathcal{H}_{cs}$ the chemical shift interaction, $\mathcal{H}_J$ the indirect spin-spin coupling, which is mediated by the electron spins and $\mathcal{H}_Q$ the quadrupolar coupling. All of these are internal spin interactions and therefore intrinsic to the material being studied.

2.1.1 External spin interactions

When spins are placed into an external magnetic field $\mathbf{B}_0$, they align within the field. The energy, and therefore the Zeeman Hamiltonian, is equal to

$$E = \mathcal{H}_Z = -\boldsymbol{\mu}\cdot\mathbf{B}_0 = -\gamma\hbar\mathbf{I}\cdot\mathbf{B}_0\,. \tag{2.4}$$

If the direction of the magnetic field is chosen along the z-axis in the laboratory frame, $\mathbf{B}_0 = (0, 0, B_0)^T$, the different energy levels are

$$E_m = -\gamma m\hbar B_0\,, \tag{2.5}$$

with the magnetic quantum number m, which can take integral values as $|m| \leq I$, hereby defining the number of energy levels. For nuclei with $I = 1/2$,

two energy levels are allowed with an energy difference ΔE, which can be associated to a frequency ω_0

$$\Delta E = -\gamma\hbar B_0 = \hbar\omega_0 \,. \tag{2.6}$$

This *Larmor frequency* ω_0 is given by

$$\omega_0 = -\gamma B_0 \tag{2.7}$$

and determines the resonance frequency of a spin in a certain magnetic field. In the classical vector picture of NMR, it is also understood as the precession frequency of the nuclear magnetic moment $\boldsymbol{\mu}$ around the magnetic field direction $\mathbf{B}_0$.

The radio frequency (r.f.) coil generates a field $\mathbf{B}_{rf}$ along the x-axis of the laboratory frame. During an r.f. pulse the magnitude of this field oscillates at the spectrometer frequency ω,

$$\mathbf{B}_{rf}(t) = B_{rf}\cos(\omega t)\mathbf{e}_x \,, \tag{2.8}$$

where the maximum r.f. amplitude is denoted B_{rf}. Between the pulses, the r.f. field is equal to zero. It is useful to write this oscillation as the sum of two rotating components,

$$\mathbf{B}_{rf}(t) = \mathbf{B}^{rf}_{res}(t) + \mathbf{B}^{rf}_{non\ res}(t) \,. \tag{2.9}$$

The component rotating in the same sense as the spin precession is called the resonant component, while the one rotating in the opposite sense is called the non-resonant component of the r.f. field. The two components are given by

$$\mathbf{B}^{rf}_{res}(t) = \tfrac{1}{2}B_{rf}[\cos(\omega t)\mathbf{e}_x + \sin(\omega t)\mathbf{e}_y] \tag{2.10}$$

$$\mathbf{B}^{rf}_{non\ res}(t) = \tfrac{1}{2}B_{rf}[\cos(\omega t)\mathbf{e}_x - \sin(\omega t)\mathbf{e}_y] \,. \tag{2.11}$$

It can be shown, that under ordinary circumstances, the non-resonant component of the r.f. field has almost no influence on the spins and can be neglected. The factor $\frac{1}{2}$ arises because half of the r.f. field amplitude is 'wasted' on the non-resonant component, and it is often omitted by using $\mathbf{B}_1 = 2\,\mathbf{B}_{rf}$. The spin Hamiltonian due to the radio frequency interaction may therefore be written as

$$\mathcal{H}_{rf} \approx -\gamma\hbar B_1 \left[\cos(\omega t)\, I_x + \sin(\omega t)\, I_y\right] \,. \tag{2.12}$$

2.1.2 Internal spin interactions

The local magnetic field experienced by the nuclei varies on a submolecular level due to the magnetic field created by the surrounding electrons. Therefore, the resonance frequencies of different nuclei depend on their electronic environment, i.e. their chemical structure. This effect is called the *chemical shift*. It results from a two-step process: First, the external magnetic field $\mathbf{B}_0$ induces currents in the electron clouds of the molecule. Second, the circulating molecular currents in turn generate an additional magnetic field at the site of the nuclei. The induced field is, to a very good approximation, linearly dependent on the applied field and depends on the orientation of the molecule with respect to the magnetic field. The resultant local field is described by

$$\mathbf{B} = (1 - \boldsymbol{\sigma})\mathbf{B_0}\,, \tag{2.13}$$

where $\boldsymbol{\sigma}$ is the chemical shift tensor. The Hamiltonian for this interaction is expressed by

$$\mathcal{H}_{cs} = \gamma\hbar\mathbf{I}\cdot\boldsymbol{\sigma}B_0\,. \tag{2.14}$$

Since each nuclear spin features a magnetic moment, it generates a magnetic field which interacts directly with the other spins. This interaction is called the *through-space* or *direct dipole-dipole coupling*. The energy of this interaction is given by

$$E_{DD} = \frac{\mu_0}{4\pi}\left[\frac{\boldsymbol{\mu}_j\cdot\boldsymbol{\mu}_k}{r^3} - \frac{3(\boldsymbol{\mu}_j\cdot\mathbf{r})(\boldsymbol{\mu}_k\cdot\mathbf{r})}{r^5}\right]. \tag{2.15}$$

By inserting Eq. 2.1, the dipolar Hamiltonian is obtained,

$$\mathcal{H}_{DD} = \frac{\mu_0}{4\pi}\frac{\gamma_j\gamma_k\hbar}{r^3}\left(\mathbf{I}_j\mathbf{I}_k - \frac{3(\mathbf{I}_j\cdot\mathbf{r})(\mathbf{I}_k\cdot\mathbf{r})}{r^2}\right) \tag{2.16}$$

The *indirect spin-spin coupling* is mediated between nuclear spins by the binding electrons and is therefore usually much weaker than the dipole-dipole coupling. It is expressed by a coupling tensor $\underline{\mathbf{J}}_{jk}$ as

$$\mathcal{H}_J = \mathbf{I}_j\cdot\underline{\mathbf{J}}_{jk}\cdot\mathbf{I}_k\,. \tag{2.17}$$

As it is shown in Section 2.5, the dipole-dipole coupling is usually averaged out in liquids, while this 'J-coupling' remains, making it important in liquid state NMR spectroscopy.

The *quadrupolar coupling* term $\mathcal{H}_Q$ is only non-zero for spins with a spin quantum number $I > 1/2$. As this work exclusively deals with $I = 1/2$ nuclei (^{1}H, ^{3}He and ^{129}Xe), it is not further considered here.

2.1.3 The semi-classical picture and relaxation

In the semi-classical picture, the spin states are not examined individually on a microscopic quantum mechanical basis, but the time evolution of the macroscopic sum of all magnetic moments is described by the *magnetization* vector $\mathbf{M}$. Within this picture, simple experiments are easier to understand and to visualize.

The thermal equilibrium magnetization $\mathbf{M}_0$ for a spin ensemble with $I = 1/2$ in a static magnetic field at temperatures $T > 1$ K is calculated in the following. The populations N_+ and N_- of the two different energy states (see Fig. 2.1) are given by a Boltzmann distribution

$$\frac{N_+}{N_-} = e^{-\Delta E/kT} = e^{-\gamma\hbar B_0/k_B T} \tag{2.18}$$

with the Boltzmann constant k_B. The excess population is described by the *polarization* P

$$P = \frac{N_+ - N_-}{N_+ + N_-} = \frac{1 - e^{-\gamma\hbar B_0/k_B T}}{1 + e^{-\gamma\hbar B_0/k_B T}}\,. \tag{2.19}$$

With Eq. 2.18 and the "high temperature approximation" $\gamma\hbar B_0 \ll k_B T$ it is given by

$$P = \tanh\left(\frac{\gamma\hbar B_0}{2k_B T}\right) \approx \frac{\gamma\hbar B_0}{2k_B T}\,. \tag{2.20}$$

For a usual water sample in a magnetic field of 4.7 T at room temperature, the polarization of ^{1}H amounts to $P = 1.6 \cdot 10^{-5}$, which shows the validity of the approximation.

The macroscopic equilibrium magnetization $\mathbf{M}_0 = (0, 0, M_0)^T$ is then given by the sum of all magnetic moments

$$\mathbf{M}_0 = \sum_i^N \boldsymbol{\mu}_i = \tfrac{1}{2} N\gamma\hbar P \mathbf{e}_z\,, \tag{2.21}$$

where $N = N_+ + N_-$ is the total number of spins. When the spins are excited by an r.f. pulse close to the Larmor frequency, the number of spins

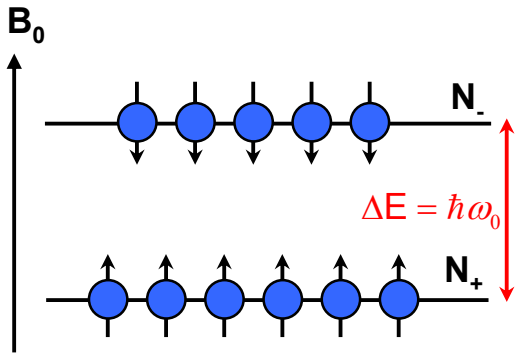

Figure 2.1: Population of the two distinct energy levels in a spin $I = 1/2$ ensemble. The orientation of the spins in the magnetic field depends on the magnetogyric moment of the nuclei. Depicted is the case of $\gamma > 0$ which is valid for ^{1}H but not for ^{3}He and ^{129}Xe ($\gamma < 0$).

in the respective energy levels change according to the Hamiltonian $\mathcal{H}_{rf}$ in Eq. 2.12. In the classical picture, the net magnetization $\mathbf{M}$ is affected by a torque $\boldsymbol{\tau} = \boldsymbol{\mu} \times \mathbf{B}$. The evolution of the magnetization was described first by Felix Bloch by the following equation of motion

$$\frac{\mathrm{d}\mathbf{M}}{\mathrm{d}t} = \gamma \mathbf{M}(t) \times \mathbf{B}(t) - \underline{\mathbf{R}} \cdot [\mathbf{M}(t) - \mathbf{M}_0] \,, \tag{2.22}$$

where $\mathbf{B}$ consists of both, the static magnetic field $\mathbf{B}_0$ and the oscillating r.f. field $\mathbf{B}_1$

$$\mathbf{B} = \begin{pmatrix} B_1 \cos(\omega t) \\ B_1 \sin(\omega t) \\ B_0 \end{pmatrix} \,, \tag{2.23}$$

and $\underline{\mathbf{R}}$ denotes as the relaxation matrix

$$\underline{\mathbf{R}} = \begin{pmatrix} 1/T_2 & 0 & 0 \\ 0 & 1/T_2 & 0 \\ 0 & 0 & 1/T_1 \end{pmatrix} \,. \tag{2.24}$$

The components of $\underline{\mathbf{R}}$ are called relaxation rates and are shortly described in the following: T_1 is the *longitudinal relaxation time*, and specifies the time for the magnetization to return into its thermal equilibrium state along the direction of the static magnetic field after the r.f. excitation. T_2 is called

transverse relaxation time and describes the loss of coherence of the the spin bundle in the transverse plane due to spin-spin interactions while rotating around the axis of the main field with the frequency ω_0.

In a coordinate system rotating with the frequency of the r.f. field ω around the z-axis the equations simplify, as the time dependence in $\mathbf{B}$ is vanishing for the effective field $\mathbf{B}_{eff}$ in the rotating frame. The effective field is calculated to be

$$\mathbf{B}_{eff} = \mathbf{B}_0 + \frac{\boldsymbol{\omega}}{\gamma} + \mathbf{B}_1 = \frac{\omega_0 - \omega}{\gamma}\,\mathbf{e}_z + \mathbf{B}_1\,. \tag{2.25}$$

For the resonance condition $\boldsymbol{\omega} = \boldsymbol{\omega}_0$, $\mathbf{M}_0$ rotates only around $\mathbf{B}_1$, while the duration t_p of the r.f. pulse determines the resulting angle α between $\mathbf{M}_0$ and $\mathbf{B}_0$. It is given by $\alpha = \omega \cdot t_p$, where α is referred to as the *flip angle*.

2.1.4 Free Induction Decay and NMR spectra

The simplest NMR pulse experiment is the detection of a Free Induction Decay (FID), which is shown in Fig. 2.2. The thermal equilibrium magnetization $\mathbf{M}_0$ is rotated into the xy-plane by a r.f. pulse along the y-axis with a flip angle α. The net magnetization $\mathbf{M}$ starts to precess around the z-axis with the Larmor frequency ω_0, and induces a current in the NMR coil, which is amplified and detected by the spectrometer. The signal is detected in the

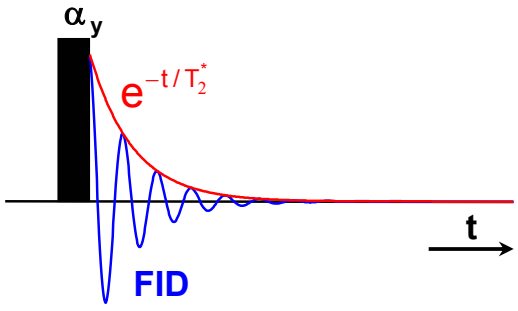

Figure 2.2: NMR pulse sequence to detect a Free Induction Decay (FID). The signal detected after the r.f. pulse with flip angle α along the y-axis is decaying with an exponential function. The relaxation time is denoted as T_2^*.

rotating frame of the r.f. irradiation and can be denoted as

$$M_{x'}(t) = M_0 \sin\alpha \cos(\Omega t)\, e^{-t/T_2^*} \quad (2.26)$$

$$M_{y'}(t) = M_0 \sin\alpha \sin(\Omega t)\, e^{-t/T_2^*}\,, \quad (2.27)$$

where $\Omega = \omega - \omega_0$ is the offset frequency. These equations can be easily combined to a complex notation,

$$M^+(t) = M_{x'}(t) + iM_{y'}(t) = M_0 \sin\alpha\, e^{(i\Omega - 1/T_2^*)t}\,. \quad (2.28)$$

The signal in a real experiment decays with the relaxation time T_2^* including inhomogeneous broadening which is approximated by

$$\frac{1}{T_2^*} = \frac{1}{T_2} + \frac{1}{T_2'} + \gamma\Delta B_0\,, \quad (2.29)$$

where T_2' is due to local changes in the magnetic susceptibility of the sample and $\gamma\Delta B_0$ are inhomogeneities of the external magnetic field. Therefore, T_2^* is much shorter than T_2 and depends mainly on the 'shim' (the homogeneity) of the static magnetic field. In our experiments T_2^* is typically of the order of tens of ms, while T_2 is in the range of seconds for water. Before the pulse sequence can be repeated for the sake of signal averaging, the magnetization has to return into its thermal equilibrium. This relaxation process is characterized by the time T_1. To ensure that the full magnetization is available again the repetition time of the experiment is usually chosen at least $5\,T_1$. The T_1 relaxation time can be measured by an inversion recovery experiment, as described in [Vold 68].

The NMR spectrum $S(\omega)$ is obtained from the time signal $s(t)$ by a Fourier transformation (FT)

$$S(\omega) = \int_{-\infty}^{+\infty} s(t) e^{-i\omega t} \mathrm{d}t \quad (2.30)$$

which reveals the different frequencies ω that are contained in the FID signal. Fig. 2.3 shows an acquired FID of an ethanol sample, as well as the FT of the data. As the protons in ethanol occur in three different chemical groups (–CH_3, –CH_2 and –OH), three peaks appear in the NMR spectrum with different chemical shifts. The amplitudes of the signals also reveal the correct ratio of the numbers of protons in the different positions (3:2:1).

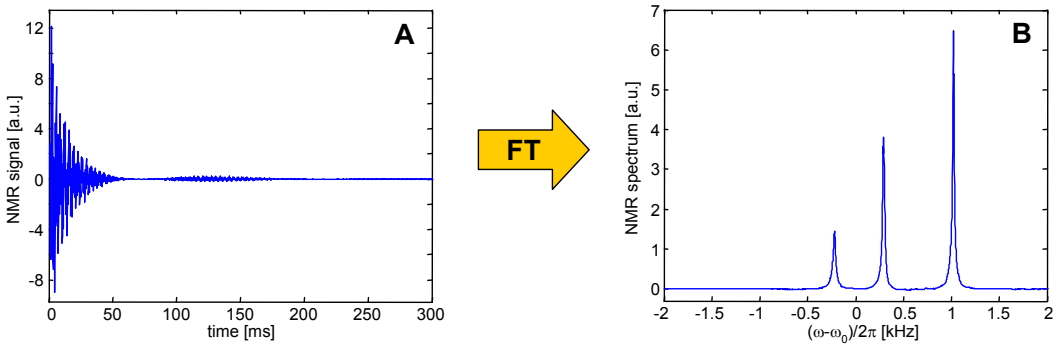

Figure 2.3: Procedure to obtain a NMR spectrum. **A:** Acquired time domain data (FID) of an ethanol sample at a frequency of 300 MHz. **B:** NMR spectrum of the sample, obtained by a Fourier transformation of the FID data. Three signals with different chemical shifts are detected.

2.1.5 Spin echo

A signal which has first vanished with time and then reappears is called an *echo*. In NMR the echo is associated with an inversion of the phases of all spins at a certain time τ which leads to a reappearing signal at the time of 2τ. This signal can be understood in terms of 'time running back wards' for a sufficiently isolated ensemble of spins. Since the discovery of the *Spin Echo* (SE) phenomenon by E. Hahn in 1950 [Hahn 50], many other echo sequences have been realized, not only in NMR spectroscopy, but also in magnetic resonance imaging (MRI).

The SE is generated by two pulses separated by a time τ (see Fig. 2.4). The first pulse is a 90°_y pulse, generating a FID signal which decays with T_2^*. The phase coherence between the different spin bundles, which evolve with the same frequency respectively (referred to as *spin isochromates*), is lost due to differences in local fields (see previous section). Thus, the vector sum of all magnetization components vanishes. However, as long as the precession frequency of each isochromate remains unchanged, a simple inversion of all phases at the time τ will generate a reoccurrence of the signal after another time τ. In the centre of the SE all magnetization components are refocused; although the respective precession frequencies differ. Therefore, the SE can also be observed in the presence of a static magnetic field gradient. The

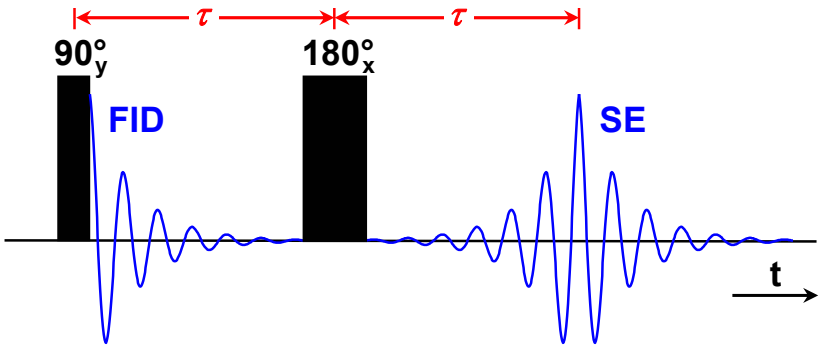

Figure 2.4: A two-pulse spin echo sequence, which refocuses the magnetization at time 2τ after the first pulse.

amplitude of the SE, without taking diffusion into account, is given by

$$A_{SE} = M_0 e^{-2\tau/T_2} \,, \tag{2.31}$$

as the relaxation by spin-spin interactions is not refocused. Thus, this sequence can also be used to measure the relaxation time T_2. This can also be accomplished in a single shot, if the magnetization is repeatedly refocused by 180° pulses. As a tribute to its inventors (Carr, Purcell, Meiboom and Gill) this technique is named the *CPMG sequence* [Carr 54, Meiboom 58].

2.1.6 Two-dimensional NMR experiments

The idea of two-dimensional (2D) NMR was first proposed by J. Jeener in 1972 [Jeener 72]. Since then it has evolved into one of the most important NMR techniques, in various applications and fields of research, also recognized by the Nobel prize for R. Ernst in 1991.

A two-dimensional data set is generated by introducing a second time variable t_1 in the pulse sequence before the detection period with time t_2. As shown in Fig. 2.5, the state excited in the first part of the experiment evolves during t_1, and is reconverted into a signal which is acquired in t_2, which is amplitude modulated depending on t_1. A set of FIDs is recorded with incremented t_1, and the two-dimensional NMR spectrum is obtained after Fourier transformation in both dimensions.

If phase sensitive detection is also needed in the indirect dimension (t_1), a suitable phase cycling scheme, which increments the phases of all excitation

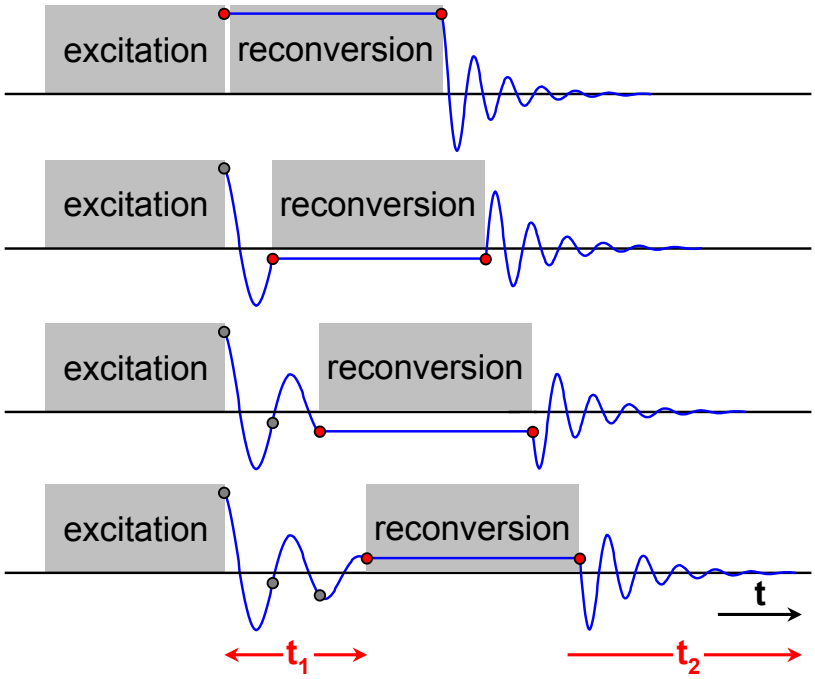

Figure 2.5: Schematic illustration of a two-dimensional NMR experiment. Excitation and reconversion blocks often consists of several pulses, their time is overemphasized in comparison to t_1 and t_2.

pulses, has to be applied. The principle of phase-cycling is described in [Kingsley 95]. Common phase cycling methods to acquire the complex signal in the indirect dimension are *States* [States 82] and *time proportional phase shift (TPPI)* [Marion 83].

The exact nature of the excitation and reconversion procedure determines the information available from the experiment. In the following, two specific 2D NMR experiments are described, which are used in this work.

First, the most widely used and simplest 2D pulse sequence is described, the correlation spectroscopy (COSY) experiment [Aue 76]. It is depicted in Fig. 2.6 A and consists of just two 90° pulses. The sequence correlates the chemical shift of spins that share a mutual J-coupling, thereby simplifying the peak assignment of complex spectra and elucidating the structure of molecules.

For a simple explanation how this happens during the pulse sequence,

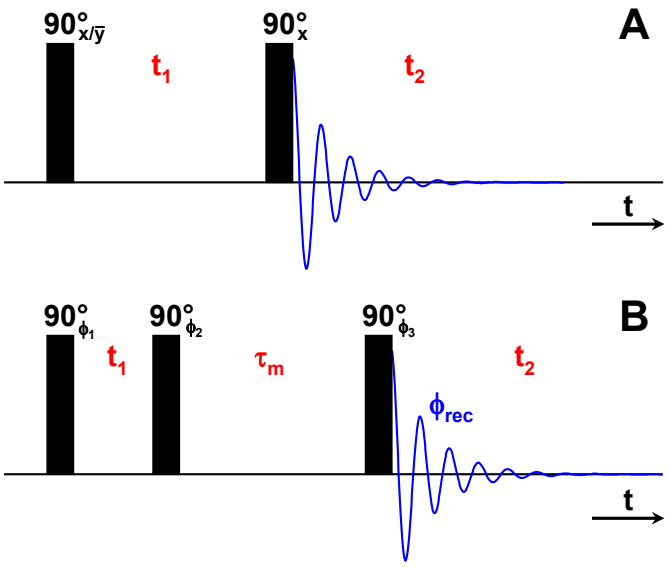

Figure 2.6: Two simple two-dimensional NMR experiments used in this work. **A:** The correlation spectroscopy (COSY) sequence. **B:** The exchange spectroscopy (EXSY) sequence.

two J-coupled spins, A and X, are considered with a respective chemical shift offset $\nu_A = \Omega_A/2\pi$ and ν_X. The magnetization associated with spin A will, after the initial 90° pulse, precess during t_1 according to its chemical shift offset ν_A. The second 90° pulse then transfers some part of this magnetization to the coupled spin X. The part that remains with A will then precess in the detection period t_2 with frequency ν_A, just as it did during t_1, so in the final spectrum it will produce a peak at (ν_A, ν_A), as it is shown in Fig. 2.7. This peak is equivalent to an uncoupled AX spin system and sits on the diagonal of the 2D spectrum and is therefore referred to as a *diagonal peak*. In contrast, the transferred magnetization will precess in t_2 at the frequency of the spin X, and will thus produce a peak in the 2D spectrum at (ν_A, ν_X). This is the peak of interest, as it provides direct evidence of the coupling between the spins A and X. It is commonly referred to as a *cross peak*. As the whole process also operates in reverse direction for magnetization originally associated with the X spin, the COSY spectrum is symmetric with another diagonal peak at (ν_X, ν_X) and a cross peak at (ν_X, ν_A). A more detailed explanation of the pulse sequence, using the quantum mechanical product operator formalism

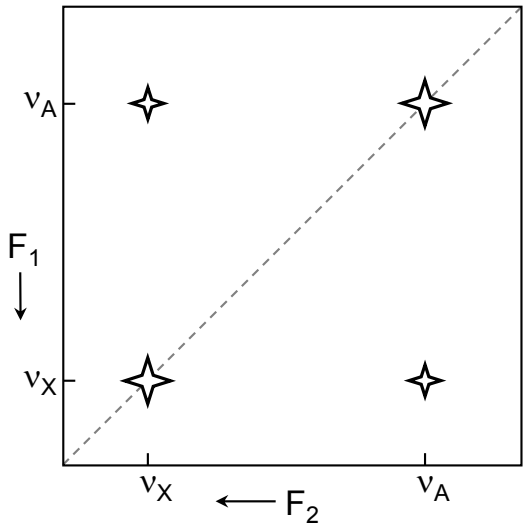

Figure 2.7: COSY spectrum of a J-coupled, two-spin AX system. Diagonal peaks are equivalent to those observed in a 1D spectrum, while cross peaks provide evidence of a coupling between the spins.

can be found in [Levitt 01].

In a COSY experiment with a sample containing two compounds with one spin species each, for example a mixture of benzene and chloroform, no cross peaks are observable (see Fig. 2.8). This is due to the fact, that the J-coupling is a purely intramolecular spin-spin interaction and the spins inside of each molecule are equivalent.

The second 2D experiment, which is used in this work for studying the dissolution process of ^{129}Xe, is the *exchange spectrocscopy* (EXSY) [Jeener 79] experiment. The pulse sequence (see Fig. 2.5 B) is commonly used to study chemical exchange of spins on the time scale of the mixing time τ_m. Consider a system with two chemical states A and X. All spins are excited by the initial 90° pulse, and the magnetization in the chemical state A evolves during the evolution time t_1 with ν_A. The second 90° pulse stores the evolved magnetization along the z-axis. If a part of the magnetization changes its chemical state from A to X during the mixing time, it will precess with the frequency ν_X during the detection, giving rise to the cross peak at (ν_A,ν_X). As this exchange process happens also vice versa, the intensity of both cross peaks is the same, and the spectrum is symmetric, like the COSY spectrum

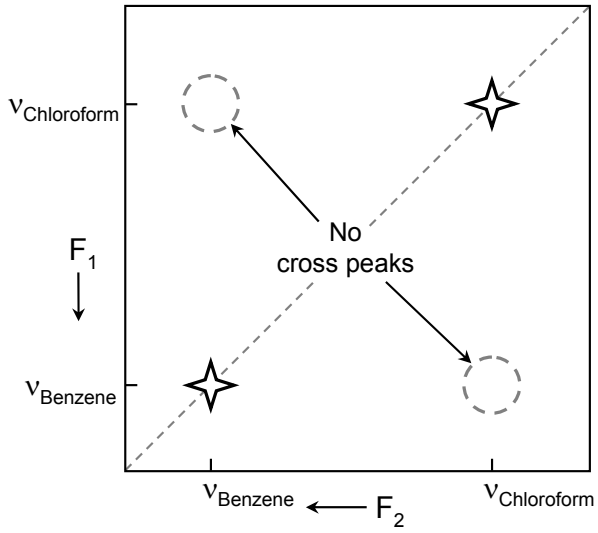

Figure 2.8: COSY spectrum of a sample containing benzene and chloroform. No cross peaks are observed because there is no intermolecular coupling. (Figure adapted from [Richter 00])

shown in Fig. 2.7. As the amplitude of the cross peaks depends on the mixing time, the dynamics of the exchange process can be quantified by measuring different EXSY spectra with varying mixing times. In the case of the dissolution of ^{129}Xe gas, the two chemical states are the gaseous and the dissolved phase which feature a different chemical shift. An eight-step phase cycle (see Tab. 2.1) is appropriate for averaging of the desired signal while suppressing all other contributions, e.g. by a stimulated echo.

Cycle counter n	ϕ_1	ϕ_2	ϕ_3	ϕ_{rec}
1	Ψ	0	0	0
2	$\Psi + \pi$	0	0	π
3	Ψ	0	π	π
4	$\Psi + \pi$	0	π	0
5	Ψ	0	$\pi/2$	$3\pi/2$
6	$\Psi + \pi$	0	$\pi/2$	$\pi/2$
7	Ψ	0	$3\pi/2$	$\pi/2$
8	$\Psi + \pi$	0	$3\pi/2$	$3\pi/2$

Table 2.1: Eight-step phase cycle appropriate for the 2D EXSY experiment. The phase $\Psi = 0$ for the 'cosine' data set of the States procedure [States 82] for phase sensitive acquisition in the indirect dimension, while $\Psi = \pi/2$ for the 'sine' data set.

2.2 MRI fundamentals

While in NMR spectroscopy a very homogeneous static magnetic field is essential for proper results, in MRI additional magnetic field gradients have to be applied. These gradients allow to distinguish spins in different spatial positions, and offer the possibility to gain spatial information from their inherent characteristics, like frequency and phase. MRI has become a routine technique in medical diagnosis, with the main advantages of being a non-invasive method with free choice of the imaging plane, and the possibility to discriminate various types of tissue.

2.2.1 Magnetic field gradients

In general, a magnetic field gradient is given by the second rank tensor

$$\underline{\mathbf{G}} = \nabla \mathbf{B} = \begin{pmatrix} \frac{\partial B_x}{\partial x} & \frac{\partial B_x}{\partial y} & \frac{\partial B_x}{\partial z} \\ \frac{\partial B_y}{\partial x} & \frac{\partial B_y}{\partial y} & \frac{\partial B_y}{\partial z} \\ \frac{\partial B_z}{\partial x} & \frac{\partial B_z}{\partial y} & \frac{\partial B_z}{\partial z} \end{pmatrix} . \tag{2.32}$$

If the additional gradient field is small in comparison with the static field $|\mathbf{r} \cdot \underline{\mathbf{G}}| \ll |\mathbf{B}_0|$, the gradient tensor $\underline{\mathbf{G}}$ can be truncated to a gradient vector

$\mathbf{G}$, which contains only those elements of the tensor aligned parallel to the $\mathbf{B}_0$ field,

$$\mathbf{G} \approx \left(\frac{\partial B_z}{\partial x}, \frac{\partial B_z}{\partial y}, \frac{\partial B_z}{\partial z} \right)^T = (G_x, G_y, G_z)^T \,. \tag{2.33}$$

This approximation is valid for all cases described in this thesis. In presence of such a constant field gradient, the Larmor precession frequency of the spins becomes spatially dependent,

$$\omega_L(\mathbf{r}) = -\gamma(B_0 + \mathbf{G} \cdot \mathbf{r}) \,. \tag{2.34}$$

2.2.2 k- and q-space

The spatial dependence of the resonance frequency, which arises from magnetic field gradients, is the basic principle of MRI; as it was first proposed by [Lauterbur 73]. The effects of magnetic field gradients on the response of a system to pulses are commonly expressed using the formalism of gradient moments and Fourier conjugates $\mathbf{k}$ and $\mathbf{q}$ as described in [Callaghan 91, Blümich 00]. This concept will be introduced first for a single pulse experiment. In general, the magnetization after an 90° pulse, for a time-dependent magnetic field, is expressed by a product of an attenuation due to relaxation and a phase term $\phi(t)$,

$$M(t) = M_0 \exp\left[-\frac{t}{T_2} + i \int_0^t \omega_L(t') \mathrm{d}t' \right] \,. \tag{2.35}$$

The spatial dependence is contained in $\phi(t)$, which with Eq. 2.34 can be written as

$$\phi(t) = \int_0^t \omega_L(t') \mathrm{d}t' = -\gamma B_0 t - \gamma \int_0^t \mathbf{G}(t') \cdot \mathbf{r}(t') \mathrm{d}t' \,. \tag{2.36}$$

If the spatial distribution of spins is also time-dependent, i.e. that the nuclei are moving on the time-scale of the experiment, $\mathbf{r}(t)$ can be expressed by a Taylor expansion

$$\mathbf{r}(t) = \mathbf{r}_0 + \mathbf{v}_0 t + \tfrac{1}{2}\mathbf{a}_0 t^2 + \dots \,, \tag{2.37}$$

where $\mathbf{v}_0$ and $\mathbf{a}_0$ are parameters of the expansion with the dimension of a velocity and an acceleration. These parameters are related to the physical nature of the dynamics of the system. For a linear motion, for example,

$\mathbf{v}_0 = (\mathbf{r}(t) - \mathbf{r}_0)/t$. While for the case of diffusion $\mathbf{v}_0$ is determined by an ensemble average from the mean square displacement $\langle \mathbf{r}^2 \rangle = 6Dt$ (see Eq. 2.57). Once these parameters are determined, they can be considered as constants in time and have not to be included in the integral over time. This finally leads to

$$\begin{aligned} \phi(t) &= -\gamma B_0 t - \gamma \mathbf{r}_0 \cdot \int_0^t \mathbf{G}(t')\mathrm{d}t' - \gamma \mathbf{v}_0 \cdot \int_0^t \mathbf{G}(t')t'\mathrm{d}t' \\ &\quad -\tfrac{1}{2}\gamma \mathbf{a}_0 \cdot \int_0^t \mathbf{G}(t')t'^2\mathrm{d}t' - \dots \\ &= \phi_0 - \gamma \sum_{k=0}^{\infty} \frac{\partial^k \mathbf{r}}{\partial t^k}(0)\mathbf{m}_k \,, \end{aligned} \tag{2.38}$$

where $\mathbf{m}_k$ are the different moments of the time-dependent gradient function

$$\mathbf{m}_k = \int_0^t \mathbf{G}(t')t'^k \mathrm{d}t' \,. \tag{2.39}$$

The first and the second moment are the definitions of the Fourier conjugates $\mathbf{k}$ to position $\mathbf{r}$ and $\mathbf{q}_v$ to mean velocity $\mathbf{v}_0$,

$$\mathbf{k} = -\frac{\gamma}{2\pi}\mathbf{m}_0 = -\frac{\gamma}{2\pi}\int_0^t \mathbf{G}(t')\mathrm{d}t' \tag{2.40}$$

$$\mathbf{q}_v = -\frac{\gamma}{2\pi}\mathbf{m}_1 = -\frac{\gamma}{2\pi}\int_0^t \mathbf{G}(t')t'\mathrm{d}t' \,. \tag{2.41}$$

The elegance of this formalism is the fact, that the NMR experiment might be chosen in a way, that allows the selective modulation of the magnetization by only one type of spatial dependence, which can then be separately investigated. Eq. 2.35 can therefore be rewritten as

$$M(t) = M_0 \exp\left[-\frac{t}{T_2} - -i\omega_0 t - i2\pi(\mathbf{r}_0 \cdot \mathbf{k} + \mathbf{v}_0 \cdot \mathbf{q}_v + \dots)\right] . \tag{2.42}$$

If an NMR experiment is, for example, conducted in a way that $\mathbf{k} = 0$ and $\mathbf{q}_v \neq 0$ during the data acquisition, it leads to velocity encoding, meaning that only moving spins contribute to the signal intensity. Also the simple case of non-moving spins is included in this equation, and will be considered in the next section.

2.2.3 Encoding of position

This section gives some examples of simple NMR imaging experiments of non-moving spins, i.e. experiments in **k**-space, where $\mathbf{m}_k = 0$ for all $k > 1$. There are two different methods to encode a spin position, namely *frequency* and *phase encoding*, which differ in the sequence how the reciprocal **k**-space is sampled. While in NMR spectroscopy time and frequency are Fourier conjugates, they are translated by a magnetic field gradient into spatial dimensions in imaging (see Eq. 2.34 and 2.40), and the acquired NMR signal can be described as the trajectory in **k**-space,

$$s(t) \equiv p(\mathbf{k}) = \int \mathrm{d}\mathbf{r} P(\mathbf{r}) e^{-i2\pi\mathbf{k}(t)\cdot\mathbf{r}} \,. \tag{2.43}$$

This relation is illustrated in Fig. 2.9. The concept of **k**-space is completely analogous to the reciprocal space in scattering experiments [Callaghan 91].

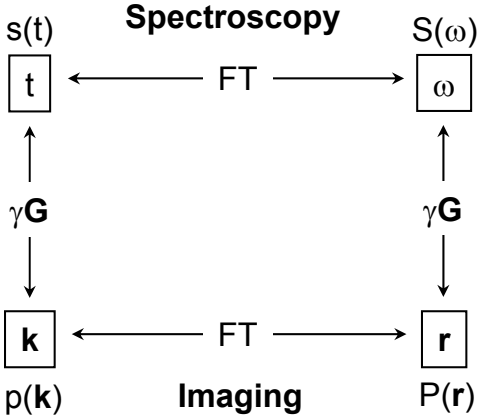

Figure 2.9: Relation between the Fourier conjugates in spectroscopy (t, ω) and in imaging $(\mathbf{k}, \mathbf{r})$. In presence of a magnetic field gradient the spectrum $S(\omega)$ becomes the spatial projection of the sample $P(\mathbf{r})$ with the Fourier conjugate $p(\mathbf{k})$ [Blümler 93].

The simplest technique to obtain an image by NMR is by frequency encoding, where a NMR spectrum of a certain sample is measured in presence of a magnetic field gradient. Starting with two differently shaped samples of the same substance, in a homogeneous field $\mathbf{B}_0$, a usual NMR spectrum will yield a single peak (see left side of Fig. 2.10). If an additional constant magnetic

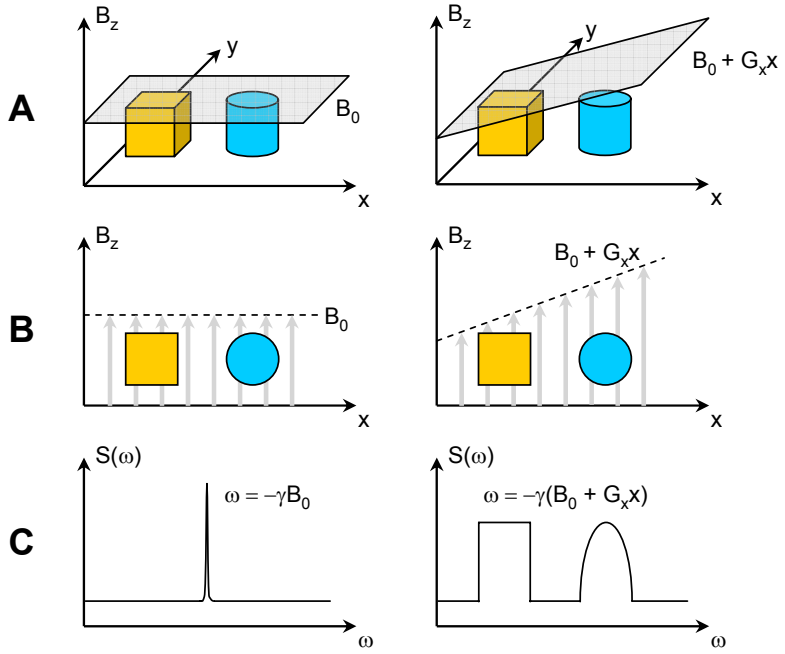

Figure 2.10: Principle of frequency encoding. The situations of two differently shaped samples in a homogeneous magnetic field (left) and with an additional gradient field (right) are shown. **A:** 3D representation of the objects. **B:** Projection along the y-axis. **C:** NMR spectra of the objects.

field gradient along the x-direction G_x is applied, the resonance frequency becomes dependent on the spatial position of the sample $\omega_L = -\gamma(B_0 + G_x x)$, and the NMR spectrum reveals the projection of the sample density along the gradient axis (see right side of Fig. 2.10). The *field of view* (FOV), i.e. the maximum region which can be imaged, depends in general on the interval $\Delta\mathbf{k}$ used to sample the $\mathbf{k}$-space,

$$\mathrm{FOV} = \frac{1}{\Delta\mathbf{k}}\,. \tag{2.44}$$

In the case of frequency encoding, it depends on the sampling rate, the 'dwell time' t_{dw} between the acquisition of two data points, and the gradient strength G,

$$\mathrm{FOV}_{freq} = \frac{2\pi}{\gamma G t_{dw}}\,. \tag{2.45}$$

The detected signal is the convolution of the spatial information of the sample with the NMR spectrum in absence of a gradient. Therefore, the resolution of the image Δr_{freq} is defined by the line width of the NMR spectrum $\Delta\omega$ and the gradient strength G,

$$\Delta r_{freq} = \frac{\Delta\omega}{\gamma G} \,. \tag{2.46}$$

It indicates the minimum distance of two structures which can still be resolved.

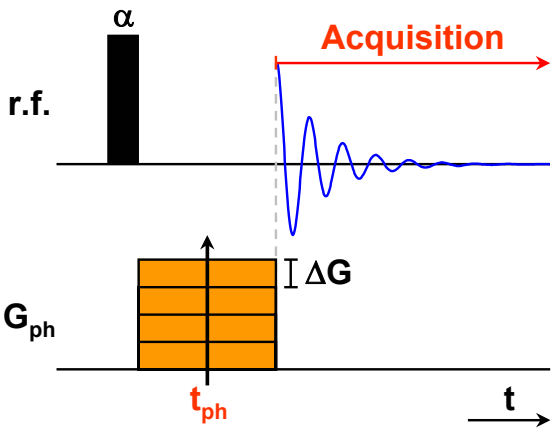

Figure 2.11: Principle of phase encoding. During the evolution time t_{ph}, the spatial information along $\mathbf{G}_{ph}$ is encoded in the phase of the acquired signal by incrementing the gradient amplitude with each experiment.

Instead of encoding the spatial information in the precession frequency of the spins, it can also be encoded in a phase modulation of the acquired signal. This is accomplished by applying a gradient pulse in between the r.f. pulse and the acquisition of the signal (see Fig. 2.11), which leads to a phase shift of the signal,

$$\Delta\phi = \gamma\mathbf{r} \cdot \int_0^{t_{ph}} \mathbf{G}_{ph}(t')dt' \,. \tag{2.47}$$

If the gradient is kept constant during the time t_{ph}, but its amplitude is incremented by $\Delta\mathbf{G}$ from experiment to experiment, the phase change of the NMR signal is proportional to the location of the spins $\mathbf{r}$,

$$\Delta\phi = \gamma t_{ph}\Delta\mathbf{G} \cdot \mathbf{r} \,. \tag{2.48}$$

Hence, for this method, the **k**-space is sampled by incrementing $\mathbf{G}_{ph}$ instead of the time, and the FOV is given by

$$\mathrm{FOV}_{ph} = \frac{2\pi}{\gamma \Delta G t_{ph}} \,. \tag{2.49}$$

The spatial resolution is mainly defined by the set FOV and the number of gradient steps n,

$$\Delta r_{ph} = \frac{\mathrm{FOV}_{ph}}{n} = \frac{2\pi}{\gamma |\mathbf{G}_{max}| t_{ph}} \,, \tag{2.50}$$

as the time t_{ph} is only restricted by T_2 and not by T_2^* as in frequency encoding. This means, that the obtainable resolution in phase encoding experiments mainly depends on the maximum amplitude of the gradients, $\mathbf{G}_{max} = n\Delta\mathbf{G}$, and on the signal of the sample, as for each pixel or voxel the signal has to exceed the noise level.

In principle, all imaging sequences are formed by combining these two different techniques for spatial encoding in different variations. A simple pulse sequence, the FLASH (Fast Low Angle SHot) experiment [Haase 86], is depicted in Fig. 2.12. It uses frequency encoding in x-direction and phase encoding in y-direction, and is applied in this thesis for imaging of hyperpolarized gases. During the acquisition under the read gradient, k_x is sampled line by line, depending on the strength of the phase gradient, which determines k_y. The shown sequence only samples the upper right quadrant of the **k**-space, which is in principle sufficient for obtaining a full image of the sample. However, the signal-to-noise ratio (SNR) can be further increased by covering the full range of **k**-space. The points with $k_x < 0$ are obtained by a *gradient echo*, during which the spins are first dephased by a gradient with opposite direction to the read gradient during a time $t_{read}/2$, before they are rephased by the read gradient to obtain an echo signal at the center of the acquisition window. The points with $k_y < 0$ can be obtained by inverting the phase gradient. As in hyperpolarized gases, the magnetization is in a non-thermal state, which is destroyed with each single r.f. pulse, only low flip angles can be applied. In return, the sequence can be repeated as fast as possible because no waiting is needed to recover the equilibrium state.

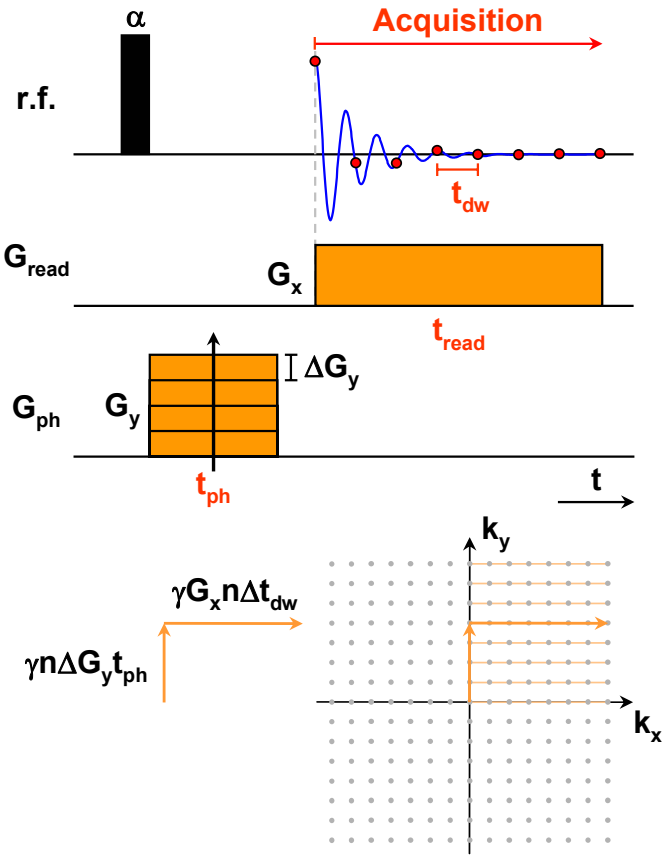

Figure 2.12: FLASH sequence for 2D imaging. The **k**-space is sampled by frequency encoding in x-direction and phase encoding in y-direction.

2.2.4 Slice selection

Three-dimensional imaging can, in principle, be performed by two phase encoding and one frequency encoding gradient along the spatial axes. However, for most applications this method is too time consuming, and enormous data sets are produced. Therefore, it is often advantageous to measure only a few 2D cross sections through the sample with a predetermined thickness. Such *slice selection*, is accomplished by shaped r.f. pulses in presence of a slice selection gradient. The principle of selective excitation is depicted in Fig. 2.13. A sinc-shaped pulse ($\sin x/x$) excites a rectangular spectrum in the frequency domain. In a first approximation the excitation pulse length

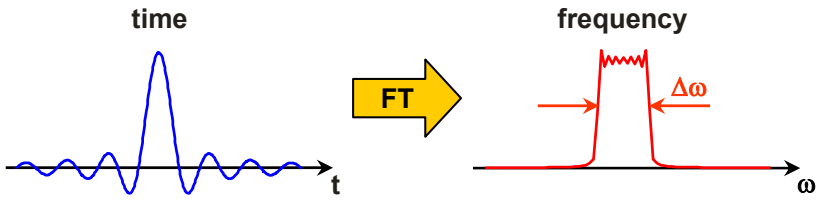

Figure 2.13: Principle of selective excitation: A sinc-shaped pulse, $(\sin x/x)$, excites a rectangular spectrum in the frequency domain. If a gradient is applied during the pulse, only spins residing in a certain slice of the sample are excited.

t_{pulse} is proportional to the spectral width $\Delta\omega_{pulse}$ excited by this pulse,

$$\Delta\omega_{pulse} \sim \frac{1}{t_{pulse}} \,. \tag{2.51}$$

A long 'soft' pulse, (which is often modulated in shape, for instance by a sinc function), can therefore selectively excite only a part of the whole spectrum. In presence of a gradient, this leads to a *slice selection*, as the spectrum is the projection of the sample along the gradient-direction (see Fig. 2.10). As the phases of the excited spins start to dephase already during the time of the slice selection pulse under influence of the gradient, usually a refocusing gradient pulse is applied with inverted amplitude and half the time of the r.f. pulse. Hereby, ideally all spin phases in the slice are refocused.

2.3 Diffusion fundamentals

This section focuses on the basics of molecular mass transport and self-diffusion, its effect on NMR experiments, and its quantification by pulsed gradient NMR. Especially for the NMR experiments in gases on which the second part of this thesis is focused, diffusion plays a major role and leads to unexpected effects in simple pulse sequences. Therefore, a brief introduction into theory of diffusion is given. The topic is covered in much more detail in [Crank 85, Callaghan 91, Kimmich 97].

2.3.1 Diffusion

Diffusion is the process by which matter is transported from one part of a system to another as a result of random molecular motion. It can be described by a flux $\mathbf{j}\,[kg\,m^{-2}s^{-1}]$ through a section, which is caused by a concentration gradient of the particles normal to this section ∇c, in order to reach thermodynamic equilibrium. The relation between these two measures was found by A. Fick in 1855 and is called Fick's first law,

$$\mathbf{j} = -D\nabla c\,. \tag{2.52}$$

The proportional constant is the diffusion coefficient $D\,[m^2s^{-1}]$, where c denotes the concentration in $[kg\,m^{-3}]$ and the nabla operator ∇ is given by

$$\nabla = \frac{\partial}{\partial x}\mathbf{e}_x + \frac{\partial}{\partial y}\mathbf{e}_y + \frac{\partial}{\partial z}\mathbf{e}_z\,. \tag{2.53}$$

If the number of particles is conserved, the time dependent change of the concentration is associated with a change in flux and the continuity theorem applies,

$$\nabla\mathbf{j} = -\frac{\partial c}{\partial t}\,. \tag{2.54}$$

Combining Eq. 2.52 and 2.54 immediately leads to Fick's second law,

$$\frac{\partial c}{\partial t} = \nabla\cdot(D\nabla c)\,, \tag{2.55}$$

which describes the time evolution of the concentration. For simple boundary conditions, this diffusion equation can be easily solved, as shown in [Crank 85]. For example, in the case of three-dimensionally diffusing particles, which originate at time $t = 0$ from a point source with $c = 1$ in a volume with $c = 0$, the concentration of the particles at the location $\mathbf{r}$ after a time t is given by

$$c(\mathbf{r},t) = \frac{1}{(4\pi Dt)^{3/2}}\,\exp\left[-\frac{\mathbf{r}^2}{4Dt}\right]. \tag{2.56}$$

The relation between the mean square displacement $\langle\mathbf{r}^2\rangle$ of the particles in a time t, and the diffusion coefficient was described in [Einstein 05, Smoluchowski 06] via the relationship

$$\langle\mathbf{r}^2\rangle = 6Dt\,. \tag{2.57}$$

For the one dimensional case, Eq. 2.56 and 2.57 becomes

$$c(x,t) = \frac{1}{\sqrt{4\pi Dt}} \exp\left[-\frac{x^2}{4Dt}\right] \tag{2.58}$$

$$\langle x^2 \rangle = 2Dt\,. \tag{2.59}$$

If the diffusion is observed to be anisotropic in different spatial directions, the diffusion coefficient is expressed by the Cartesian tensor

$$\underline{\mathbf{D}} = \begin{pmatrix} D_{xx} & D_{xy} & D_{xz} \\ D_{yx} & D_{yy} & D_{yz} \\ D_{zx} & D_{zy} & D_{zz} \end{pmatrix}, \tag{2.60}$$

where the off-diagonal elements vanish if the principal axes system of the tensor coincides with the Cartesian reference system.

2.3.2 Statistical description

In the case of self-diffusion, where the concentration gradient $\nabla c = 0$, the random translational movement of the particles is caused by a statistical Brownian motion, which depends on the temperature of the system. This motion can be expressed by a mean distance $\overline{x}$ which each particle covers during the time t, as the result of numerous individual collisions (known as *random walk*). The probability of finding a particle at a distance x after the time t, when it resided at $x = 0$ at time $t = 0$, follows a Gaussian statistics,

$$P(x,t) = \frac{1}{\sqrt{2\pi\overline{x}^2}} \exp\left[-x^2/2\overline{x}^2\right]\,. \tag{2.61}$$

The Einstein-Smoluchowski relation in Eq. 2.59 links the microscopic nature of the individual particle jumps with the macroscopic description of diffusion for $\langle x^2 \rangle = \overline{x}^2$, leading to the probability function

$$P(x,t) = \frac{1}{\sqrt{4\pi Dt}} \exp\left[-x^2/4Dt\right]\,. \tag{2.62}$$

Fig. 2.14 depicts this function for the diffusion coefficient of gaseous ^{3}He at room temperature and different times.

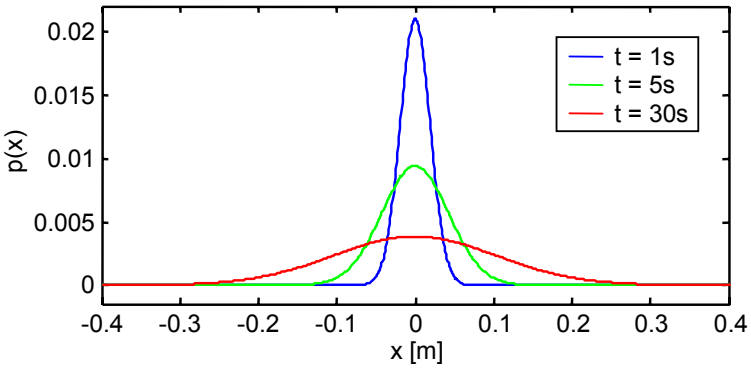

Figure 2.14: Gaussian probability distribution of finding a particle at a distance x, for an instantaneous plane source, plotted for different times t and a diffusion coefficient of $D = 1.8 \cdot 10^{-4}\, m^2/s^{-1}$.

2.3.3 Restricted diffusion

In the two previous sections, the diffusion coefficient was considered to be independent of time and the probability is assumed to be always Gaussian. This means that the diffusion coefficient stays constant and is independent of the observation time Δ. This assumption is only valid if no obstacles interfere with the free movement of the particles. For longer times Δ the probability rises, that a particle in a container collides with the walls. This restriction leads to a deviation of the measured diffusion coefficient to the unrestricted one. If the diffusion time Δ is chosen long enough, such that on average all particles have experienced the restrictions, the diffusion coefficient reaches the long time limit and is time independent again.

2.3.4 Measurement by NMR

Since Hahn's discovery of the spin echo, NMR has become an important tool in measuring diffusion. Carr and Purcell first described in [Carr 54], using a random walk model, how the dephasing of spins caused by diffusion can be partly refocused in a spin echo. In 1956 Torrey introduced a diffusion term in the phenomenological Bloch equations [Torrey 56], hereby providing a very useful theoretical tool for predicting diffusion effects in pulse sequences. In 1965, Stejskal and Tanner developed the pulsed gradient spin echo method

[Stejskal 65], which opened the way for measuring also small diffusion coefficients with high precision. In the following, the two basic pulse sequences for diffusion measurements are examined, which are depicted in Fig. 2.15.

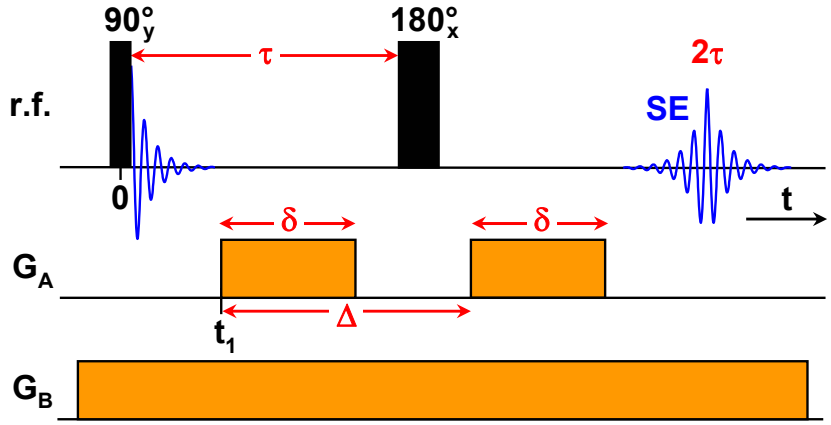

Figure 2.15: The two basic experiments to measure the diffusion coefficient by the amplitude of a spin echo in the presence of a pulsed gradient $\mathbf{G}_\mathrm{A}$ or a steady gradient $\mathbf{G}_\mathrm{B}$.

The encoding of a movement requires a pulse scheme, in which the zeroth gradient moment $\mathbf{m}_0 = 0$, while $\mathbf{m}_1 \neq 0$ (see Eq. 2.39). A simple example is the pulsed gradient spin echo (PGSE) sequence (see Fig.2.15 A), which uses a bipolar gradient, separated by a time Δ, meeting the condition $\mathbf{k}_1 = -\mathbf{k}_2$, i.e. that for non-moving spins, without considering relaxation, the signal is completely refocussed at time 2τ and independent of the spatial spin distribution. The echo amplitude reduces with the movement of spins from $\mathbf{r}$ to $\mathbf{r}'$ during the time Δ, because their accumulated phase during the first gradient, while residing at $\mathbf{r}$ is not completely rewinded during the second gradient as they experience a different magnetic field at the new location $\mathbf{r}'$. Following Eq. 2.42 the signal at the echo position 2τ is given by

$$E(q_v) = \int \mathrm{d}v_x P(v_x, \Delta) \exp\left[i2\pi q_v v_x\right] , \tag{2.63}$$

when relaxation is neglected and a one-dimensional gradient in x-direction G is assumed; $P(v_x, \Delta)$ is the distribution of the velocities of the spins in x-direction v_x for a time Δ, while q_v denotes the Fourier conjugate of v_x, as

defined in Eq. 2.41. To calculate q_v, the gradient $G(t)$ during the experiment is written as,

$$G(t) = \begin{cases} -G & , t_1 < t < t_1 + \delta \\ G & , t_1 + \Delta < t < t_1 + \Delta + \delta \\ 0 & , \text{all other } t \end{cases} \tag{2.64}$$

with a negative sign for the first pulse, because a negative gradient has the same effect on the spin phases as a positive gradient with a subsequent phase inversion by a 180° r.f. pulse. This leads to

$$\begin{aligned} q_v &= -\frac{\gamma}{2\pi}\left[-\int_{t_1}^{t_1+\delta} Gt'\mathrm{d}t' + \int_{t_1+\Delta}^{t_1+\Delta+\delta} Gt'\mathrm{d}t'\right] \\ &= -\frac{\gamma}{2\pi}\frac{G}{2}\left[-(t_1+\delta)^2 + t_1^2 + (t_1+\Delta+\delta)^2 - (t_1+\Delta)^2\right] \\ &= -\frac{1}{2\pi}\gamma G\delta\Delta\,, \end{aligned} \tag{2.65}$$

where δ is the gradient pulse length and Δ defined as shown in Fig. 2.15 A. When the velocity is replaced by the mean displacement of the spins x' during the time Δ, the echo amplitude is given by

$$E(q_v) = \frac{1}{\Delta}\int \mathrm{d}x' P(x',\Delta)\exp\left[i2\pi q_v x'/\Delta\right]\,, \tag{2.66}$$

where $P(x',\Delta)$ is the known probability distribution from Eq.2.62, leading to

$$E(q_v) = \frac{1}{2\Delta\sqrt{\pi D\Delta}}\int \mathrm{d}x' \exp\left[-\frac{x'^2}{4D\Delta} + i2\pi q_v x'/\Delta\right]\,. \tag{2.67}$$

When the reciprocal velocity q_v is substituted by the reciprocal space $q = -q_v/\Delta$ and the Fourier theorem $\mathcal{F}[f(t/a)] = |a|F(a\omega)$ is used, this corresponds to the Fourier transformation of a Gaussian function with a width of $4D\Delta$, which results in

$$E(q) = \exp\left[-4\pi^2 q^2 D\Delta\right] = \exp\left[-\gamma^2 G^2\delta^2 D\Delta\right]\,. \tag{2.68}$$

This equation is only valid for the case $\Delta \gg \delta$. For finite δ, the effect of diffusion during the r.f. pulses has also to be taken into account, which after a longer calculation leads to the effective diffusion time of $\Delta - \delta/3$ in the Stejskal-Tanner equation [Stejskal 65],

$$E(\delta,\Delta) = \exp\left[-\gamma^2 G^2\delta^2 D(\Delta - \delta/3)\right]\,. \tag{2.69}$$

A semi-logarithmic plot of the normalized echo amplitudes $\frac{E(q)}{E(0)}$, acquired for different gradient amplitudes, versus $\gamma^2 G^2 \delta^2 (\Delta - \delta/3)$ gives access to the diffusion coefficient.

The echo attenuation for the second experiment in Fig. 2.15 B using a steady field gradient is already included in Eq. 2.69 as a special case, if $\delta = \Delta = \tau$ is chosen. The echo signal is then given by

$$E(\tau) = \exp\left[-\tfrac{2}{3}\gamma^2 G^2 D \tau^3\right] . \tag{2.70}$$

As the experiments and more detailed calculations in Section 4.2 show, this equation is only valid for the assumption that the influence of diffusion during the acquisition of the signal can be neglected.

2.3.5 Diffusion in gas mixtures

The diffusion of light gases at ambient temperature can be influenced by varying their pressure p or by admixing them with heavier buffer gases. The diffusion coefficient of a gas mixture is given by the sum of the individual diffusion rates weighted by their molar fraction [Wilke 50]. Hence, for a binary mixture of helium (He) and a buffer gas (BG) it is given by

$$\frac{1}{D_{mix}} = \frac{x_{He}}{D_{He}} + \frac{x_{BG}}{D_{BG}} , \tag{2.71}$$

where x denotes the molar fractions of the gases, respectively. The relevant diffusion coefficient for NMR is not that of the bulk mixture D_{mix}, but rather that of the signal carrying isotope (here ^{129}Xe or ^{3}He) in the mixture, so that Eq. 2.72 has to be modified [Mair 02],

$$\frac{1}{D_{He/BG}(x)} = \frac{x_{He}}{D_{He}} + \frac{1 - x_{He}}{D^0_{He/BG}} , \tag{2.72}$$

where the diffusion coefficients D follow the nomenclature: $D_{He/BG}(x)$ for ^{3}He in the mixture with the BG, D_{He} for pure ^{3}He ($x = 1$) and $D^0_{He/BG}$ for ^{3}He at infinite dilution $x \to 0$ in the buffer gas. This value can be calculated with the classical theory for transport in dilute gases [Hirschfelder 64],

$$D^0_{He/BG} = \frac{3}{16} \frac{\sqrt{2\pi (k_B T)^3 \left(\frac{1}{m_{He}} + \frac{1}{m_{BG}}\right)}}{p \pi \sigma^2_{He,BG} \Omega^{(1,1)^*}} , \tag{2.73}$$

where k_B is the Boltzmann constant, p the pressure, m_{He} and m_{BG} are the ^{3}He and BG atomic mass, respectively, $\pi\sigma^2$ the collision cross section in a rigid-sphere model, and $\Omega^{(1,1)^*}$ a T-dependent factor depending on the actual interatomic potential. The values obtained by this equation were compared with the values obtained by NMR in [Agulles-Pedró 04, Acosta 06a] showing with a high accuracy the validity of Eq. 2.72. Table 2.2 shows the experimentally determined values for ^{3}He and ^{129}Xe within SF_6 as a buffer gas [Acosta 06a, Acosta 06b] without any spatial restrictions. The same experimental setup was also used for the gas mixing experiments in this thesis.

	^{3}He	^{129}Xe
$D_{SG}\,[m^2/s]$	$1.85 \cdot 10^{-4}$	$5.8 \cdot 10^{-6}$
${}^0D_{SG/BG}\,[m^2/s]$	$4.8 \cdot 10^{-5}$	–

Table 2.2: Diffusion coefficients of signal carrying gases (SG) ^{3}He and ^{129}Xe in binary mixture with SF_6 without spatial restrictions.

2.4 Hyperpolarized Gases

One of the main problems in most NMR experiments is the lack of sensitivity due to the low thermal spin polarization at ambient temperatures, which was already shown in section 2.1.3. Therefore in recent years, several *polarization* techniques were developed to overcome the Boltzmann distribution of the spins, leading to an enhancement of the NMR signal up to 5–6 orders of magnitude. These techniques follow different routes to obtain this non-thermal equilibrium state. For example, *dynamic nuclear polarization* (DNP) utilizes microwave irradiation of an electron transition, which is coupled to the nuclei of interest [Abragam 78], while *parahydrogen induced polarization* (PHIP) is accomplished by a chemical reaction of the compound of interest with parahydrogen [Natterer 97].

In this work the noble gases ^{3}He and ^{129}Xe are polarized indirectly by a transfer of angular momentum from circular polarized laser light to an electronic spin first, which couples afterwards to the particular nuclear spin

via the hyperfine interaction. The first step of this mechanism, the optical pumping, was discovered by Kastler in 1950 [Kastler 50], for which he was awarded the Nobel prize in physics in 1966. The second step, the ability to transfer polarization from electron to nuclear spins, was found by Bouchiat in 1960 [Bouchiat 60]. In this work, two different methods of optical pumping were used for the particular gases, namely *Spin Exchange Optical Pumping* (SEOP) for ^{129}Xe and *Metastable Exchange Optical Pumping* (MEOP) for ^{3}He, which are both explained in the following sections.

This section also covers the relaxation mechanisms of HP gases, which lead to a loss of the polarized state, as well as the different physical and chemical properties of ^{3}He and ^{129}Xe.

2.4.1 Spin Exchange Optical Pumping

SEOP polarizes an electronic spin state of a gaseous alkali metal by irradiation of circular polarized laser light (optical pumping). This polarization is then transferred via spin exchange to the nuclear spin. The theory of this method is described in much detail in [Happer 72]. Although this method works generally with all alkali metals, the usage of rubidium was established in most cases due to its technical advantages, like low vapor pressure, practical handling and safety aspects. In the following the principle of SEOP for ^{129}Xe polarization is shortly described, further information can be found in [Walker 97, Appelt 98], details focusing especially on the setup used in this work are given in [Mühlbauer 07].

The electronic energy term scheme of Rb in presence of a magnetic field is depicted in Fig. 2.16. The energy levels split into $(2J + 1)$ Zeeman sublevels, which are characterized by the magnetic quantum number $m_J = -J, -J + 1, \ldots, J$, where J is the total angular momentum of the electrons (coupled spin and orbit angular momentum). Resonant irradiation with circular polarized laser light can only excite transitions with $\Delta m = \pm 1$, depending on the helicity of the photons. In the case of Rb, the D1 transition from the ground state $^{2}S_{1/2}$ with $m_J = -1/2$ to the level $^{2}P_{1/2}$ with $m_J = +1/2$ is excited by σ^{+}-light with a positive helicity ($\Delta m = +1$). Collisions with other atoms cause an equal distribution of the two excited states on a timescale of 10 ps (*collisional mixing*) [Appelt 04]. Usually the excited state has a lifetime of ca. 30 ns and relaxes into the ground state by spon-

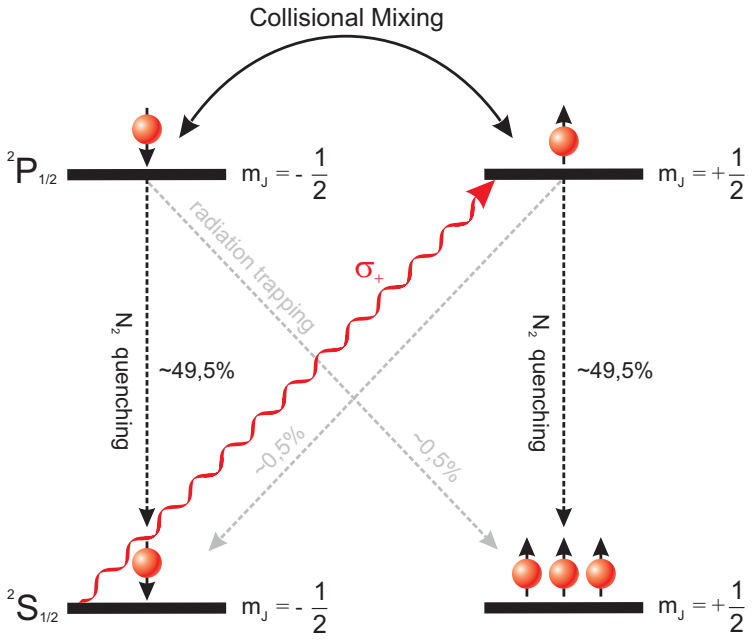

Figure 2.16: Optical pumping process of the D1 transition in Rb metal, by circular polarized σ_+ laser light. The excited states are mixed by gas collisions and radiation trapping is avoided by the admixture of N_2 as a quench gas.

taneous emission of a circular polarized photon, which can be absorbed by other alkali atoms, leading to attenuation of the optical pumping (referred to as *radiation trapping*). Therefore, a quench gas (usually N_2) is admixed, which enables a radiation free transition to the ground state by collisions. For typical partial pressure of ca. 0.35–0.4 bar N_2 the lifetime of the excited state is lowered to ca. 1 ns, leading to an almost total suppression of spontaneous emission. As only the ground state with $m_J = -1/2$ is continuously depopulated by the laser excitation, this process leads to a spin polarization in the $m_J = +1/2$ state.

The main reason, why Rb is the alkali metal of choise in most applications of SEOP, is that its D1 transition energy corresponds to a wavelength of 794.8 nm, which can be excited by commercially available high power diode laser arrays. The disadvantage of these lasers is their broad emission profile with a line width of 2-4 nm, which is in general much more than the width of the Rb absorption line. Therefore, only a small part of the laser light is taking

part in the polarizing process. To overcome this problem, SEOP is often conducted at elevated pressure, where the life time of the excited state is shortened by inelastic scattering, leading to a *pressure broadening* of the line [Romalis 97]. In our setup typically 7 bar of ^{4}He are used, which leads to a broadened absorption line width of ca. 0.5 nm (see Fig. 3.9).

The spin exchange between optically pumped Rb electrons and ^{129}Xe nuclei is mediated by a collisional polarization transfer, which can include either only the two particles themselves or three-body collisions with N_2, as indicated in Fig. 2.17. Which kind of process occurs predominantly, depends

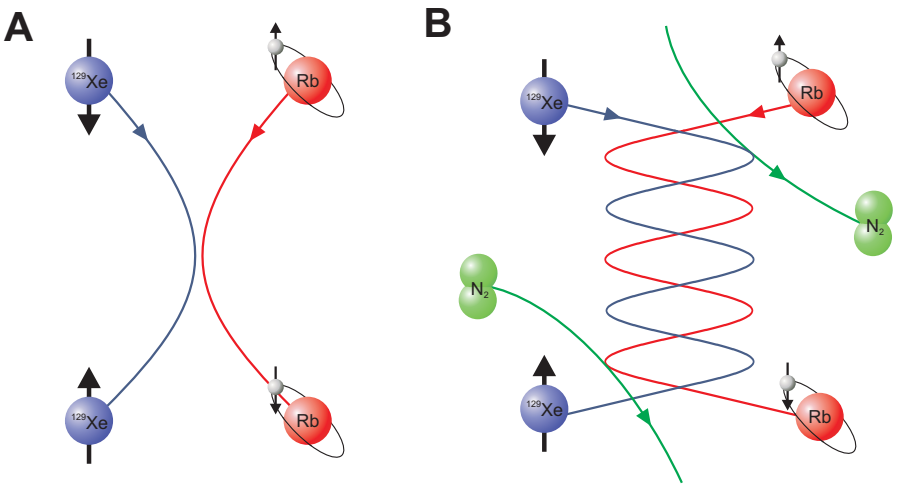

Figure 2.17: Spin exchange process between the optically pumped Rb electron spin and the ^{129}Xe nuclear spin. **A:** Exchange by binary collisions at elevated gas pressures. **B:** Exchange via the formation of van der Waals molecules by collisions with N_2 at low pressures.

on the gas pressure in the optical pumping cell. Under high pressure conditions of several bars mainly *binary collisions* between Rb and ^{129}Xe take place, leading to short living Rb-Xe complexes with a lifetime of ca. 1 ps (see Fig.2.17 A). At low gas pressures Rb-Xe *van der Waals molecules* can be formed in a triple partner collision with N_2 (see Fig.2.17 B). The life time of this molecules depends strongly on the gas pressure because they exist only until the next collision with a N_2 molecule (e.g. 0.1 μs at 1.3 mbar). A detailed investigation of these collisional processes causing the spin exchange can be found in [Happer 84].

Important steps towards the successful application of the described hyperpolarization method for ^{129}Xe were, inter alia, the separation of the polarized gas from the the Rb metal vapor in the optical pumping cell, and the realization of the continuous flow mode [Driehuys 96, Goodson 02]. Recent experiments show that extremely high polarizations above 60% can be achieved by either recirculation of the gas [Knagge 04], by extremely high laser power [Zook 02], or by using low gas pressures and counterflowing the gas mixture with the laser light over a long optical pumping region to improve the efficiency of the spin exchange [Ruset 06].

2.4.2 Metastable Exchange Optical Pumping

The described SEOP mechanism is also applied for ^{3}He polarization, but the spin exchange is not as effective as for ^{129}Xe. Therefore, instead of optical pumping of an alkali metal transition, a metastable electronic state of the ^{3}He itself is pumped, which then transfers its electronic polarization to nuclear ^{3}He spin polarization [Colegrove 63, Gamblin 65]. The process is depicted in Fig. 2.18 and explained in the following.

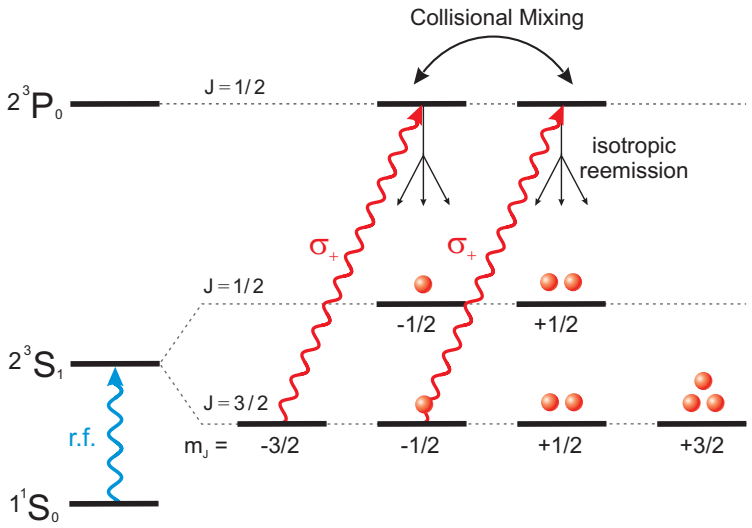

Figure 2.18: Optical pumping process of metastable ^{3}He atoms (^{3}He*). The population of the 2^3S_1 is driven by circular polarized laser light into the states with positive m_J quantum number, leading to a spin polarization of the metastable atom.

In ^{3}He gas at low pressure (about 1–2 mbar) a fraction of ca. 10^{-6} atoms is excited into a metastable 2^3S_1 state by a weak electrical discharge with a frequency of 3–4 MHz. In the presence of a small magnetic 'guiding' field ($B_0 \approx 100$ mT) the energy levels are split into different Zeeman sub levels. The irradiation of circular polarized laser light σ_+ with a wave length of 1083 nm excites the transition $2^3S_1 \rightarrow 2^3P_0$, and transfers an angular momentum of $\Delta m_J = +1$ to the electron spins. By collisional mixing of the excited states and isotropic reemission into the different 2^3S_1 hyperfine states, the population is driven into the states with positive m_J quantum number. Due to the strong hyperfine couplings in ^{3}He the nuclear spin of the metastable atoms becomes polarized. The nuclear polarization of the metastable atoms is then transferred to atoms in the ground-state by metastable exchange collisions. During these collisions the metastable and the ground-state atoms exchange their electron shells, while the nuclear polarization remains unaffected (see Fig. 2.19). Thus, the collisions yield a polarized ground-state atom and a non-polarized metastable atom, which can undergo again the optical pumping process.

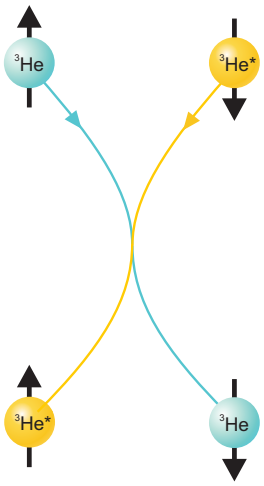

Figure 2.19: Metastability exchange collisions between ^{3}He and ^{3}He* which lead nuclear polarization of the ground-state atoms.

In comparison to SEOP the restriction to low pressures in MEOP poses the main problem, as the polarized gas has to be compressed from mbars to bars to accumulated sufficient amounts of gas, without losing its polarization.

This problem was solved by using a compressor without any magnetic parts, as shown in [Schmiedeskamp 04]. Hereby, polarization rates of up to 73% are obtainable for different applications in NMR and MRI. The maximum polarization value achieved in an optimized setup was $91\% \pm 2\%$ [Wolf 04].

2.4.3 Relaxation mechanisms

The population of a hyperpolarized system returns to its thermal equilibrium with the time constant T_1 (see Eq. 2.24). Therefore, it is essential that the time between the creation of the HP state and the beginning of the experiment is short in comparison to T_1. Several mechanisms contribute to the relaxation rate ($1/T_1$) of HP noble gases *in vitro* and *in vivo*, including for example surface relaxation, oxygen-induced relaxation, gradient-induced relaxation, dipolar relaxation and in case of ^{129}Xe spin rotation relaxation.

The *surface relaxation* rate of ^{3}He and ^{129}Xe depends on the surface-to-volume ratio S/V of the gas container and of a coefficient η, as described in [Driehuys 95],

$$\frac{1}{T_{1,surf}} = \frac{1}{\eta}\frac{S}{V}\,, \tag{2.74}$$

where η depends on the material, the temperature, and the magnetic field strength. The relaxation rate can be influenced by different types of surface coatings, achieving record relaxation times of up to 840 h for a Rb-coated glass cell [Rich 02]. The effects of different coatings of glass cells are described in [Deninger 06]. It was also shown recently, that for uncoated aluminosilicate glasses the wall relaxation is dominated by ferromagnetic impurities in the glass walls. By demagnetizing the cells before usage, average relaxation times of 150 h are observed [Schmiedeskamp 06b, Schmiedeskamp 06a]. For ^{129}Xe, a T_1 time of 3 h has been reported for gas contained in a 7.5 cm diameter quartz cell [Chann 02].

In medical imaging paramagnetic oxygen is a very potent source of relaxation. The *oxygen-induced relaxation* rate has been empirically determined for ^{129}Xe [Jameson 88] and ^{3}He [Saam 95] at room temperature as

$$\frac{1}{T_{1,O_2}} = \frac{p_{O_2}}{\xi}\,, \tag{2.75}$$

where $\xi_{Xe} = 2.80$ bar s and $\xi_{He} = 2.40$ bar s. Accordingly, the p_{O_2} in room air results in T_1 relaxation times of 13 s and 11 s respectively.

Magnetic field gradients are another source of T_1 relaxation of HP gases [Gamblin 65, Schearer 65, Cates 88], according to the simplified expression

$$\frac{1}{T_{1,grad}} = D\,\frac{|\nabla B_x|^2 + |\nabla B_y|^2}{B_0^2}\,, \tag{2.76}$$

where B_x and B_y are the transverse components of the main magnetic field B_0, with their spatial gradients ∇B_x and ∇B_y. This relation is only valid when the magnetic field and the gas pressure are sufficiently large, so that

$$\frac{\omega_0 r^2}{D} \gg 1\,, \tag{2.77}$$

where ω_0 is the Larmor frequency and r is the radius of the gas container [Cates 88]. According to the ratio of diffusion coefficients of ^{3}He and ^{129}Xe (see Tab. 2.2), ^{3}He is over 30 times more sensitive to inhomogeneous fields than ^{129}Xe. Therefore, HP ^{3}He is usually transported in specially designed magnetically shielded boxes providing a field of a few mT [Grossmann 00].

Dipolar relaxation caused by atomic collisions (^{3}He–^{3}He or^{129}Xe–^{129}Xe), during which the nuclear spins couple via magnetic dipole interaction, transferring their energy into a relative angular momentum. As a result, the nuclear polarization is lost. The resulting relaxation rates depend only on the gas pressure p at room temperature, and have been derived for ^{3}He and ^{129}Xe as,

$$\frac{1}{T_{1,dipolar}} = \frac{p}{809}\,\mathrm{h}^{-1} \quad (^3\mathrm{He}) \tag{2.78}$$

$$\frac{1}{T_{1,dipolar}} = \frac{p}{61}\,\mathrm{h}^{-1} \quad (^{129}\mathrm{Xe})\,. \tag{2.79}$$

Dipolar relaxation is thus insignificant except for very high pressures, where it imposes a fundamental limit on attainable storage times.

Additionally a new relaxation mechanism for ^{129}Xe was recently identified, which is caused by spin-rotation coupling in bound Xe–Xe van der Waals molecules [Chann 02]. The relaxation time of this mechanism is constant under usual circumstances[1],

$$\frac{1}{T_{1,vdW}} = \frac{1}{4.1}\,\mathrm{h}^{-1}\,, \tag{2.80}$$

[1]The relaxation time increases at extremely high field strengths (tens of tesla) and at very low pressures.

and even lowers the fundamental limitation on T_1 posed by the dipolar relaxation time in Eq. 2.79 for ^{129}Xe.

All the relaxation mechanisms sum up to to a total relaxation time

$$\frac{1}{T_{1,total}} = \sum_x \frac{1}{T_{1,x}}\,, \tag{2.81}$$

where x denotes all the different relaxation types mentioned above.

As a new technique to simplify the dissolution process of HP gases is introduced in Chapter 6 of this work, the relaxation mechanisms of HP gases in the solute state are considered in the following. The T_1 relaxation time of a dissolved HP gas, hereby mainly depends on the composition of the solvent. Maximum T_1 times for dissolved ^{129}Xe are reached in deuterated solvents, e.g. $\sim$ 5 min in deuterated urea [Rubin 00] or $\sim$ 17 min in D_2O [Bifone 96]. The oxygenation level of the solvent is hereby an important parameter, since interactions with paramagnetic substances decrease the T_1 time. Several studies showed that the T_1 of HP ^{129}Xe in blood depends on its oxgenation level, which is partly due to the paramagnetism of deoxyhemoglobin [Bifone 96, Albert 00]. Usual T_1 relaxation times of ^{129}Xe in potential carrier liquids as contrast agent in MRI range from 20–100 s [Goodson 99]. Therefore, such solutions of HP ^{129}Xe need to be prepared immediately (less than minutes) before the MR examination, as opposed to gaseous ^{3}He (T_1 up to 800 h) or frozen ^{129}Xe (T_1 up 500 h [Gatzke 93]), which can be transported over long distances after the polarization to the experiment site.

2.4.4 Properties of ^{3}He and ^{129}Xe

^{3}He is a perfectly inert noble gas that can be inhaled in large quantities (84% He, 16% O_2) without any severe adverse effects, as the solubility in blood is negligible. The only risk of breathing pure He is hypoxia, since the body is deprived of oxygen. This makes HP ^{3}He the ideal contrast agent for *in vivo* lung imaging [Middleton 95, Ebert 96, Kauczor 96]. Other applications in the field of particle physics are the usage of HP ^{3}He as spin filter for neutrons [Batz 05], and in electron scattering experiments for the determination of the neutron electric form factor [Becker 98]. ^{3}He is obtained from the decay of tritium (^{3}H), mainly as a by-product in the manufacturing of

nuclear weapons, and the total amount on earth is limited to hundreds of kg [Kauczor 98], while as a matter of curiosity, large quantities should be available on the moon [Wittenberg 86].

^{129}Xe is an inert noble gas as well, but its solubility in liquids and biological tissues is substantially larger than for ^{3}He [Goodson 99, Lynch 00]. Xe is known to have euphoric and anesthetic effects, and can be used as an inhalant anesthetic agent with many attractive properties, as it is does not bind to any other molecules in the body [Lynch 00]. The biodistribution of inhaled Xenon is well known, and pharmokinetic models for the in vivo uptake of HP ^{129}Xe have been presented [Peled 96, Martin 97]. The supply of Xe is virtually unlimited, as it is contained in the atmosphere ($\sim$ 0.01 ppm), but the natural abundance of the isotope ^{129}Xe is only 26.4%. Isotopic enrichment of ^{129}Xe to 80% is possible, but extremely expensive. Additionally, as its magnetogyric ratio is 2.75 times lower than of ^{3}He, the SNR of ^{129}Xe experiments is about one order of magnitude smaller than for ^{3}He at equal pressures and polarizations (see Tab. 2.3). The melting point of Xe at 1 bar is 161.4 K, which is higher than the temperature of liquid nitrogen. Therefore, Xe can be easily separated from other light gases by freezing it out and it can be stored in the solid state without great effort. The most important advantage for NMR is the sensitivity of the ^{129}Xe resonance to its chemical and physical environment, because its large electron cloud can be easily polarized. This results in a wide chemical shift range in usual applications of about 300 ppm, which makes it an interesting probe for material science, biology or medicine.

2.5 Intermolecular multiple quantum coherences in liquids

In the early 1990's a series of simple NMR experiments was conducted, that seemed to contradict conventional NMR theory [He 93, Warren 93], the detection of intermolecular multiple-quantum coherences (iMQC) in liquids. This section will shortly cover the theoretical basis of these measurements as described in [Richter 00], while a more detailed description can be found in [Lee 96, Levitt 96, Jeener 00]. This theory is required to understand the first measurements of intermolecular double-quantum coherences (iDQC) in

Isotope	^{1}H	^{3}He	^{129}Xe
Polarization P	$5 \cdot 10^{-6}$	0.7	0.2
Natural abundance n_I	0.9998	$1.38 \cdot 10^{-6}/1^*$	0.26
magnetogyric moment γ $[10^7 s^{-1} T^{-1}]$	26.75	-20.38	-7.45
Larmor frequency at 7 T ω_0 [MHz]	300	228	83
Spin density ϱ [cm^{-3}]	$6.7 \cdot 10^{22}$	$2.5 \cdot 10^{19}$	$2.5 \cdot 10^{19}$
relative signal $S \sim \varrho P n_I \omega_0^{3/4}$	1	42.53	1.48

Table 2.3: Comparison of the NMR properties of the different isotopes used in this work. All nuclei bear a spin $I = 1/2$. The relative signal is normalized on the ^{1}H signal. *: As in all experiments pure ^{3}He is used, the signal calculation is done with $n_I(^3\text{He}) = 1$.

the gas phase between HP ^{3}He nuclei, which are described in Chapter 5.

2.5.1 The CRAZED experiment

As already shown in Section 2.1.6, a simple 2-pulse COSY experiment can quantify the intramolecular J-coupling between two spins by the detection of their cross peaks (see Fig. 2.7). If the experiment is conducted with a sample containing two compounds with one spin species each, no cross peaks are observed (see Fig. 2.8), because the corresponding spins are in separate molecules and are not J-coupled to one another. When a 'double-quantum gradient filter' is added to the COSY pulse sequence, the whole 2D-spectrum is expected to be blank, as this filter only lets pass DQ signals, which would only arise from a state of two intermolecular coupled spins.

This filter is based on the fact that a gradient pulse modulates the resonance frequency of the spins as a linear function of space along the gradient axis (see Eq. 2.34). In a classical view, the transverse magnetization is wound up into a helix by such a pulse. As long as diffusion can be neglected on the timescale of the pulses, this helix represents a highly ordered state without net magnetization, which can be unwound by another gradient pulse of opposite polarity. This classical picture can be extended to MQC, although

the helix is no measurable quantity in there. If a gradient pulse is applied to a DQC, which naturally evolves at twice the basic resonance frequency, the created (virtual) helix has only half the pitch of a helix created by the same gradient pulse when applied to a single-quantum coherence (SQC). Therefore, a pair of gradient pulses whose areas are at a ratio of 1:2 acts as a DQ filter, i.e. that magnetization which is detected after this filter has to have been a DQC during the first gradient pulse which was then transferred to a SQC before the second gradient pulse. Only for this case the second gradient pulse exactly unwinds the helix and creates detectable net magnetization again.

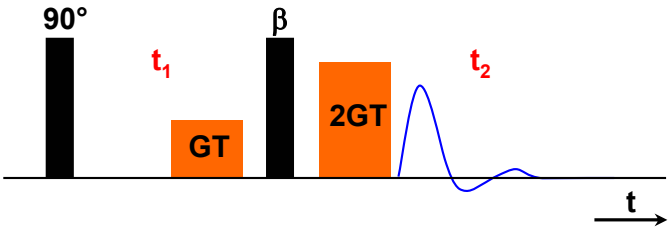

Figure 2.20: CRAZED pulse sequence to detect intermolecular double-quantum coherences. The area of the second gradient pulse is twice the area of the first one to act as a double-quantum filter. The signal is acquired directly after the second gradient pulse.

When such a DQ gradient filter is added to the second r.f. pulse of the COSY experiment, with GT the area of the first and $2GT$ the area of the second pulse as shown in Fig. 2.20, no signal is expected after this pulse sequence. As mentioned above and in Section 2.1.6, the first pulse of the COSY experiment creates a usual SQC, which will not pass the DQ filter. However, it was shown in [He 93], that large signals are detected after this pulse sequence. That is why this pulse sequence was called the CRAZED (COSY Revamped by Asymmetric Z-Gradient Echo Detection) sequence. As depicted in Fig. 2.21, peaks appear both on the pseudo-diagonal $F_1 = -2F_2$, and as cross peaks between benzene and chloroform.

Two conclusions can be drawn from the detection of these unexpected signals. First, there must have been a iDQC evolving before the gradient filter. Second, this coherence was transformed into a SQC after the first gradient pulse. This implies two consequences, which are examined in the

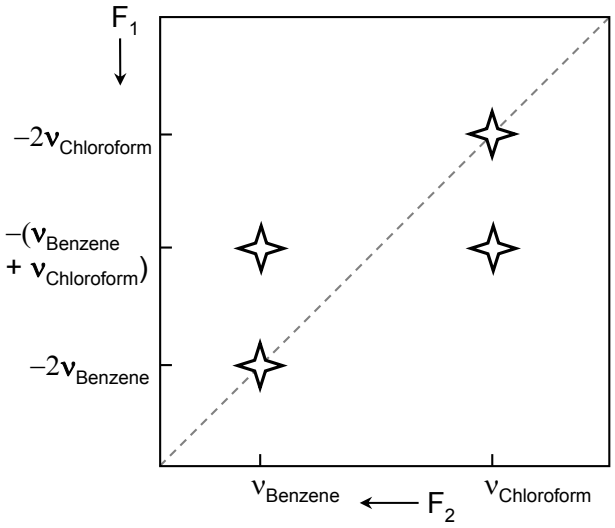

Figure 2.21: CRAZED spectrum of a mixture of chloroform and benzene. Following conventional theory all intermolecular couplings are averaged out, and this spectrum is expected to be blank. Instead, peaks with all properties of iDQCs are observed. (Figure adapted from [Richter 00])

following sections; first, a single pulse must create iDQC, also in liquids, (in solids this is well known). Second, there must be a net coupling between benzene and chloroform molecules, which transforms the DQC to a detectable magnetization. Both of these statements seem to contradict conventional NMR theory, and will be discussed in the following two sections.

2.5.2 The density operator

In the quantum mechanical picture of NMR the density operator ρ describes the state of the spin system at any point during the pulse sequence. A comprehensive discussion of this picture and the density operator is given in [Ernst 87, Levitt 01].

As already shown in Eq. 2.18 the spin system at thermal equilibrium follows a Boltzmann distribution. The density operator is then given by

$$\rho_{eq} = \frac{\exp(-\mathcal{H}/k_B T)}{\mathrm{Tr}[\exp(-\mathcal{H}/k_B T)]}\,, \tag{2.82}$$

where Tr denotes the trace calculation of the particular operator. To show the equivalence with the semi-classical picture the case of an isolated spin $I = 1/2$ is considered. The Hamiltonian of this system in a magnetic field is given by the Zeeman Hamiltonian,

$$\mathcal{H}_Z = \hbar\omega_0 \mathbf{I}_z \,, \tag{2.83}$$

as already shown in Eq. 2.4. In the a matrix notation with a basis set given by the two basis function $|\alpha\rangle = (1,0)^T$ and $|\beta\rangle = (0,1)^T$ for the 'up' and 'down' state, the angular momentum operator $\mathbf{I}_z$ can be written as

$$\mathbf{I}_z = \frac{1}{2}\begin{pmatrix} 1 & 0 \\ 0 & -1 \end{pmatrix} . \tag{2.84}$$

In this picture, the density operator at thermal equilibrium results in

$$\begin{aligned} \rho_{eq} &= \frac{\exp(-(\hbar\omega_0/k_BT)\mathbf{I}_z)}{\mathrm{Tr}[\exp(-(\hbar\omega_0/k_BT)\mathbf{I}_z)]} \\ &= \frac{\begin{pmatrix} \exp\left(-\frac{\hbar\omega_0}{2k_BT}\right) & 0 \\ 0 & \exp\left(+\frac{\hbar\omega_0}{2k_BT}\right) \end{pmatrix}}{\exp(-\hbar\omega_0/2k_BT) + \exp(+\hbar\omega_0/2k_BT)} \,, \end{aligned} \tag{2.85}$$

where the equilibrium populations of the two states are given by the diagonal elements of the matrix. Therefore, the ratio of the population of the two particular states is calculated as

$$\frac{P_\beta}{P_\alpha} = \frac{\exp(+\hbar\omega_0/2k_BT)}{\exp(-\hbar\omega_0/2k_BT)} = \exp\left(+\frac{\hbar\omega_0}{k_BT}\right) , \tag{2.86}$$

which corresponds exactly to the ratio given for the semi-classical picture in Eq. 2.18.

For a system of N coupled nuclear spins, the single operator $\mathbf{I}_z$ in the density matrix is substituted by the sum over all spins $\sum_i^N \mathbf{I}_{zi}$, leading to

$$\rho_{eq} = \frac{\exp(-(\hbar\omega_0/k_BT)\sum_i \mathbf{I}_{zi})}{\mathrm{Tr}[\exp(-\mathcal{H}/k_BT)]} \,. \tag{2.87}$$

Traditionally, the high-temperature approximation replaces the exponential function by its Taylor expansion, which is truncated after the first order term,

$$\rho_{eq}^{HT} \approx \frac{\mathbf{1} - (\hbar\omega_0/k_BT)\sum_i \mathbf{I}_{zi}}{\mathrm{Tr}[\exp(-\mathcal{H}/k_BT)]} \,. \tag{2.88}$$

This is very convenient, because any pulse sequence calculation can start with an equilibrium state of

$$\rho_{eq} \sim \mathbf{I}_{zi} \,, \tag{2.89}$$

because $\mathbf{I}_{zi}$ is the only variable that evolves in time. The argument that is usually given for the validity of the approximation is that the Boltzmann factor is a small number and therefore the higher order terms are negligible. This argumentation is a fallacy, which can be seen, if the Taylor expansion is not truncated

$$\rho_{eq} = \frac{\mathbf{1} - (\hbar\omega_0/k_BT)\sum_i \mathbf{I}_{zi} + \frac{1}{2}(\hbar\omega_0/k_BT)^2 \sum_i \sum_j \mathbf{I}_{zi}\mathbf{I}_{zj} - \cdots + \ldots}{\mathrm{Tr}[\exp(-\mathcal{H}/k_BT)]} \,. \tag{2.90}$$

Even though the quadratic term has a coefficient that is several orders of magnitude smaller than that of the linear term, the double sum in the quadratic term has N times as many members as the single sum in the linear term. For a typical NMR sample, $N = 10^{20}$ and $N^2 = 10^{40}$; hence it is not at all obvious that this expansion even converges. Therefore, the exact density operator in a closed form was calculated in [Lee 96] as a product of all individual spins. However, for an understanding of the signals detected in the CRAZED experiment, this expansion up to the second order is sufficient.

If a single 90° pulse in y-direction is applied to the spin system as described in Eq. 2.90, the operators in the sum of the quadratic term $\sum_i \sum_j \mathbf{I}_{zi}\mathbf{I}_{zj}$ are transformed into $\sum_i \sum_j \mathbf{I}_{xi}\mathbf{I}_{xj}$, which can be described as a mixture of zero-quantum and double-quantum coherences. These double-quantum coherences lead to the signal observed in the CRAZED experiment, which shows that the high-temperature approximation fails if large numbers of spins are coupled to each other. This coupling between the spins, which is also responsible for the transformation of the DQ signal into detectable magnetization, is examined in the following section.

2.5.3 The distant dipolar field

As already described in section 2.1.2, the interaction of two dipolar coupled spins is expressed by the dipolar Hamiltonian in Eq. 2.16. If this Hamiltonian

is extended to a system of N coupled spins, it amounts to

$$\mathcal{H}_{DD} = \frac{\mu_0}{4\pi} \sum_{j>k}^{N} \frac{\gamma_j \gamma_k \hbar}{r_{jk}^3} \left(\mathbf{I}_j \mathbf{I}_k - \frac{3(\mathbf{I}_j \cdot \mathbf{r}_{jk})(\mathbf{I}_k \cdot \mathbf{r}_{jk})}{r_{jk}^2} \right) . \tag{2.91}$$

This expression can be rewritten in polar coordinates, whereby the non-secular part of the dipole-dipole coupling terms may be discarded in high magnetic fields [Levitt 01]. The remaining dipolar Hamiltonian is

$$\begin{aligned} \mathcal{H}_{DD}^{sec} &= \frac{\mu_0}{4\pi} \sum_{j=0}^{N} \sum_{k=0}^{N} \frac{\gamma_j \gamma_k \hbar}{r_{jk}^3} (1 - 3\cos^2\theta_{jk})(3I_{jz}I_{kz} - \mathbf{I}_j \cdot \mathbf{I}_k) \\ &= \sum_{j=0}^{N} \sum_{k=0}^{N} D_{jk}(3I_{jz}I_{kz} - \mathbf{I}_j \cdot \mathbf{I}_k) , \end{aligned} \tag{2.92}$$

where θ_{jk} denotes the angle between the internuclear vector and the direction of the main magnetic field. The magnitude of this through-space interaction is given by the 'dipolar coupling constant'

$$D_{jk} = \frac{\mu_0}{4\pi} \frac{\gamma_j \gamma_k \hbar}{r_{jk}^3} (1 - 3\cos^2\theta_{jk}) . \tag{2.93}$$

For a typical molecular distance of 5 Å (0.5 nm) between two protons and an angle $\theta_{jk} = 90°$ it amounts to $D_{jk} = 3020$ rad s^{-1}, which corresponds to a frequency of 480 Hz. If the dipolar couplings are on the order of hundreds of Hz, or more for nearby protons, the lines detected in NMR spectroscopy should be just that wide, and therefore no structure would be seen in the spectra. This is exactly the case in solid state NMR, in liquid state NMR usually sharp lines with widths of less than 1 Hz are detected. Thus the question arises; which mechanisms leads to this line narrowing?

In fact, there are two separate mechanisms that are responsible for the narrow lines observed in liquids. The first one applies to pairs of nearby spins, while the second one applies to spins which are far apart. Both mechanisms are based on the fact, that over the surface of an isotropic sphere the dipolar interaction averages to zero,

$$\int_{\theta=0}^{\pi} \int_{\varphi=0}^{2\pi} (1 - 3\cos^2\theta) \sin\theta \, \mathrm{d}\theta \mathrm{d}\varphi = 0 , \tag{2.94}$$

where the extra factor $\sin\theta$ arises from the fact, that the number of surface elements on a sphere is proportional to $\sin\theta$. The two mechanisms that average out the dipolar coupling are explained in the following.

The *intramolecular couplings* and the *intermolecular short range dipolar interactions* are averaged out by diffusion processes; while the intramolecular couplings vanish due to rotational diffusion on a timescale of typically 40 μs ($D_{rot} \sim 25$ kHz), the short range intermolecular interactions can be neglected due to translational diffusion. This is demonstrated by a simple calculation for water molecules. The root mean square distance that a water molecule covers in one direction during a given time t_D driven by diffusional motion is given by Eq. 2.59,

$$r_{rms} = \sqrt{2Dt_D}\,, \tag{2.95}$$

where the diffusion coefficient $D = 2.3 \cdot 10^{-9}$ m/s^2 at room temperature. As calculated above, the dipolar coupling between two protons at a distance of 0.5 nm amounts to ca. 480 Hz, which corresponds to an oscillation time of 2.1 ms. The dipolar coupling constant can only be measured, if the random motion of the spins happens on a much slower timescale, so that the angle θ_{jk} remains constant during the measurement and the integral in Eq. 2.94 is not averaged out. If, however, one spin moves a mean distance in the order of 0.5 nm, it is assumed that the whole range of angles is sampled, which leads to a total averaging of the interaction. The time required t_D for a diffusing spin to cover a distance of $r_{rms} = 0.5$ nm is calculated using Eq. 2.95. It amounts to only 54 ps, which is about 8 orders of magnitude less then the time associated with the dipolar coupling. This clearly shows the impossibility of measuring dipolar interactions for such short distances. If the spins are moved farther apart, the ratio of these times decreases even further, as it is approximately inverse proportional to the separation distance,

$$D_{jk} \cdot t_D \sim \frac{r_{rms}^2}{r_{jk}^3} \sim \frac{1}{r}\,. \tag{2.96}$$

Consequently, *individual* spin-spin dipolar interactions cannot be measured in liquid state NMR.

For *long range dipolar interactions* it is not sufficient to consider only individual spin couplings. As motional averaging is ineffective for spins separated by macroscopic distances, all individual couplings sum up with a proper

weighting for each spin pair. It is a fallacy to conclude that in general long range interactions are negligible because of its r^{-3} dependence, as the number of spins at a given distance increases with r^2. Therefore, the sum of all dipolar couplings decreases only with r^{-1}. The field arising from this sum is called the *distant dipolar field* (DDF). Only if the liquid is magnetically isotropic, i.e. that the magnetization is the same anywhere in the sample, the distant dipolar fields add up to zero by virtue of spherical symmetry. As a consequence, long range dipolar interactions reappear whenever the magnetization is a function of location, which is exactly the case if gradient pulses are applied, e.g. during the pulse sequence of the CRAZED experiment. Also if the sample is not spherical, the dipolar interactions are not averaged out completely, but usually in the absence of gradients the associated signals are too small to detect.

2.5.4 Analysis of the CRAZED experiment

The origin of the unexpected signals observed in the CRAZED experiment can now be understood, by considering the previous sections. The pulse sequence is depicted in Fig. 2.20. The quadratic term in the equilibrium density operator contains two-spin terms such as $\mathbf{I}_{z1}\mathbf{I}_{z2}$ (see Eq. 2.90), which are transformed into a mixture of double- and zero-quantum coherences $\mathbf{I}_{x1}\mathbf{I}_{x2}$ by the first 90° r.f. pulse. These DQCs evolve during t_1, giving rise to the cross peak signals. The second r.f. pulse (for the sake of simplicity also with a flip angle of 90°) transforms for example the evolved state $\mathbf{I}_{x1}\mathbf{I}_{y2}$ into $\mathbf{I}_{z1}\mathbf{I}_{y2}$, which is a SQ two-spin term. As it was a DQ state during the first and is a SQ state during the second gradient pulse, it passes the DQ gradient filter. Due to the gradient pulses the sample exhibits anisotropic magnetization after the second r.f. pulse and the dipolar couplings reappear. These dipolar couplings between spins 1 and 2 transform $\mathbf{I}_{z1}\mathbf{I}_{y2}$ into detectable magnetization $\mathbf{I}_{x2}$.

A more detailed and also quantitative analysis of the pulse sequence, using the density matrix calculation, is given in [Lee 96, Richter 00]. Here, only the resulting equations for the time evolution of the signal are given. The complete derivation reveals the following expression for the detectable magnetization after the second gradient pulse,

$$M^+(t_1,t_2) = i^{n-1} n M_0\, e^{i\Omega t_2} e^{-in\Omega t_1} \left(\frac{\tau_d}{t_2\Delta_s}\right) J_n\left(\frac{t_2\Delta_s}{\tau_d}\right), \qquad (2.97)$$

where n is the order of the multiple-quantum gradient filter ($n = 2$ for DQ), $\Delta_s = [3(\mathbf{g} \cdot \mathbf{e}_z) - 1]/2$ with $\mathbf{g}$ the unit vector in gradient direction, J_n the n-order Bessel function and the demagnetizing time

$$\tau_d = \frac{1}{\gamma \mu_0 M_0} \,. \tag{2.98}$$

Note, that this signal evolves at $n\Omega$ in the indirectly detected dimension t_1, which is the frequency associated to an n-quantum coherence. For a DQ experiment with the gradient orthogonal to the magnetic field, the equation simplifies,

$$M^+(t_1, t_2) = i2M_0 \, e^{i\Omega t_2} e^{-i2\Omega t_1} \left(\frac{\tau_d}{t_2}\right) J_2\left(\frac{t_2}{\tau_d}\right) \,. \tag{2.99}$$

Fig. 2.22 graphs this signal amplitude for on-resonant r.f. pulses ($\Omega = 0$), depending on the time t_2/τ_d. Unlike an usual FID, the signal increases during the acquisition time. This reflects the action of the dipolar couplings which transform two-spin one-quantum operators into detectable magnetization during t_2. The signal maximum occurs at $t_2 \approx 2.2\,\tau_d$, and is therefore inverse proportional to M_0; which usually depends on the temperature and the magnetic field. In the case of HP gases the signal maximum time depends on the polarization, with higher values leading to earlier times. In real experiments, the signal is suppressed by T_2^* relaxation, usually circumventing the full acquisition of the signal.

2.5.5 Optimum flip angles for CRAZED experiments

The signal-to-noise ratio of the detected iMQC signals in the CRAZED experiment can be increased by optimizing the flip angle β of the second r.f. pulse. The dependence of the different n-quantum signals on β was derived by [Chen 01a]. The expression for the signal detected in the CRAZED experiment (Eq. 2.97) changes to

$$M^+(\xi, \beta) = i^{-(n+1)} M_0 \left[n J_n(\xi)/\xi + \tfrac{1}{2} \left(J_{n-1}(\xi) - J_{n+1}(\xi)\right) \cos\beta \right] \,, \tag{2.100}$$

with on-resonant r.f. pulses ($\Omega = 0$) and $\xi = t_2/\tau_d \cdot \sin\beta$. In experiments with thermal magnetizations it can be assumed that

$$\xi = t_2 \gamma \mu_0 M_0 \sin\beta \ll 1 \,, \tag{2.101}$$

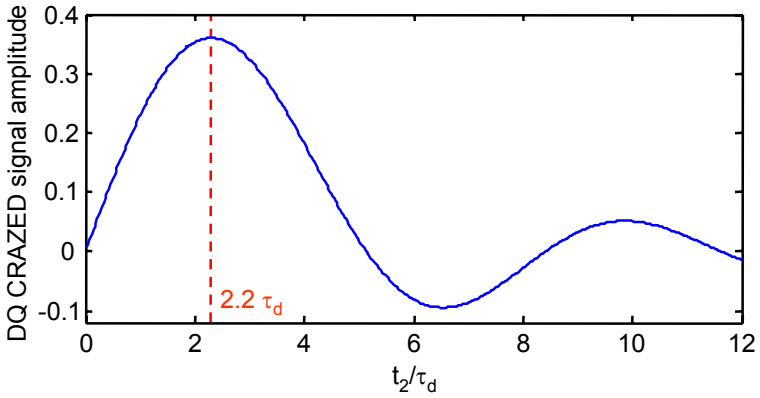

Figure 2.22: Theoretical shape of the time signal in a double-quantum CRAZED experiment after the second gradient pulse in absence of relaxation. The signal maximum occurs at $2.2\,\tau_d$, the signal amplitude is given as a fraction of the equilibrium magnetization M_0.

and therefore the Bessel functions can be approximated as

$$J_n(\xi) \approx \frac{1}{n!}\left(\frac{\xi}{n}\right)^n . \tag{2.102}$$

This leads to the simplified expression for the relative intensity $f(\beta)$ of n-order iMQC signals,

$$f(\beta) \sim \begin{cases} \sin^{-n-1}\beta(1+\cos\beta), & n<1 \\ \sin\beta\cos\beta, & n=0 \\ \sin^{n-1}\beta(1-\cos\beta), & n>1\,. \end{cases} \tag{2.103}$$

This theoretical signal dependence on β is depicted in Fig. 2.23 for $n = \pm 2$ and compared with experimentally obtained signal intensities [Chen 01a]. The signal maxima occur in perfect agreement of theory and experiment at $\beta = 60°$ and 120° respectively.

For the case of non-thermal polarizations the approximation in Eq. 2.102 may not be strictly valid anymore, as the magnetization M_0 in ξ may be too large. Without this approximation the signal for $n = 2$ is given by the exact expression

$$f(\beta) = |2J_2(\xi)/\xi + 1/2(J_1(\xi) - J_3(\xi))\cos(\beta)|\ , \tag{2.104}$$

which features a slightly different course, depending on the magnitude of M_0.

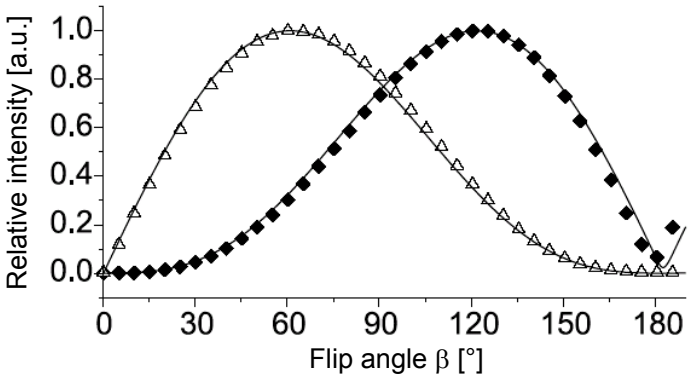

Figure 2.23: Normalized relative signal intensity of iDQCs as a function of the flip angle β. Left peak: n = -2; Right peak n = 2. Symbols indicate experimental data, while the solid lines are fitted to the normalized theoretical curves based on Eq. 2.103. (Figure adapted from [Chen 01a])

Chapter 3

Experimental setup

This chapter covers the different experimental setups for the measurements, including the NMR spectrometers, the clinical MRI scanner and the gas polarizers. It also gives a description of the developed gas mixing device, as well as an explanation of the flip angle calibration in HP gases.

3.1 NMR spectrometers

The "proof-of-principle" experiments with dissolved HP ^{129}Xe, as well as all experiments using HP ^{3}He, were conducted in a horizontal magnet with a field strength of 4.721 T and a bore diameter of 20 cm (Magnex Scientific Ltd., UK). It is equipped with actively shielded gradients with a maximum strength of 0.3 T/m (Bruker Biospin GmbH, Germany), that are driven by Copley amplifiers (Copley Controls Corp., USA). A double-resonant birdcage coil, manufactured by Bruker, was used for r.f. excitation and detection at the frequencies of 55.6 MHz (^{129}Xe) and 153.12 MHz (^{3}He). It features an inner diameter of 26 mm and a length of 45 mm. For the experiments with water, another birdcage coil with a diameter of 22 mm and a length of 31 mm was used, which was tuned to the ^{1}H-frequency of 201.01 MHz. The main advantages of conducting these experiments in a horizontal magnet with a large bore were practical aspects, like comfortable accessibility of the sample and enough space for assembling the valves of the gas mixing setup inside the magnet. Hereby all the connections can be kept short and the "dead" gas volume is minimized.

The continuous flow experiments with dissolved HP ^{129}Xe, using the membrane method inside the NMR tubes, were conducted in a standard vertical bore magnet with a magnetic field strength of 6.995 T (Bruker Biospin GmbH, Germany). For r.f. excitation and -detection a modified Bruker probehead was used. The original coil, designed for static solid state NMR, was exchanged by a saddle coil with two loops and an inner diameter of 10 mm. The double-resonant circuit was tuned to frequencies of 297.8 MHz for ^{1}H and 82.82 MHz for ^{129}Xe.

In both magnets the experiments were controlled by a Maran DRX console (Oxford Instruments, Oxfordshire, UK), using self developed software in a Matlab environment (MathWorks Inc., Natick, USA). This allows a synchronized control of the pulse sequence and other triggers, like e.g. the switching of the valves for gas mixing.

3.2 Clinical MRI scanner

The imaging experiments were conducted in a whole body scanner, type Magnetom Vision (Siemens Medical Solutions, Erlangen, Germany), at the university clinics of Mainz in the group of Prof. W. Schreiber. The scanner exhibits a magnetic field of 1.49 T and uses Numaris VB33D as controlling software. The gradient system is slightly stronger than in usual clinical scanners and features a maximum gradient strength of 50 mT/m. The system is equipped with a broadband amplifier, which also allows experiments at the present ^{129}Xe frequency of 17.59 MHz.

For this frequency two different coils were constructed at the Max Planck Institute for polymer research (MPI-P). The first one is a solenoid coil with a diameter of 65 mm and a length of 120 mm. By this means, the coil is suitable for later whole body imaging of small animals. The coil was wound using a 2 mm copper wire with 12 windings, and is shielded by a silver foil. A schematic view of the circuit, as well as an image of the coil, is depicted in Fig. 3.1. The coil features three different tunable capacitors for tuning and matching of the resonance circuit.

Furthermore, a surface coil was built to obtain larger SNRs of small objects, especially for later applications in brain imaging of small animals. The coil has a diameter of 32 mm and consists of 5 windings (see Fig. 3.2). The

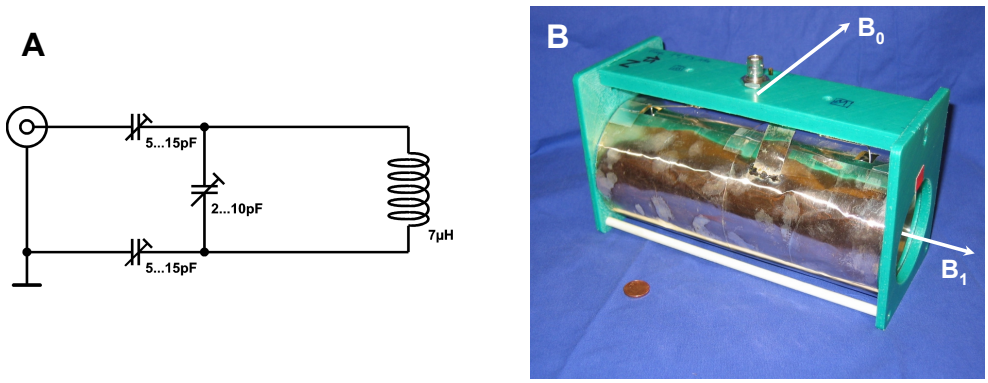

Figure 3.1: The solenoid coil constructed for ^{129}Xe imaging in a clinical 1.5 T scanner. **A:** Schematic view of the circuit; **B:** Image of the finished coil.

circuit comprises a tunable coil and a tunable capacitor for adjustment of the appropriate resonance frequency. Both coils have to be used perpendicularly to the B_0 field.

3.3 ^{3}He polarizer

The HP ^{3}He gas used in this work was obtained from a home built, large scale polarizer, which is located at the Institut für Physik at the university of Mainz. A detailed description of the setup is given in [Schmiedeskamp 04, Wolf 04]. The polarization process is based on the MEOP method (see Section 2.4.2), and yields polarizations values of up to 60% at flow rates of 3.2 bar l/h and of 77% at 1 bar l/h. A picture of the setup during the optical pumping process is shown in Fig. 3.3. The left hand side of the picture shows the optical system, which guides the circular polarized laser light through the gas cells filled with ^{3}He gas at low pressures of ca. 1 mbar. By an electric discharge, a part of the ^{3}He atoms is brought into a metastable state, which is excited by the laser irradiation. The blue fluorescence light due to the electric discharge can be seen on the right hand side of the picture.

After the polarization process, the compressed HP gas is transferred into a transport cell with a volume of 1.2 l and pressures of 2.1–2.7 bar. These

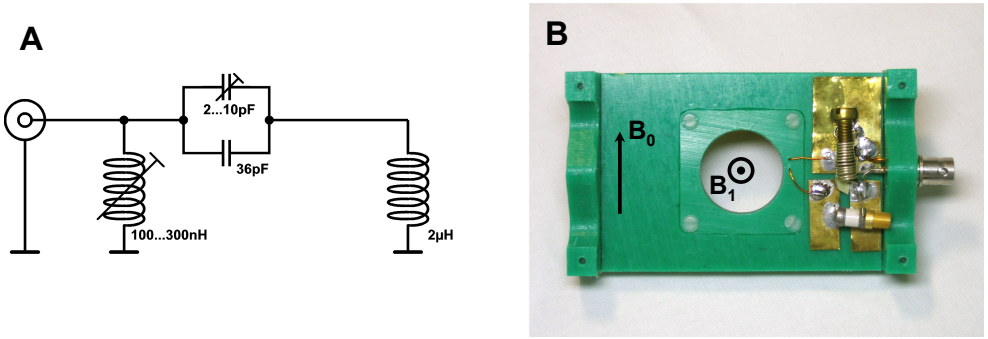

Figure 3.2: The surface coil constructed for ^{129}Xe imaging in a clinical 1.5 T scanner. **A:** Schematic view of the circuit; **B:** Image of the finished coil.

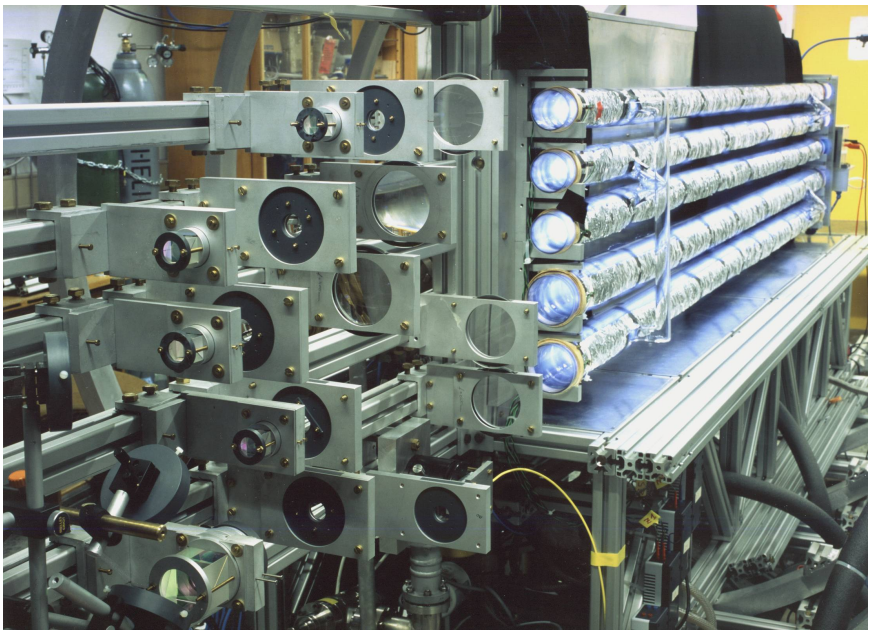

Figure 3.3: ^{3}He polarizer at the Institut für Physik at the university of Mainz. The optical system, guiding the laser light, is depicted at the left side. The blue fluorescence light in the pumping cells due to the electric discharge can be seen on the right hand side.

cells are made of iron-free aluminosilicate glasses to minimize relaxation effects. Subsequently, the cells are placed in shielded containers with a homogeneous low magnetic field (0.8 mT), produced by permanent magnets, and transported to the NMR laboratory at the MPI-P. The transport cells and containers are shown in Fig. 3.4 A. During the experiments, the cell is stored in a homogeneous magnetic field of 2.5 mT, generated by a current of 2 A through five coaxial coils of 45 cm diameter and 70 cm total length (see Fig. 3.4 B).

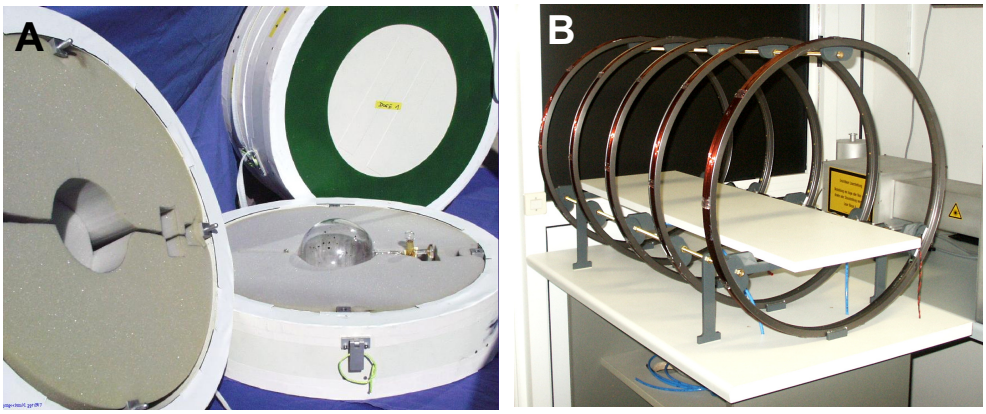

Figure 3.4: Transportation and storage of HP ^{3}He. **A:** Transportation box, consisting of a static magnetic field created by permanent magnets inside a μ-metal shielded container, with one glass cell inside [Beek 03]. **B:** Field coil to generate a homogeneous magnetic field for storage of the HP ^{3}He transport cells during the experiments.

3.4 ^{129}Xe polarizer

As the ^{129}Xe polarizer is an integral part of the present work, its setup is described in more details than the setup of the ^{3}He polarizer. The ^{129}Xe polarizer was developed and built at the Forschungszentrum Jülich and is similar to the one described in [Shah 00]. A schematic diagram of its design is shown in Fig. 3.5, the different components are explained in the following.

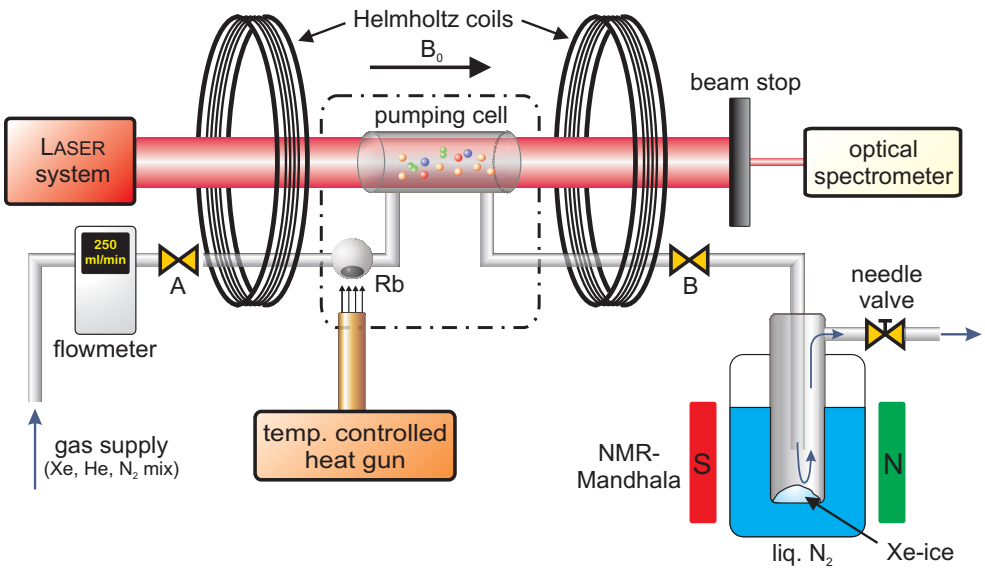

Figure 3.5: Schematic diagram of the ^{129}Xe polarizer, showing the different elements required for the polarization process.

3.4.1 Gas supply

The polarizer is supplied with a continuous flow of a gas mixture containing xenon, helium and nitrogen. As described in Section 2.4.1, helium is required for pressure broadening of the rubidium transitions, while the admixture of nitrogen avoids radiation trapping. The gas mixture is either supplied by a readily-blended gas bottle or by a home built gas mixing system which allows free choice of the mixing ratios. The polarizer usually operates at an absolute pressure of 8 bar, and the flow rate through the system is regulated by a needle valve at the outlet. Before the gas mixture is lead into the polarizer, a gas purifier (UltraPure™ Eliminator® CA, Nupure, Ottawa, Canada) removes all contaminating gases like O_2 and H_2O, that can cause an oxidation of the rubidium vapor. All tubings from the gas bottles to the optical pumping (OP) cell are made from stainless steel, as it turned out that the usage of polyurethane (PU) tubing leads to impurities in the gas stream, which oxygenate the rubidium due to small quantities of gas that are emitted from the material.

Two different readily-blended gas mixtures were used. For operation in *batch mode*, where the polarized ^{129}Xe is accumulated in the solid state by

freezing it in liquid nitrogen (see Fig. 3.5), a mixture of 1% Xe, 5% N_2, and 94 % He was used. The second mixture, containing 16% Xe, 32% N_2, and 52 % He, was used for experiments in *continuous flow mode*, where the gas stream is guided from the outlet of the polarizer directly into the NMR spectrometer.

The automated gas mixing system, that allows experiments with variable mixing ratios, is depicted in Fig. 3.6. It consists of three digital mass flow controllers (Bronkhorst EL-FLOW, Wagner M+R, Offenbach, Germany), which are connected to the three particular gas bottles. The desired mixing ratio is obtained by controlling the individual gas flow rates. The different gases are merged inside a vessel with a volume of 500 ml, which also serves as a reservoir. The total pressure is kept constant by a digital pressure controller (Bronkhorst EL-PRESS), which releases excess pressure to atmosphere. The whole system is easily controlled and monitored by a special computer software.

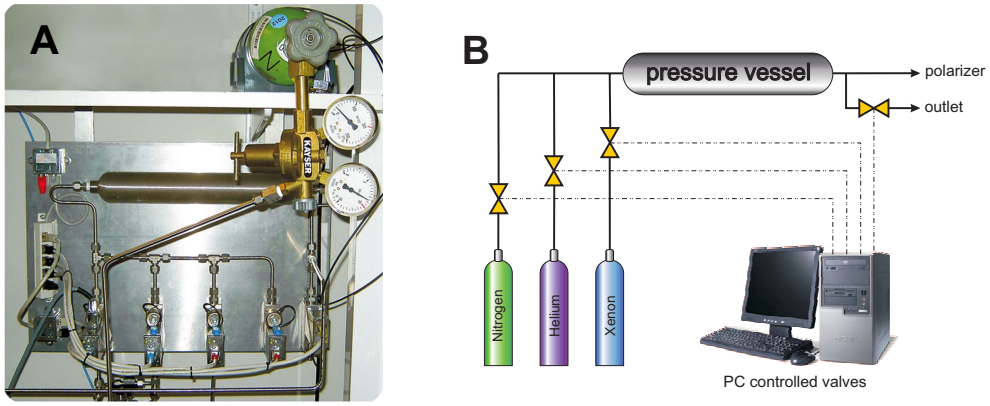

Figure 3.6: Gas mixing system of the polarizer. **A:** Picture of the mass flow and pressure controllers and the gas reservoir. **B:** Schematic diagram of the admixing process.

3.4.2 Optical pumping setup

The optical pumping (OP) setup is located inside of a aluminum box to minimize the danger of laser stray light and possible breakage of glass under high pressures. A picture of the setup inside the box is shown in Fig. 3.7,

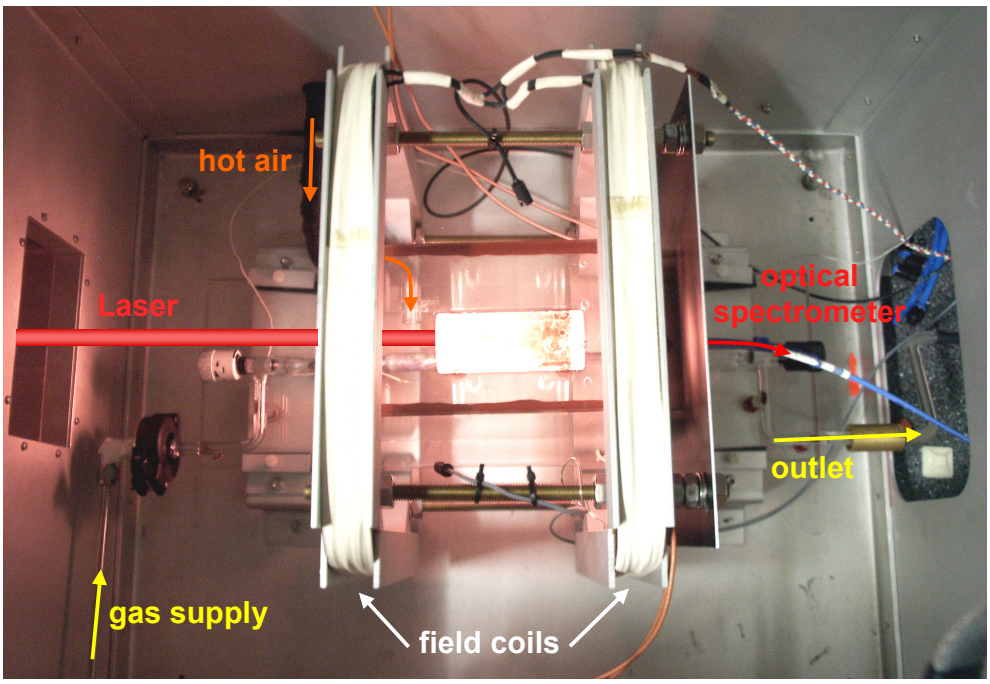

Figure 3.7: ^{129}Xe polarizer during the polarization process. The picture was taken with an infrared-sensitive camera, so that the usually invisible fluorescence light of the rubidium excitation is depicted clearly.

while the dismantled OP cell is depicted in Fig. 3.8.

The gas mixture flows into the pumping cell through valve A and the heated rubidium reservoir, where it takes up the Rb vapor. The OP volume is irradiated by circular polarized laser light, so that the ^{129}Xe nuclei are polarized via SEOP (see Section 2.4.1). The polarized gas leaves the pumping volume through valve B, and is either accumulated by freezing it in liquid nitrogen or guided directly into the NMR spectrometer. The gas flow through the entire setup is regulated manually by a needle valve at the outlet of the polarizer (after passing the freezing unit or NMR spectrometer).

The optical pumping cell, which was constructed at the Forschungszentrum Jülich, consists of a glass cylinder with flat glass windows in order to avoid lens effects on the pump laser beam. It is made from 5 mm thick borosilacate glass with an inner diameter of 24 mm, a length of 70 mm, and was tested to withstand gas pressures of up to 15 bar. The glass construction

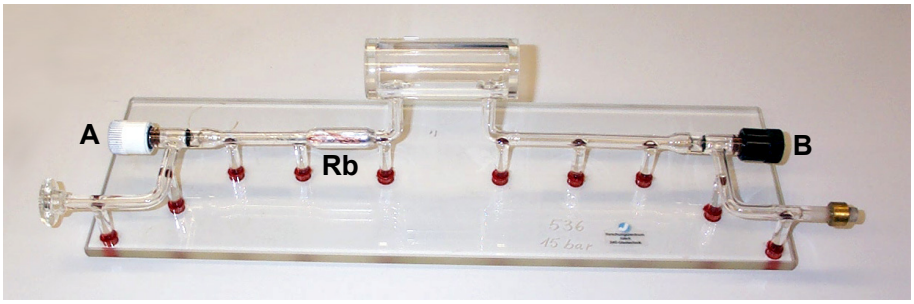

Figure 3.8: Optical pumping cell made from borosilicate glass. The Rb reservoir is visible at the left hand side of the cell.

also features two non-magnetic valves and a reservoir for the rubidium metal (see Fig. 3.8). Both the rubidium reservoir and the OP cell are covered by a glass box, which is heated by a temperature controlled heat gun up to 140–180°C. The optimum temperature depends on the amount of rubidium and the time of the desired OP process [Mühlbauer 07].

The magnetic field, which is required for the Zeeman splitting of the energy levels, is generated by two coils with a Helmholtz-like geometry around the OP cell. The strength of the created magnetic guiding field is usually 2–3 mT at currents of 2–3 A.

3.4.3 Laser system and optical spectrometer

The laser light is generated by a fiber-optically coupled diode laser array (Duo FAP LX Scientific, Cohererent GmbH, Dieburg, Germany) with a maximum output power of 60 W and a spectral linewidth of 2.5 nm (FWHM). By regulating the temperature of the diodes, the wavelength of the laser light can be adjusted, where an increase of 1°C leads to a shift of 0.28 nm. The light is guided by a fiber optics with a length of 1.5 m into a circular polarizing unit, which converts the randomly polarized laser beam into two right-circularly polarized laser beams of equal intensity. This unit consists of a Glan-Thompson polarization prism, that splits the laser beam into two linear polarized components, which are converted afterwards into circular polarized light by two $\lambda/4$ plates.

As only a part of the laser light is absorbed by the rubidium vapor, the transmitted laser spectrum can be analyzed by an optical spectrometer.

The fiber optics which guides the light into the spectrometer is installed in the center of a blackened aluminum plate, which also serves as beam block after the OP cell. The optical spectrometer (HR2000, Ocean Optics Inc., Ostfildern, Germany) provides a resolution down to 0.035 nm with acquisition times in the range of ms. Hereby, real time monitoring of the absorption spectrum during the polarizing process is possible, which allows a precise calibration of the laser wave length and heating temperature. Typical absorption spectra for different heating temperatures and pumping times are shown in Fig. 3.9. The Rb absorption line is clearly visible at a wave length of 794.5 nm. Under optimized conditions (170°, 3 min) the light at the resonance is just fully absorbed. For higher temperatures of 190°, and long laser irradiation times of 38 min, that lead to an additional heating of the cell, the whole spectrum is suppressed and the back part of the cell remains dark. Here, the Rb density is much too high, and the absorption length is shorter than the total length of the OP cell. For lower temperatures (160°, 3 min), the Rb density is too small and the resonant laser light is only in parts absorbed by the Rb atoms.

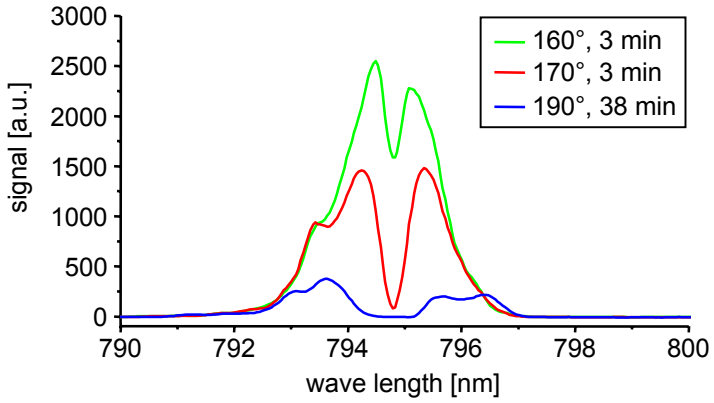

Figure 3.9: Light absorption profiles measured with the optical spectrometer after the OP cell for different cell temperatures and polarizing times.

3.4.4 Batch mode

The polarized xenon is separated from the buffer gases by directing the flow through a cold finger, which is submerged in liquid nitrogen (referred to as *batch mode*). As xenon features a relatively high melting point (161.4 K), it is the only gas in the mixure that freezes at liquid nitrogen temperature (77.36 K), and therefore it can be accumulated as xenon ice. The dewar is located in a homogeneous strong magnetic field of ca. 0.3 T, to avoid relaxation of the HP ^{129}Xe via ^{131}Xe (see Fig. 3.10 A). The field is generated by a specially designed NMR Mandhala magnet [Raich 04], which consists of a stack of Halbach subunits. As depicted in Fig. 3.10 B and C, identical bar magnets are arranged in a certain way to form a strong and homogeneous field. The relaxation times of ^{129}Xe in the solid state are typically in the range of several

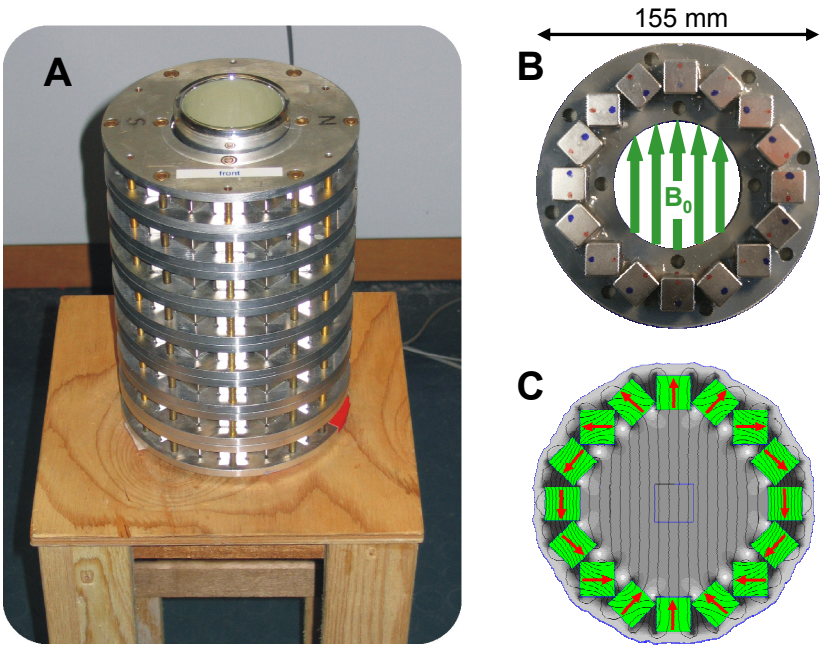

Figure 3.10: NMR Mandhala magnet containing a liquid nitrogen dewar to accumulate HP ^{129}Xe. **A:** The whole magnet consists of 8 subunits and features a total field strength of 0.3 T. **B:** Each subunit respectively consists of 16 identical bar magnets. **C:** The magnetic field in one subunit is very homogeneous and the field is restricted only to the inside of the ring.

hours (see Section 2.4.3). The compact design of the magnet also allows the transportation of HP ^{129}Xe in frozen state.

The amount of accumulated xenon can be controlled by the duration of the polarizing process and the flow. After the polarization process is finished, the buffer gases remaining in the cold finger are removed by shortly evacuating the sample tube, and the xenon is thawed inside of the NMR spectrometer before starting the experiment. Usually 30–60 ml of xenon gas at ambient pressure are accumulated during polarization times of 5–20 min and gas flows of 200–250 ml/min. The achieved polarization rate of ^{129}Xe gas is typically 4–8%, whereby ca. 55% of the obtained polarization are lost during the thawing process [Mühlbauer 07].

3.4.5 Continuous flow mode

Instead of accumulating the HP ^{129}Xe in the solid state and conducting the experiments after the polarization process, the gas mixture can also be guided directly into the NMR spectrometer (referred to as *continuous flow mode*). The setup for this experiments is depicted in Fig. 3.11. The gas mixture flows from the polarizer through 3–7 m of PU tubing into the NMR spectrometer. The pressure of the gas can either be reduced by a non-magnetic Teflon needle valve at the outlet of the polarizer, or by simple hose clamps that compress a part of the tube. The flow rate is regulated by a needle valve at the outlet and monitored by a digital flowmeter. Typically rates of ca. 250 ml/min were used, which delayed the arrival of the HP ^{129}Xe in the NMR probe by 30–120 s, depending on the distance between polarizer and spectrometer.

This whole setup was tested and optimized in the work of [Mühlbauer 07], with respect to all different parameters, like e.g. heating temperature, gas mixture ratios, etc. It also describes the development of a possible online polarization measurement during the polarizing process for the used setup.

3.5 Gas handling system

In order to mix HP ^{3}He with other gases in a controlled fashion, a self-constructed gas handling system was used which operates synchronized with the pulse sequence. This system is described in [Acosta 06a] and was slightly

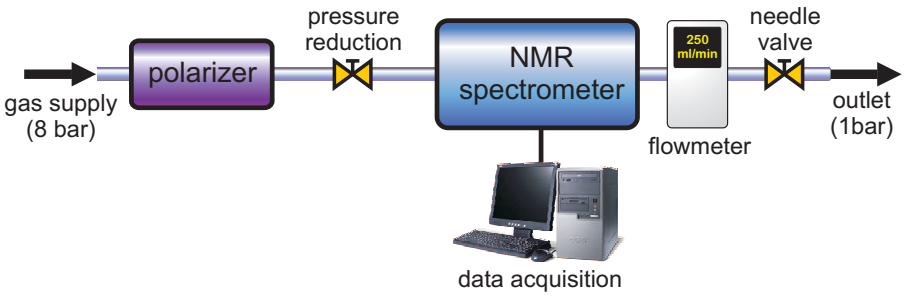

Figure 3.11: Setup for continuous flow experiments. The gas mixture flows directly from the polarizer to the NMR spectrometer, whereby a reduction of the pressure is possible. The flow is regulated by a needle valve at the outlet and monitored by a digital flowmeter.

modified for the experiments presented here (see Fig. 3.12). A spherical sample container resides inside the NMR coil, that is connected to four different pneumatic piston valves A-D and a non-magnetic pressure sensor (Sensortechnics GmbH, Puchheim, Germany). To prepare a gas mixture inside the sample volume with a defined amount of ^{3}He and buffer gas, the following steps have to be accomplished: By opening valve A, the sample volume and the transmission lines are evacuated by a vacuum pump. Once A is closed, a portion of HP ^{3}He with pressure p_{He} is filled into the sample by shortly opening B, which is connected to the ^{3}He transport cell, that is stored in a homogeneous guiding field to reduce relaxation effects (see Fig. 3.4 B). The pressure in the sample container is then released to a certain reference pressure by opening C. Valve C connects to a soft bag, residing inside a box with a constant pressure p_{ref}, which can be adjusted in a range between 0.1 and 2 bar. Therefore, it is important to make sure that p_{He} always exceeds p_{ref}. By this means, the same defined portion of ^{3}He can be used for each experiment. To lower the diffusion coefficient, an additional buffer gas can be pressed into the sample volume by opening valve D for a short time.

The pneumatic piston valves A-D (Festo KG, Esslingen, Germany) are commercially available, and were modified by replacing all magnetic components to operate in high magnetic fields. Hereby, the depolarization of the HP gases and other distortions of the NMR experiment are circumvented, that could arise from the direct vicinity of the valves to the NMR coil. The

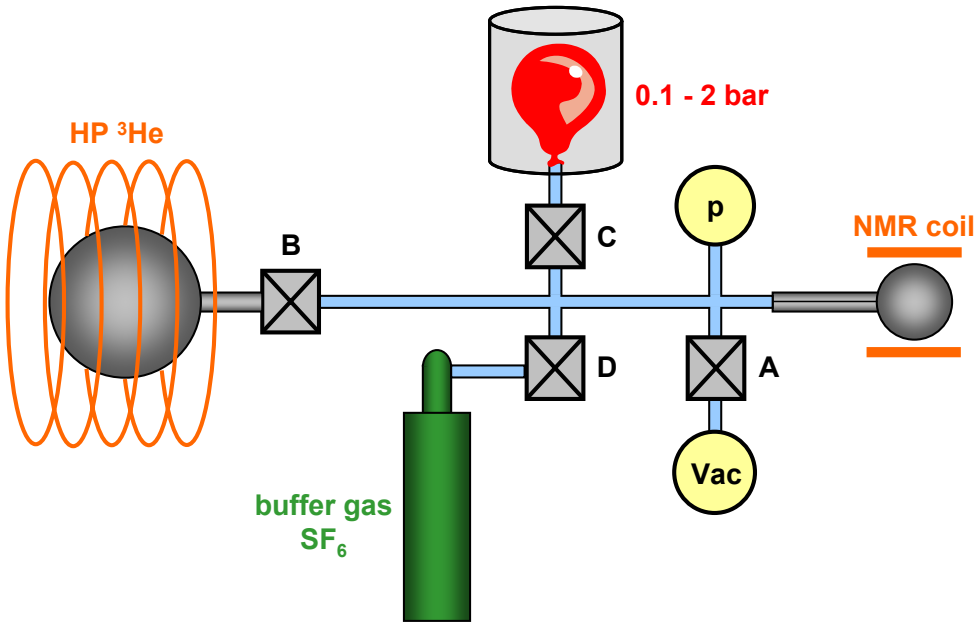

Figure 3.12: Sketch representing the pneumatic valve configuration for preparation of different gas mixtures. *A*, *B*, *C* and *D* are pneumatic valves that are controlled by the spectrometer console. *p* is a pressure sensor and *Vac* a vacuum pump. The red balloon symbolizes a soft bag inside a box with controlled pressure for pressure equalization.

total volume of the mixing system is minimized to ca. 15 ml, which leads to a pressure drop of ca. 30 mbar in the ^{3}He bottle for each filling. Therefore, about 70 equal sample fillings with 1 bar ^{3}He are feasible from a usual ^{3}He transport cell with a pressure of ca. 3 bar.

The pressurized air, which closes and opens the piston valves (see Fig. 3.13), is controlled by a set of magnetic valves residing outside of the strong magnetic field. These electric valves are switched by a voltage of 24 V, which is controlled manually by a switch box or automatically via the NMR spectrometer console. In this way, the mixing procedure can be completely automated and synchronized to the pulse sequence, to enable fast, stable and reliable experiments.

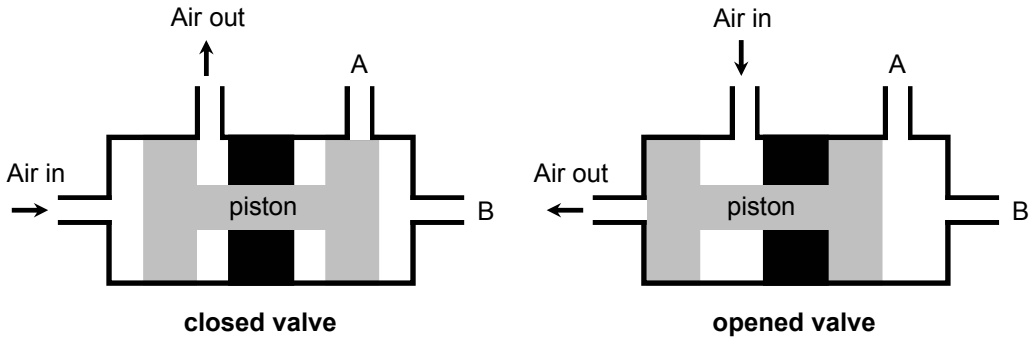

Figure 3.13: Piston valves to control the gas mixing during NMR experiments. **Left:** Closed valve, the passage from conduit A to conduit B is blocked by a piston which is pushed to the right by pressurized air from the left inlet. **Right:** Opened valve, conduit A and conduit B are connected because the piston is pushed to the left by pressurized air from the top inlet.

3.6 Flip angle calibration in HP gases

An important prerequisite for the measurements of the DDF in ^{3}He (Section 5.3) is a precisely calibration of the RF flip angle. In usual NMR experiments with thermally polarized samples, the procedure to calibrate the flip angle is quite simple: A series of spectra with different RF pulse lengths is recorded and the signal maximum is plotted versus the respective pulse length to obtain a *nutation spectrum*. The flip angle dependence on the pulse length can be determined by fitting these values to a sinusoidal function or by just reading off the maximum and zero values for the 90° and 180° pulses. To obtain such a nutation spectrum for HP gases is a little bit more difficult, as the magnetization is irretrievable destroyed by the RF pulses, which usually prohibits the application of pulses with large flip angles. Therefore, the calibration is conducted with small flip angles only and the values for large flip angles are determined by fitting the measured values to the theoretical curve. This method works quite well for the calibration of small flip angles but features a certain error for large flip angles, which makes it unsuitable for our experiments.

As our setup allows an easy refilling of the sample cell with HP gas, a

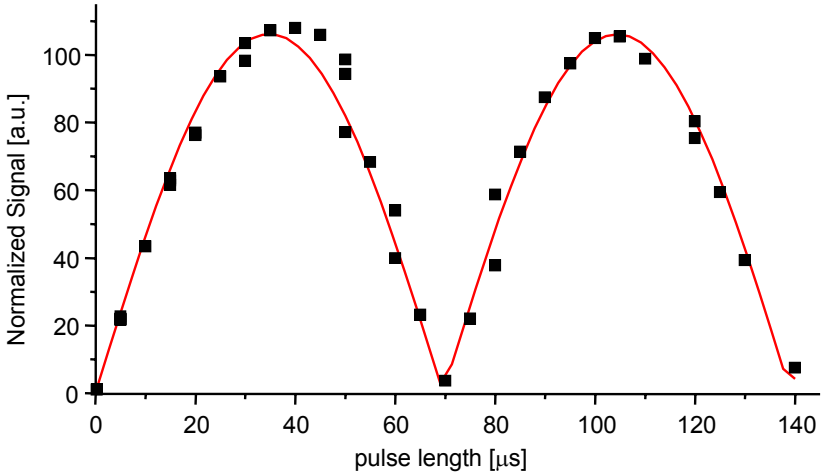

Figure 3.14: Nutation spectrum recorded in HP ^{3}He. The normalized signal maximum values are plotted versus the RF pulse length. The red line is the fitted flip angle calibration curve.

real nutation spectrum was measured also in HP gas. Therefore, for each calibration value two spectra were acquired: The first one with a constant small flip angle of about 1° as a measure for the relative polarization, and the second one with a variable pulse length. The signal amplitude of the second spectrum was normalized by the amplitude of the first one. As the T_1 relaxation times were in the range of 10 min, the measurements are not time-critical and up to 8 calibration values were measured for each gas portion, depending on the used RF pulses. An example of a nutation spectrum recorded in HP ^{3}He is depicted in Fig. 3.14. The normalized signal amplitude values were fitted by the function

$$S = A \cdot |\sin(t/t_{180} \cdot \pi)| \tag{3.1}$$

for the signal dependence on the pulse length. For the shown measurement a time of $t_{180} = (69.6 \pm 0.2)$ μs for a flip angle of 180° is obtained. The measured values lie in good agreement with the theoretical curve, approving a correct flip angle calibration.

Chapter 4

Pseudo spin echoes in gases

4.1 Motional effects on spin echoes

The spin echo (SE) phenomenon, as described in Section 2.1.5, is a well known and studied effect in NMR. Since its discovery in 1950 [Hahn 50], the respective refocusing principle is included in various pulse sequences, applied in modern NMR and MRI experiments. The effect of spin motion on the SE signal, caused by diffusion or other dynamical processes, is subject of many studies in the liquid and solid state [Carr 54, Stejskal 65, Collignon 81]. Following [Spiess 83], the effect of motion on the SE can be classified in three different regimes, which are distinguished by the ratio of the correlation time of the dynamical process τ_c [Kampen 92] and the inter pulse delay time τ of the SE sequence.

For non- or very slow moving spins, $\tau_c \gg \tau$, the total signal amplitude of the FID is refocused after exactly 2τ, when other relaxation effects are negligible ($T_1, T_2 \gg 2\tau$).

For faster dynamical processes, but still $\tau_c > \tau$, the amplitude of the SE at time 2τ is suppressed by the movement of the spins in the field gradient, because the spins experience different magnetic fields during their motion and their phases are not refocused completely. This effect is used to measure diffusion coefficients, as already described in Section 2.3.4. In these experiments, usually the amplitude of the SE at time 2τ is measured either in dependence of the magnetic field gradient (PGSE) or of the echo time τ (CPMG). The shape and the time of the maximum amplitude of the SE are

not influenced much by the spin motion in this regime.

If the dynamical process, however, happens on the same or even a faster timescale than τ, $\tau_c \geq \tau$, the signal shape itself and the apparent echo position changes considerably. This phenomenon was first discovered in deuteron NMR of molten linear polyethylene (LPE) in 1981 [Collignon 81, Spiess 83, Cohen Addad 93], and named *pseudo solid echo* effect. Here, the maximum of the detected signal occurs at times $t < 2\tau$. An analytical description of this effect is only possible for simple two-site exchange processes [Spiess 81]. For more complicated motions, the SE signals can only be calculated by computer simulations. In liquids, the translational motion due to diffusion is in general too slow to observe effects in the fast regime. In gases, however, these motional regimes might be accessible due to the much faster translational diffusion.

Along these lines, in this chapter the behaviour of SEs in gases is studied in detail for all three different motional regimes by changing the diffusion coefficient using different pressures and gas mixtures (see Section 2.3.5). Note that these experiments take advantage of HP gases (^{3}He and ^{129}Xe), as the signals of thermally polarized gases are too small to acquire SEs within reasonable measurement times τ (see Appendix A).

For the theoretical description of the diffusion effect in the fast regime, the usual Stejskal-Tanner equation is insufficient, as it only calculates the signal suppression at the time 2τ (see Eq. 2.69). Therefore, the equation was extended to describe the whole time evolution of the SE signal under the effect of diffusion in linear gradients. If non-linear gradients are present or if the sample exhibits a non-rectangular profile, there is no simple analytical solution and the SEs have to be simulated by a computer calculation, which is based on a random walk model for the diffusing spins.

The understanding of this effect is on the one hand of general theoretical interest, while on the other hand, it is a prerequisite for different applications, like e.g. SE sequences in MRI of HP gases or measurements of intermolecular double quantum coherences in HP ^{3}He, as shown in Chapter 5.

4.2 Diffusion suppression function

While the calculations of the signal suppression by diffusion usually are restricted to the time 2τ of the SE formation, in this section, the total time dependence of the diffusion suppression is calculated. Hereby, a constant linear magnetic field gradient $G = \partial B/\partial z$ is assumed during the experiment (see pulse sequence in Fig. 2.15 B).

In general, the detected signal after the inversion pulse $E(t)$ is given by the product

$$E(t) = M(t)A_{Diff}(t)\,, \tag{4.1}$$

where $M(t)$ is the time evolution of the magnetization without diffusion effects, and $A_{Diff}(t)$ is the time-dependent diffusion suppression function.

For an ensemble of spins with a rectangular profile along the gradient direction with the length $2d$ (e.g. a cylindrical tube), the phases of the spins in the rotating frame are given by

$$\phi(z,t) = \gamma G z t\,, \tag{4.2}$$

where the initial phases $\phi(z,0) = 0$. The magnetization $dM(z,t)$ in a slice dz is described by

$$dM(z,t) = \cos(\phi(z,t))dz = \cos(\gamma G z t)dz\,. \tag{4.3}$$

The total magnetization at time t is calculated by integrating over the whole sample,

$$M(t) = \int_{-d}^{d} dz\ \cos(\gamma G z t) = \frac{2}{\gamma G t}\ \sin(\gamma G d t)\,. \tag{4.4}$$

As at time $t = 0$, $M(t = 0) = 1$ should apply, a factor of $1/2d$ is included to normalize $M(t)$, which leads to

$$M(t) = \frac{1}{\gamma G d t}\sin(\gamma G d t)\,. \tag{4.5}$$

This function is valid for times $t < \tau$ and corresponds to the FT of the spin distribution profile along the z-axis. At time $t = \tau$, the spin phases are inverted by a 180° pulse,

$$\phi(z,\tau) \rightarrow -\phi(z,\tau)\,. \tag{4.6}$$

For times $t > \tau$, the magnetization is then given by

$$\begin{aligned} M(t) &= -\int_0^T dM(t) + \int_T^t dM(t) \\ &= \frac{1}{\gamma G d(t-2\tau)} \sin(\gamma G d(t-2\tau)) \,. \end{aligned} \tag{4.7}$$

In summary, the magnetization without diffusion is described by

$$M(t) = \begin{cases} \frac{1}{\gamma G d t} \sin(\gamma G d t) & , t < \tau \\ \frac{1}{\gamma G d(t-2\tau)} \sin(\gamma G d(t-2\tau)) & , t > \tau \,. \end{cases} \tag{4.8}$$

The diffusion suppression function $A_{Diff}(t)$ is determined following the approach in [Kimmich 97], but without the restriction to the time 2τ. The function $A_{Diff}(t)$ describes the effect of diffusion on an isochromate of spins[1], depending on their motion, which is governed by stochastic processes. The function is given by the integral

$$A_{Diff}(t) = \int_{-\infty}^{\infty} d\phi \; p(\phi, t) \; e^{i\phi} \,, \tag{4.9}$$

where $p(\phi, t)$ is the probability for the occurrence of phase ϕ at time t. This expression can be simplified by expanding the phase factor and using the fact that $p(\phi, t)$ is an even function of the phase shifts (in the case of free diffusion it is a simple gaussian) and so the odd moments of the exponential function vanish:

$$\begin{aligned} A_{Diff}(t) &= \int_{-\infty}^{\infty} d\phi \; p(\phi, t) \left(1 + i\frac{\phi}{1!} - \frac{\phi^2}{2!} - i\frac{\phi^3}{3!} + \frac{\phi^4}{4!} \pm \ldots \right) \\ &= 1 - \frac{\langle \phi^2 \rangle}{2!} + \frac{\langle \phi^4 \rangle}{4!} - \frac{\langle \phi^6 \rangle}{6!} \pm \ldots \end{aligned} \tag{4.10}$$

The even moments of a gaussian distribution can be obtained from its second moment, e.g.

$$\langle \phi^{2n} \rangle = 1 \cdot 3 \cdot 5 \cdots (2n-1) \langle \phi^2 \rangle^n \qquad (n = 1, 2, 3, \ldots) \,. \tag{4.11}$$

Using this relation, Eq. 4.10 can be transformed to

$$A_{Diff}(t) = e^{-1/2 \langle \phi^2(t) \rangle} \,. \tag{4.12}$$

[1] A bunch of spins with equal precession frequencies at time $t = 0$ and position z.

Therefore, it is sufficient to calculate $\langle\phi(t)^2\rangle$. For the SE sequence, two different cases before and after the inversion pulse have to be considered,

$$\langle\phi(t)^2\rangle = \begin{cases} \gamma^2 G^2 \left\langle \left(\int_0^t z(t')\, dt' \right)^2 \right\rangle & , t < \tau \\ \gamma^2 G^2 \left\langle \left(\int_0^\tau z(t')\ dt' - \int_\tau^t z(t')\ dt' \right)^2 \right\rangle & , t > \tau\,. \end{cases} \tag{4.13}$$

The relative minus sign in the latter case accounts for the fact that at time τ all phases are inverted due to the π-pulse. Using the relation

$$\langle z(t')z(t'+T)\rangle = D[2t' + T - |T|]\,, \tag{4.14}$$

which follows from the Einstein-Smoluchowski equation $\langle z^2\rangle = 2Dt$ (Eq. 2.59). The solution of the resulting integrals finally leads to the diffusion suppression function for arbitrary times t,

$$A_{Diff}(t) = \begin{cases} \exp\left[-\frac{1}{3}\gamma^2 G^2 D t^3\right] & , t < \tau \\ \exp\left[-\frac{1}{2}\gamma^2 G^2 D(4\tau^3 - 4\tau^2 t + \frac{2}{3}t^3)\right] & , t > \tau\,. \end{cases} \tag{4.15}$$

This function also includes the well known echo suppression formula for a constant gradient at time 2τ as a special case (see Eq. 2.70),

$$A_{Diff}(2\tau) = \exp\left[-\tfrac{2}{3}\gamma^2 G^2 D\tau^3\right]\,. \tag{4.16}$$

The behaviour of the calculated echo signal $E(t)$ for typical values of a SE in ^{3}He with a long echo time ($\tau = 10$ ms, $D = 2$ cm^2/s, $G = 0.7$ mT/m, $d = 8$ mm) is shown exemplary in Fig. 4.1. The usual echo maximum at time 2τ is almost suppressed completely by the function $A_{Diff}(t)$. This leads to an apparent shift of the SE maximum, which legitimates the term of *pseudo spin echoes*. The local maximum of $A_{Diff}(t)$ is derived by setting its derivative to zero,

$$\frac{\mathrm{d}A_{Diff}}{\mathrm{d}t} = -\tfrac{1}{2}\gamma^2 G^2 D(-4\tau^2 + 2t_{max}^2)A_{Diff}(t) \stackrel{!}{=} 0\,, \tag{4.17}$$

which leads to a time,

$$t_{max} = \sqrt{2}\tau\,. \tag{4.18}$$

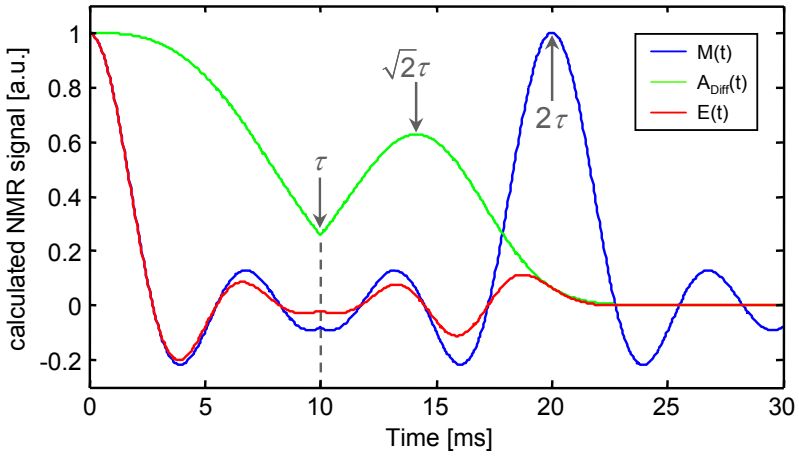

Figure 4.1: Calculated diffusion suppressed SE signal $E(t)$ for ^{3}He parameters ($\tau = 10$ ms, $D = 2$ cm^2/s, $G = 0.7$ mT/m, $d = 8$ mm); blue: Echo of a cylindrical sample in a linear gradient without suppression; green: Diffusion suppression function with a local maximum at time $\sqrt{2}\tau$; red: Suppressed SE signal showing an apparent maximum shift.

4.3 Pseudo spin echoes in linear gradients

As an experimental verification for the calculations of the previous section, SEs in HP ^{3}He were measured in presence of a constant linear gradient for different diffusion coefficients D. By using the setup described in Section 3.5, it was possible to vary D over the range of one order of magnitude (0.1 cm^2/s – 4 cm^2/s), by either admixing it with a heavier buffer gas (SF_6) at elevated pressures or reducing the total pressure of the gas portion. A slice selective excitation pulse (see Section 2.2.4) was applied, to ensure that all spins, which were excited by the first r.f. pulse, stay in the detection volume during the experiment. Otherwise, the measurements would not correspond to the theoretical assumptions. The thickness of the excited slice $2d$ was controlled by the amplitude of the slice selection gradient. To avoid additional oscillations in the time signal, which would arise from small frequency offsets in the experiment, only magnitude signals are depicted in the following.

Before the actual experiments on gases, control experiments on water were performed to check the slice selection and limitations of the used setup. Such control experiments in water showed, that the slice selection technique leads to a reduction of the detected signal for times $t > 2\tau$. Fig. 4.2 shows the magnitude signal, acquired with a SE sequence without slice selection of a water sample, while Fig. 4.3 depicts the asymmetric magnitude SE signal, which was obtained with a slice selective r.f. pulse. This effect could be traced back to an initial phase distribution of the spins after the excitation pulse, which is caused by imperfections of the slice selection gradient pulses. Because the product of the amplitude of the slice selection gradient and the excitation pulse length is in the same range as the product of the constant linear gradient amplitude and the time τ, this initial phase distribution can affect the signal for times $t > 2\tau$. Computer simulations also showed that the signal for $t > 2\tau$ is sensitive to small variations of the initial phase distribution of the spins.

The profiles of two slices in HP ^{3}He along the main field axis are shown in Fig. 4.4. The slice selection was accomplished using a Gaussian smoothed sinc-shaped r.f. pulse with 2 lopes and a duration of 600 μs and gradient strengths of 14 and 21 mT/m. With these parameters, slices with a thickness of ca. 58% and 43% of the whole sample profile were excited. The peak at ca. -7000 Hz is a frequency artifact due to the demixing of the signal in the spectrometer.

For these two slices, SEs were acquired for different diffusion coefficients D in presence of a defined linear gradient, which is strong enough so that all effects of non-linear gradients were negligible. The pulse sequence used is depicted in Fig. 4.5. The 180° pulse had a duration of 67.5 μs and the constant linear gradient exhibited a magnitude of 0.7 mT/m. All SEs were acquired with a two-step phase cycle to remove the strong signal arising after the 180° pulse, due to pulse imperfections. The measurements with the stronger slice selection gradient were acquired with $\tau = 10.3$ ms and the thickness of the excited slice $2d$ was ca. 10 mm (see Fig. 4.6 A). For the weaker slice selection gradient, the experiment was conducted with $\tau = 10.9$ ms and $2d \approx 16$ mm (shown in Fig. 4.6 B).

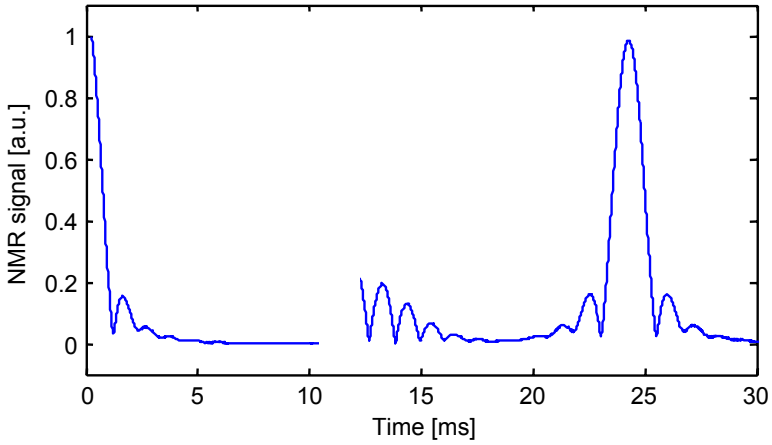

Figure 4.2: Magnitude SE signal of a water sample in a constant gradient of 0.7 mT/m without slice selection (τ = 12.2 ms). The signal directly after the inversion pulse is due to imperfections of the 180° pulse.

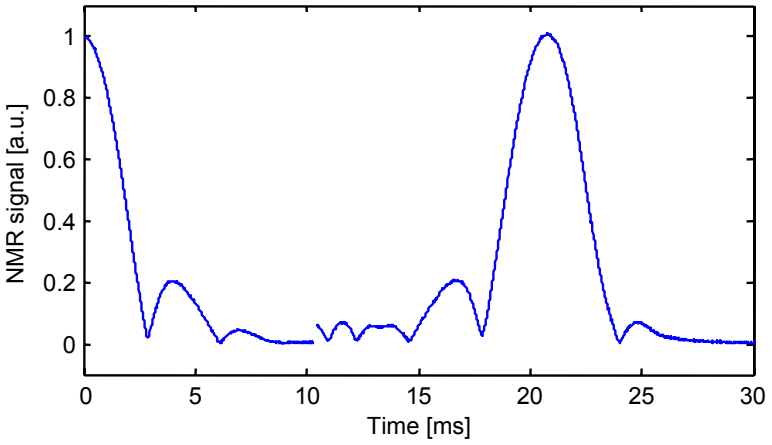

Figure 4.3: Magnitude SE signal of a water sample in a constant gradient of 0.7 mT/m, using a slice selective excitation pulse (τ = 10.4 mm, $2d \approx 8.9$ mm $\approx 44\%$ of the length of the detection volume). Note that the suppression of the signal for times $t > 2\tau$ arises from an initial spin phase distribution induced by the slice selection technique.

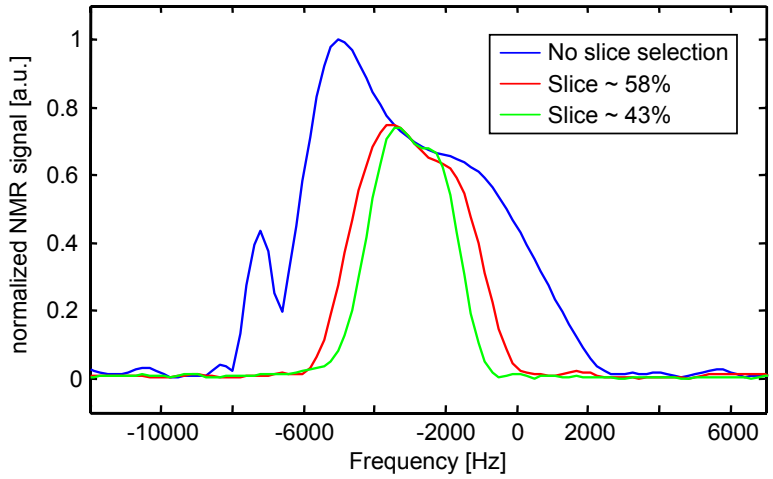

Figure 4.4: Sample profiles, acquired with a slice selection gradient echo sequence in HP ^{3}He; blue: Sample profile without slice selection gradient (frequency artifact at -7000 Hz); red: Slice selection with a gradient of 14 mT/m; green: Slice selection with a gradient of 21 mT/m.

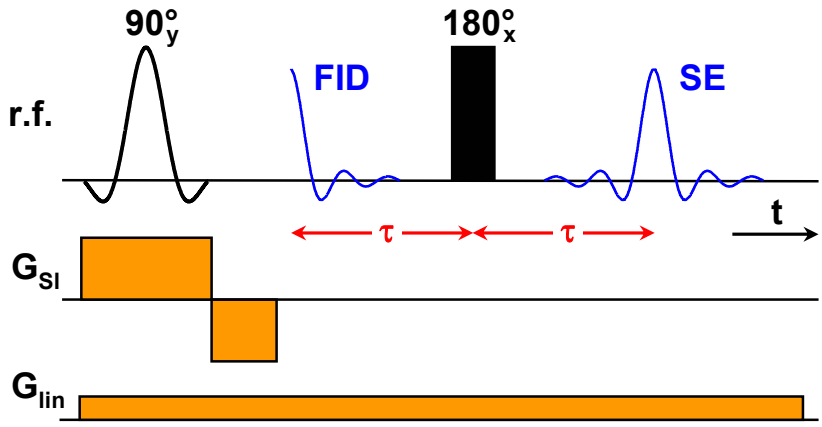

Figure 4.5: SE sequence with a slice selective excitation pulse in presence of a constant linear gradient. The times of the applied pulses are exaggerated in the illustration.

The SEs for different D show the behaviour predicted by the calculations: The apparent signal maximum shifts with increasing D to earlier times, which is caused by the increasing impact of the diffusion suppression function. For the diffusion coefficient of helium at ambient pressure ($D = 1.8$ cm^2/s), the signal at time 2τ is suppressed to the point where the amplitude of the secondary maximum of the sinc-function exceeds the main echo. If only the signal after the inversion pulse was detected (as it is usually the case for most pulse sequences), the echo signal would appear to be shifted in time. From this observation arises the term of *pseudo spin echoes*. As it was already observed in the SEs in water, the signal for times $t > 2\tau$ is additionally suppressed by the imperfect slice selection.

For a validation of the derived diffusion suppression function for arbitrary times (see Eq. 4.15), the detected FID signal before the inversion pulse for the slowest diffusion coefficient is taken as an initial state and mirrored at time τ to obtain the theoretical echo signal without diffusion. As the excited slice profile deviates considerably from an ideal rectangular shape (see Fig. 4.4), an ideal sinc function, which could be calculated analytically, cannot be used as the initial state. The resulting echo without diffusion is then multiplied with the analytical diffusion suppression function for times $t > \tau$ (Eq. 4.15) and compared to the experimental data. The calculation parameters resemble the experimental values for the linear gradient, the diffusion coefficient and the echo time τ. Fig. 4.7 shows both the experimental and theoretical SE signal for different diffusion coefficients for the smaller slice, while Fig. 4.8 depicts the data of the larger one. For both cases, the calculated signals agree almost perfect with the experimental data, hereby approving the analytical suppression function with its local maximum at time $\sqrt{2}\tau$. The only deviation is caused by the already mentioned effect for times $t > 2\tau$, where the signal is additionally suppressed by an initial phase distribution of the spins caused by the slice selection, similar to the SEs in water (see Fig. 4.3).

As Fig. 4.6 shows, the main and the secondary echo maximum decay with increasing diffusion, yet with different constants. Therefore, for a particular diffusion coefficient, the amplitude of the main echo maximum at time $t_1 = 2\tau$ equals the amplitude of the secondary maximum at time t_2. This special diffusion coefficient, referred to as D_{12}, could serve as a value to quantify the motional regime of a certain spin system. If one can calculate D_{12}

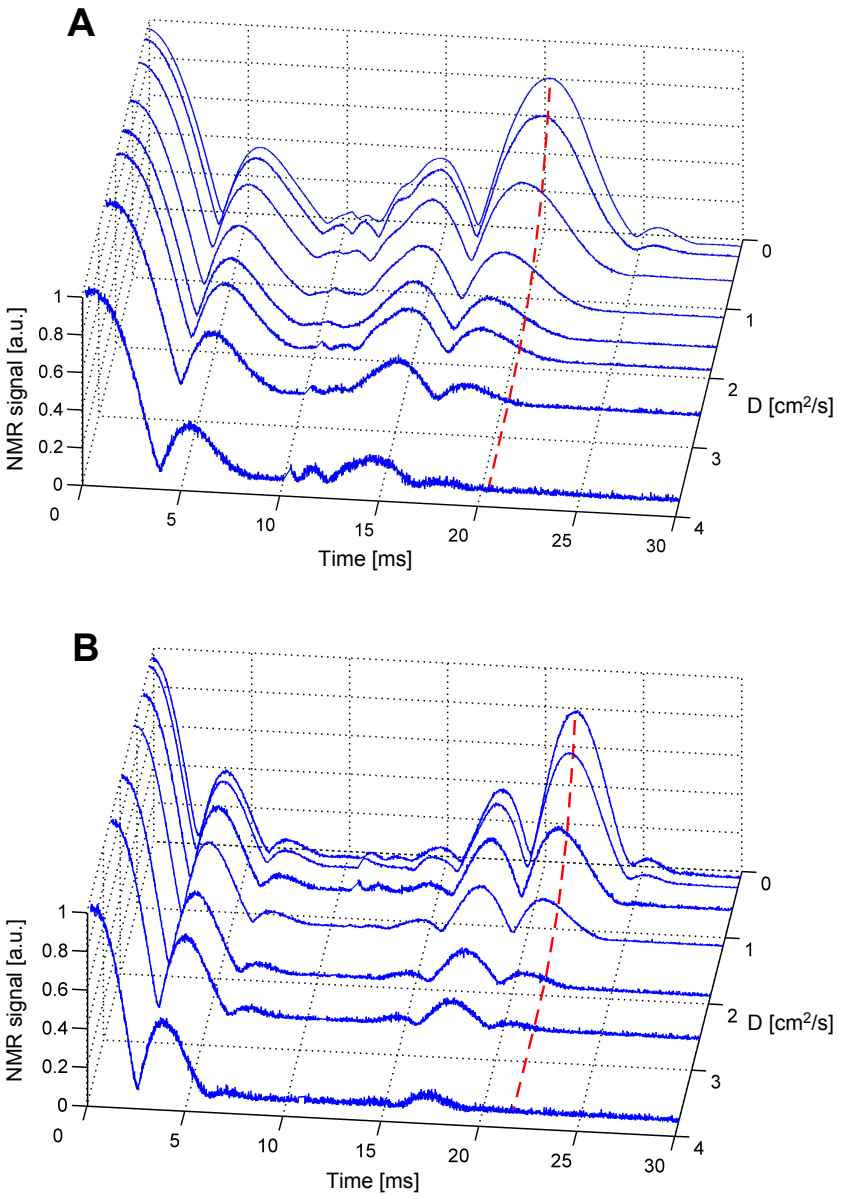

Figure 4.6: Magnitude FID and SE signals in HP ^{3}He in presence of a constant linear gradient for different diffusion coefficients D. The dashed red line marks the time 2τ, where in absence of diffusion the maximum signal is expected. **A:** Thickness of the excited slice $2d \approx 10$ mm, $\tau = 10.3$ ms; **B:** $2d \approx 16$ mm, $\tau = 10.9$ ms.

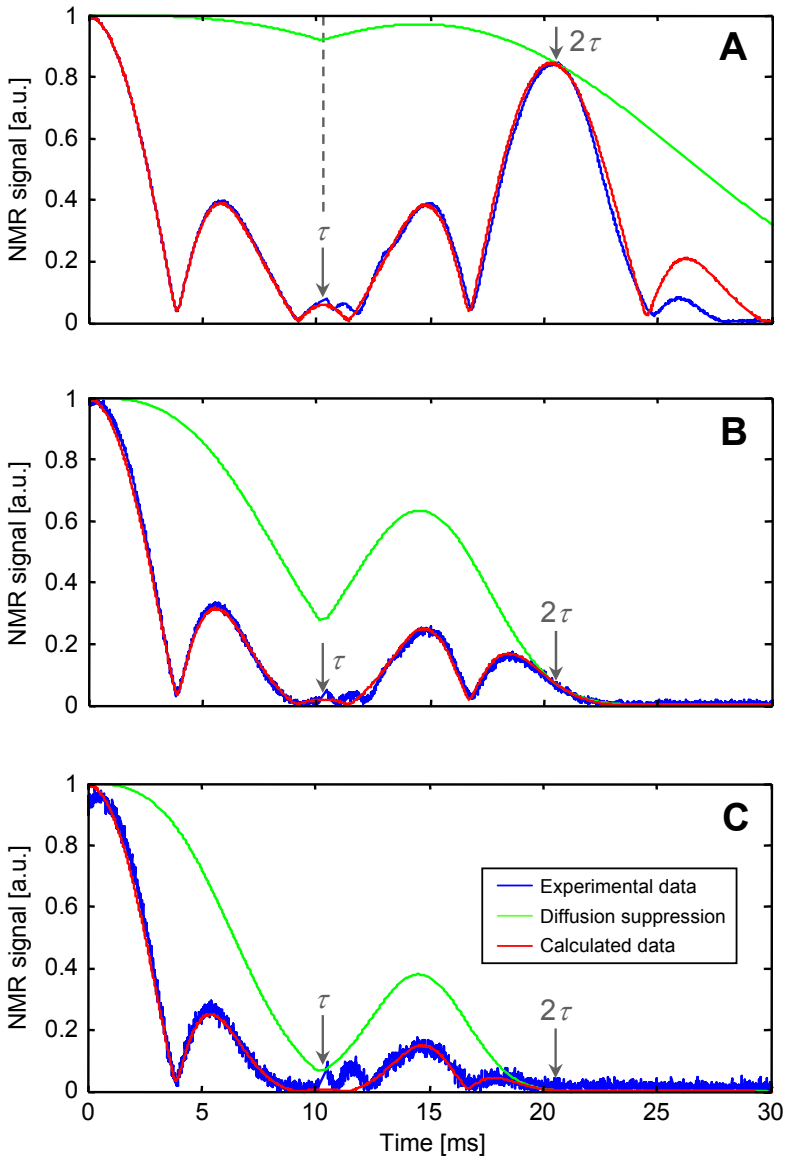

Figure 4.7: Comparison of experimental (blue) and calculated (red) SE magnitude signals in HP ^{3}He. The calculations are the product of the diffusion suppression function (green) and the mirrored FID signal for times $t < \tau$ and $D = 0.115$ cm^2/s. The signal was acquired in presence of a constant linear gradient of 0.7 mT/m and only a slice with a thickness of ca. 10 mm was excited. The different measurements were conducted with different diffusion coefficients D. **A:** $D = 0.115$ cm^2/s; **B:** $D = 1.8$ cm^2/s; **C:** $D = 3.8$ cm^2/s.

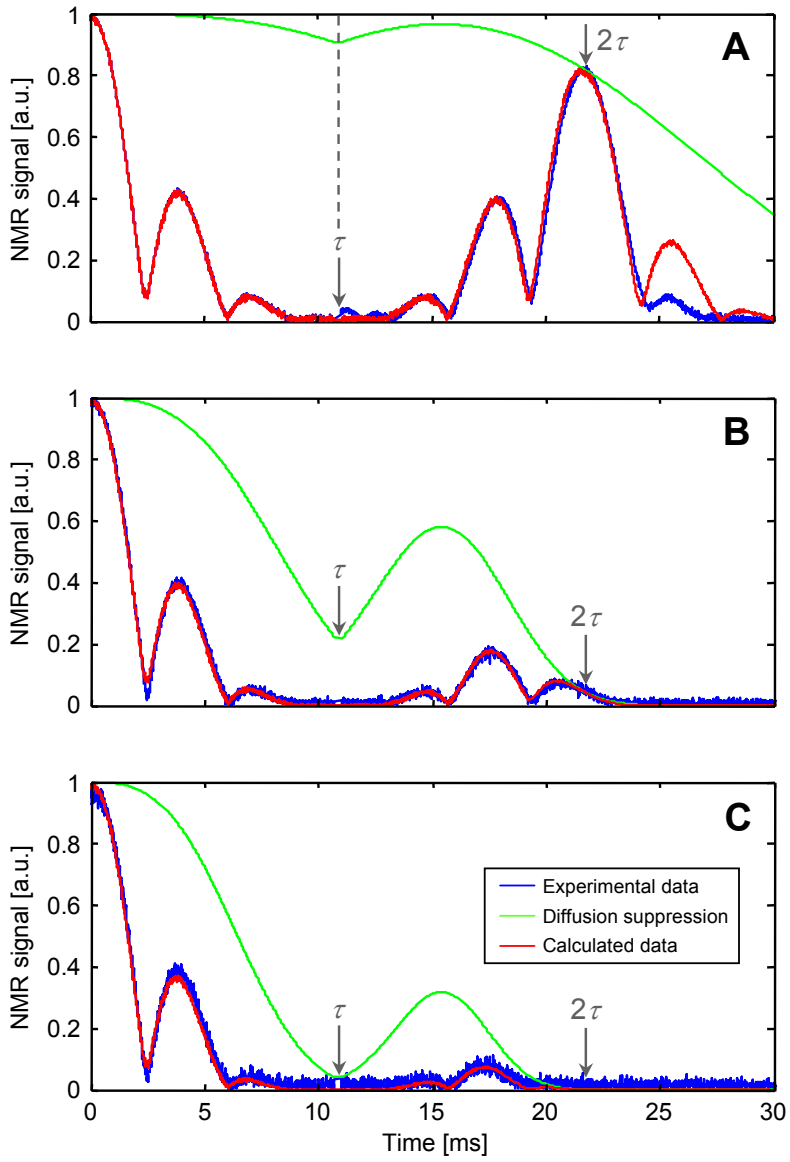

Figure 4.8: Comparison of experimental (blue) and calculated (red) SE magnitude signals in HP ^{3}He. The calculations are the product of the diffusion suppression function (green) and the mirrored FID signal for times $t < \tau$ and $D = 0.115$ cm^2/s. The signal was acquired in presence of a constant linear gradient of 0.7 mT/m and only a slice with a thickness of ca. 16 mm was excited. The different measurements were conducted with different diffusion coefficients D. **A:** $D = 0.115$ cm^2/s; **B:** $D = 1.8$ cm^2/s; **C:** $D = 3.8$ cm^2/s.

analytically, it can indicate, if for a particular diffusion coefficient D and fixed values of γ, G and d, it is still reasonable to measure the echo signal at the usually expected echo time 2τ.

Thus, D_{12} is derived from the intersection of the two exponential functions, which describe the decay of the signals with increasing D at time t_1 and t_2. The time t_2 of the secondary maximum is calculated approximately from the time of the first minimum of $\sin(\gamma G d t)$,

$$t_2 \approx 2\tau - \frac{3\pi}{2d\gamma G}\,. \tag{4.19}$$

By inserting these times into Eq. 4.15, one obtains the decay functions

$$A(t_1) = \exp\left[-\tfrac{2}{3}\gamma^2 G^2 \tau^3 D\right] \tag{4.20}$$

$$A(t_2) = \exp\left[-\tfrac{1}{2}\gamma^2 G^2 (\tfrac{4}{3}\tau^3 - \tfrac{18}{3}\tau_s\tau^2 + 9\tau_s^2\tau - \tfrac{27}{12}\tau_s^3)D\right]\,, \tag{4.21}$$

$$\text{where} \quad \tau_s = \frac{\pi}{d\gamma G}\,.$$

The intersection diffusion coefficient is the value, where

$$M_1 A(t_1) = M_2 A(t_2)\,. \tag{4.22}$$

M_1 and M_2 are the amplitudes of the total and the secondary FID maximum. Rearranging the equation to make D the subject results in the following formula for the intersection value,

$$D_{12} = -\ln\left(\frac{M_1}{M_2}\right)\frac{1}{\gamma^2 G^2 \tau_{12}^3}\,, \tag{4.23}$$

$$\text{where} \quad \tau_{12}^3 = -\tfrac{9}{3}\tau_s\tau^2 + \tfrac{9}{2}\tau_s^2\tau - \tfrac{27}{24}\tau_s^3\,. \tag{4.24}$$

To compare this value with the experimental results, the measured SE signals at times t_1 and t_2 for different values of D are fitted by an exponential decay function, type

$$E(D) = E_0 \cdot e^{-D/D_{dec}} + E_1\,. \tag{4.25}$$

The intersection of the two fitted decay curves is then compared with the calculated value from Eq. 4.23. As it is shown in Fig. 4.9, the calculated intersection value fits exactly the measured one, for both the smaller (Fig. 4.9 A) and the larger slice (Fig. 4.9 B). As the signal amplitudes are plotted

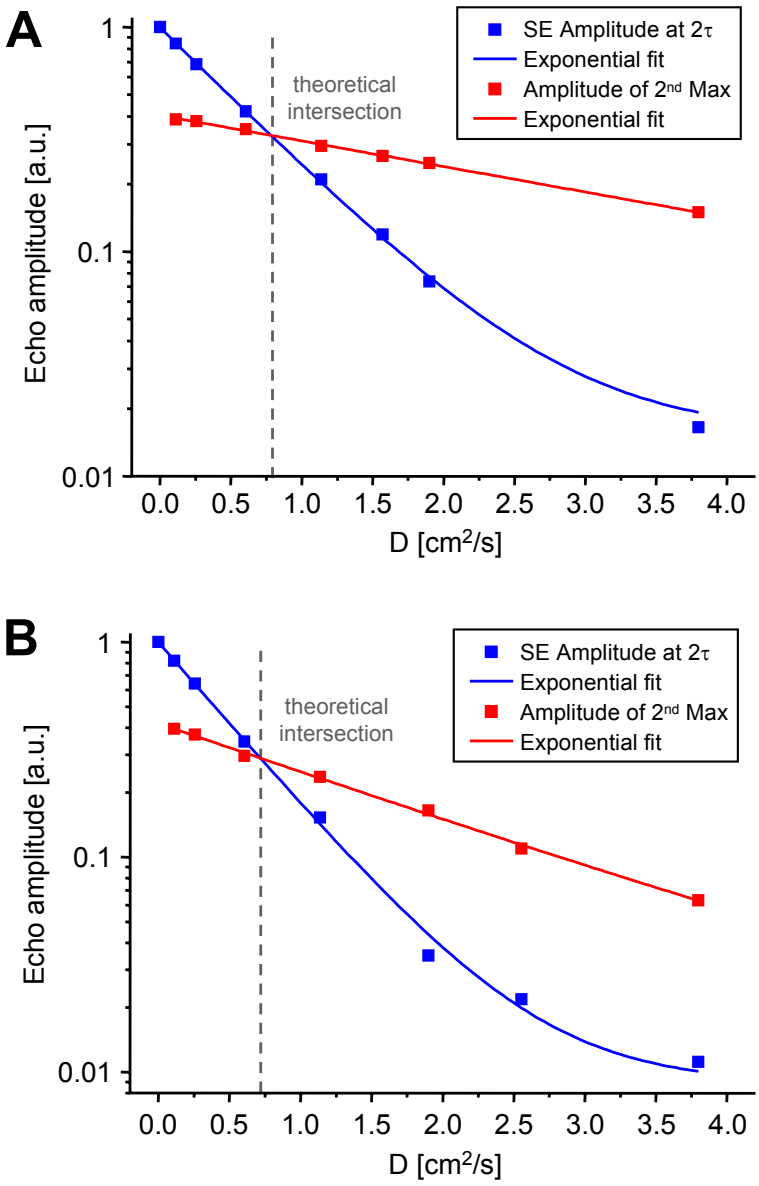

Figure 4.9: Amplitudes of the SE signal at time 2τ (blue) and at the time of the secondary maximum (red), in dependence of the diffusion coefficient D. The amplitudes are plotted on a logarithmic scale, so that the exponential curves result in straight lines. The calculated theoretical intersection value is marked by a grey dashed line. **A:** Thickness of the excited slice $2d \approx 10$ mm; **B:** $2d \approx 16$ mm.

on a logarithmic scale, the fitting curves are given by straight lines. The fit values D_{dec} agree for all four curves with the calculated values from Eq. 4.20 and 4.21 within their error margins. This almost perfect agreement is a second proof for the validity of the calculations described in Section 4.2.

It was shown in this section, that the extension of the Stejskal-Tanner equation for arbitrary times is valid, and describes exactly the experimentally obtained pseudo SEs. Additionally, the calculation of the value D_{12} allows a simple assessment of the motional regime in advance of such experiments, in analogy to the correlation time τ_c for rotational diffusion effects. If the diffusion coefficient of the intended measurement $D \ll D_{12}$, it is still reasonable to detect the signal at time 2τ, while for $D > D_{12}$ one should check the echo signal at times $t < 2\tau$.

4.4 Pseudo spin echoes in non-linear gradients

Usually, NMR experiments are conducted in magnetic fields, where the remaining gradients are minimized by a *shimming* procedure. Hereby, several small additional gradient fields in different directions and of different orders are adjusted in such a way, that the gradient of the main field is compensated. Only by means of this procedure, the high resolution in the range of 0.1 ppm and less is attainable in modern NMR spectroscopy. However, the remaining field gradient is not purely linear, which makes the analytical solution for the diffusion suppression of SEs (Eq. 4.15) insufficient to describe the signal, even in a well shimmed field. Additionally, the sample geometry in real experiments does usually not feature a rectangular profile along the magnetic field axis, but can be spherical of or even totally irregular, like e.g. in medical MRI.

Therefore, the diffusion suppressed SE signals in non-linear gradients and non-rectangular sample shapes were calculated by computer simulations. In this section, the principle of the simulations is described and the results are compared to experimental SEs, which were obtained from HP gases in spherical sample containers in the small and undefined magnetic field gradient of a shimmed magnet.

4.4.1 Spin echo simulations

Usually, the simulations performed to describe the effect of diffusion on NMR experiments are based on stochastic methods, which are motivated by a random walk model of freely diffusing spins. In these methods, an ensemble of spins is randomly moved in space and their phase accumulated according to the local magnetic field at each time step. Recent simulations of NMR spin echoes, including diffusion effects, can be found in literature [Balinov 93, Gudbjartsson 95]. While Balinov calculates the effect of restricted diffusion, Gudbjartsson shows a new method to speed up such calculations, using the so called convolution method. But in all published works, only the suppression of the SE amplitude by particle diffusion is calculated and not the whole time evolution of the NMR signal. The same holds true for all known published analytical solutions, which also restrict themselves to the description of the SE amplitude at time τ after the inversion pulse. Therefore, a simulation of the SE time evolution was set up to investigate the effect measured in ^{3}He.

The simulation program was developed in cooperation with J. Schmidt [Schmidt 07] and is similar to the ones mentioned above, where the spin-bearing, non-interacting "pseudo-particles" are allowed to perform a random walk inside of certain geometrical restrictions with reflecting boundaries. Constant field gradients of different polynomial order can be applied to resemble the remaining field inhomogeneities or application of static magnetic field gradients. The fine tuning of the magnitude of these gradients was determined by comparing the simulations to the experiment. The simulations were conducted for cylindrical and spherical boundary conditions. Further information on the structure of the program can be found in Appendix B.

The simulations were tested and calibrated by calculating the SE of a water sample and comparing the results to the experimental measurements. The sample container in the experiment was of the same size as the one later used for the gas measurements, a glass sphere with an inner diameter of 12 mm. The simulated signals were obtained by using 10^5 spin trajectories, a time step of 0.1 ms, $D = 2.3 \cdot 10^{-9}$ m^2/s, a τ value of 50 ms, magnetogyric ratio $\gamma(^1\mathrm{H}) = 26.75 \cdot 10^7$rad/T·s and a relaxation time of $T_2 = 1.72$ s. Fig. 4.10 shows the comparison of experimental and simulated SEs for different settings. Clearly, both spherical boundary conditions and non-linear gradients are needed to reproduce the experimentally observed sharp peak of the SE.

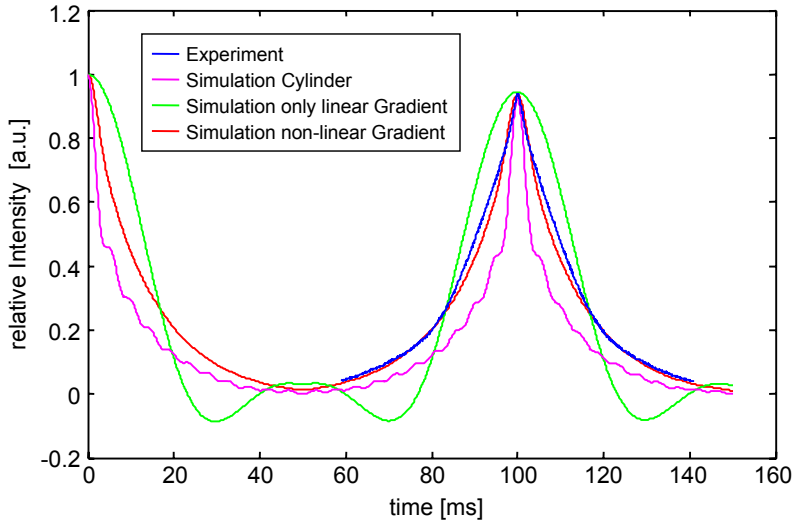

Figure 4.10: Comparison of simulated Magnetization time evolution with the experiment; blue: Experimental signal; magenta: Simulation with cylindrical boundaries; green: Simulation with spherical boundaries and only linear gradients; red: Simulation with spherical boundaries and non-linear gradients up to 5th order (for details see Fig. 4.11).

With optimized gradients of up to the fifth order and a spherical geometry, the simulation meets quite accurately the experimental results. The non-linear gradients might be due to steps in the magnetic susceptibility at the sample/container boundaries and not only to inhomogeneities of the static magnetic field. The spatial dependence of the gradient values of different orders is shown in Fig. 4.11, where the z-axis represents the actual size of the sample. From this, it is obvious that the higher order gradients cannot be neglected for the used sample dimensions, whereas in smaller samples, a linear gradient approximation suffices.

4.4.2 Spin echoes in HP ^{3}He and ^{129}Xe

The SEs in HP ^{3}He and ^{129}Xe were acquired in a spherical samples container with an inner diameter of 12 mm. The magnetic field with a strength of 4.7 T was shimmed, reaching a line width of the NMR signals of ca. 0.2–0.3 ppm. The echo time τ was set to a longer time (50 ms) than in the previous

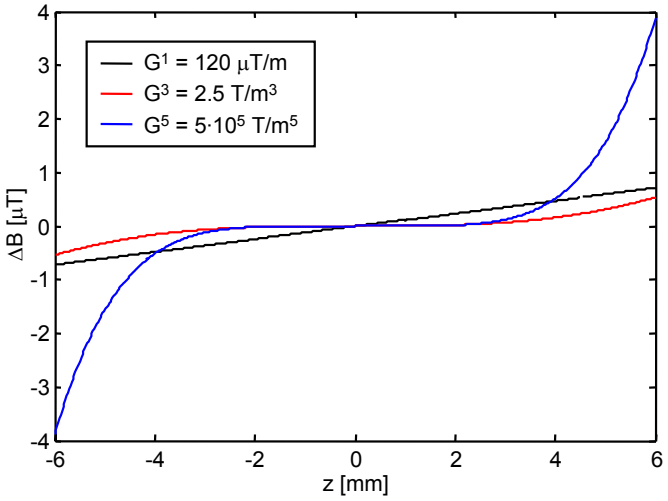

Figure 4.11: Dependence of the gradient values used for the non-linear gradient simulation in Fig. 4.10 on the spatial coordinate z; black: Linear gradient; red: Cubic gradient; blue: Gradient of fifth order.

experiments for two reasons. First because of the smaller gradients present, and second, because the intermolecular double quantum echo signal in ^{3}He is expected on that time scale (studied in the following Chapter 5). In these SE experiments, only the echo signal directly after the inversion pulse at time $t = 0$ was acquired.

Fig. 4.12 shows the SE signal of HP ^{3}He for different diffusion coefficients D. The suppression of the echo signal is clearly visible, which leads to a considerable shift of the maximum amplitude. To ensure that this effect really arises only from the change of D and that all other effects can be excluded, D was varied over almost two orders of magnitude using different kinds of techniques. Fig. 4.14 depicts the signal maximum times depending on D. Although points in different colors were recorded with different methods for varying D, they all show the same behaviour. While e.g. for red points D was changed by varying the pressures of pure ^{3}He, the blue and green points represent experiments where ^{3}He was admixed with SF_6 in two different sample containers. By these measurements all other effects which could be responsible for such a behaviour are excluded:

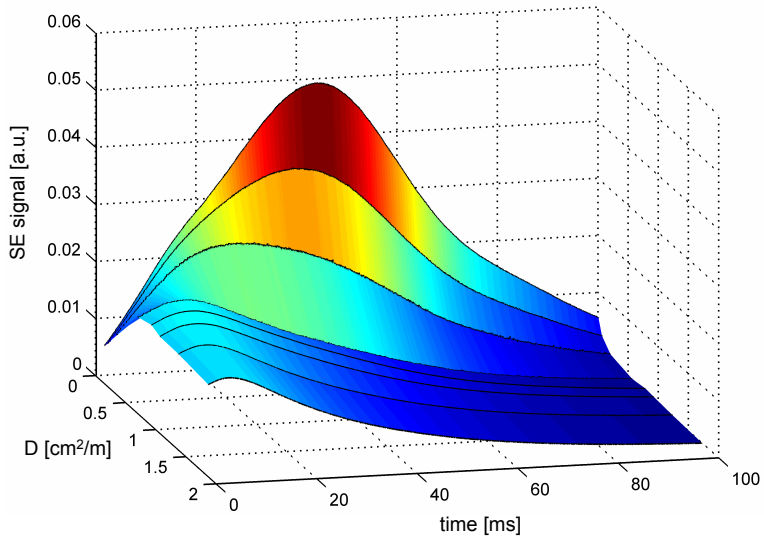

Figure 4.12: Detected SE signal in HP ^{3}He after the inversion pulse (at time $t = 0$ s) of a spin echo sequence for different diffusion coefficients. The echo is usually expected at a time $\tau = 50$ ms.

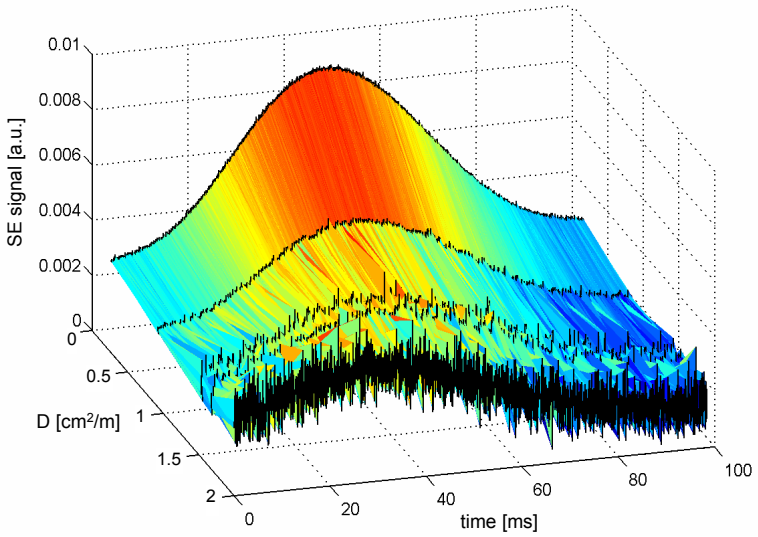

Figure 4.13: Detected SE signal in HP ^{129}Xe after the inversion pulse (at time $t = 0$ s) of a spin echo sequence for different diffusion coefficients. The echo is usually expected at a time $\tau = 50$ ms.

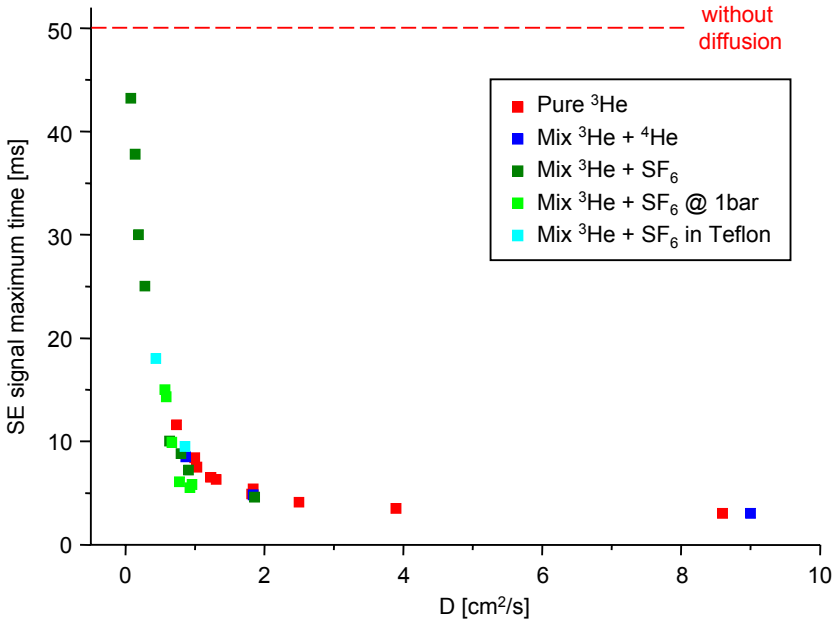

Figure 4.14: Maximum signal times of a SE experiment in ^{3}He for $\tau = 50$ ms depending on diffusion coefficient D. The dashed lines shows the expected echo time. Different colors distinguish different methods to accomplish changes in D; red: Pure ^{3}He at different pressures p; blue: Different mixtures of ^{3}He and ^{4}He; dark green: Different mixtures of ^{3}He and SF_6 and different p; light green: Different mixtures of ^{3}He and SF_6 $p = 1$ bar; cyan: Same as dark green but inside a teflon container instead of glass.

- Dipolar couplings between the ^{3}He spins are not critical, as the shift is the same for pure and admixed ^{3}He and the coupling depends directly on the distance between ^{3}He spins (see eq. 2.16).

- Radiation damping can be excluded, as the observed effect does not change with lowering the polarization of ^{3}He, which should lead to a decrease of radiation damping.

- Effects of the sample container, e.g. paramagnetic impurities in the walls of the glass surface [Schmiedeskamp 06b, Schmiedeskamp 06a] are not critical as the shift occurs in exactly the same manner for glass and teflon vessels.

The same experiments with HP ^{129}Xe show a much less pronounced impact of the diffusion coefficient on the apparent SE maximum position (see Fig. 4.13). Here, D was changed by a reduction of the pressure down to minimum 0.1 bar, which leads to a quite low SNR for measurements at high D. The comparison of the signal maximum times in ^{129}Xe and ^{3}He in Fig. 4.15 shows that the signal for ^{129}Xe shifts only down to times of about 25 ms after the inversion pulse, while the minimum times for ^{3}He are in the range of 5 ms. This effect can only arise from the different magnetogyric ratios of the two nuclei or a different remaining gradient for the two experiment series.

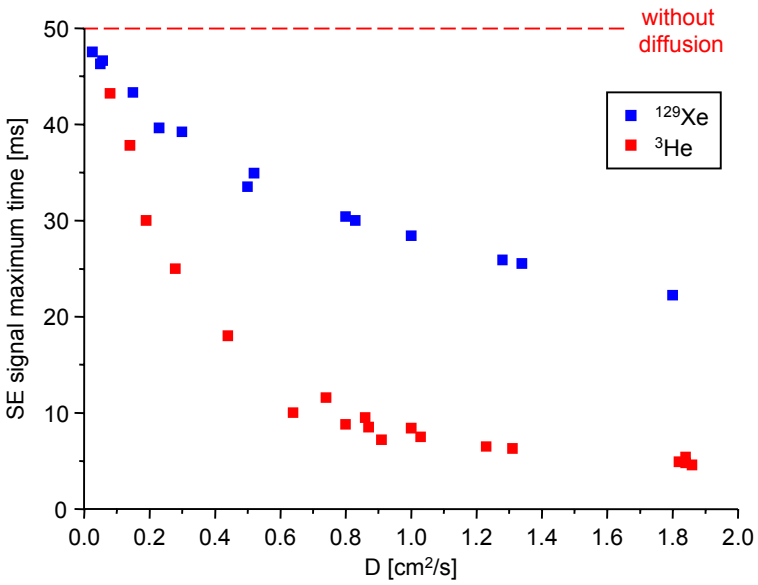

Figure 4.15: Maximum signal times of a SE experiment in ^{129}Xe (blue) and ^{3}He (red) for $\tau = 50$ ms depending on diffusion coefficient D. The dashed line shows the expected echo time.

4.4.3 Simulation of spin echoes in HP ^{3}He and ^{129}Xe

In order to check if the measured effect can be reproduced by computer simulations, the SE signal for different diffusion coefficients D was calculated as described in Section 4.4.1. The following parameters were changed in comparison to the water simulations: To obtain the same accuracy for the

much higher D, the number of spins was increased to $N = 5 \cdot 10^5$. The magnetogyric ratio $\gamma(^3\text{He}) = 20.37 \cdot 10^7 \text{rad/T·s}$ and the relaxation time was set to $T_2 = 1$ s, which agrees with the experimental value of $T_2 = 0.97$ s, measured by a CPMG sequence with a short $\tau = 1$ ms. Gradients of first and third order were needed to have a good agreement with the experimental echo shape.

Fig. 4.16 depicts the results of these simulations for different D. The shift of the maximum signal to shorter times with increasing D is well reproduced (see experimental results in Fig. 4.12). A more quantitative evaluation of the simulations can be accomplished by comparing the obtained signal maximum times with the experimental values as shown in Fig. 4.17. The values of the simulations agree well with the characteristics of the experimental curve, which demonstrates the capability of the calculations to reproduce the diffusion suppression effect for in HP ^{3}He.

In order to check if the differences of the SE signals in ^{3}He and ^{129}Xe (see Fig. 4.15) really arise from the magnetogyric ratio, a simulation series with the parameters of ^{129}Xe was performed ($\gamma(^{129}\text{Xe}) = -7.452 \cdot 10^7 \text{rad/T·s}$). The simulated signal maximum times are compared to the experimental values in Fig. 4.18. One simulation series was calculated with the gradient parameters of the ^{3}He simulations ($G^1 = 100$ μT/m, $G^3 = 5$ T/m^3, green stars), while for the second series, the parameters were newly optimized ($G^1 = 47$ μT/m, $G^3 = 15$ T/m^3, magenta stars), as the ^{129}Xe measurements were performed with other shim currents. The optimization of the parameters was conducted for the SE signal at $D = 0.057$ cm^2/s. The errors of the experimental values, depicted exemplary for one series, result from the uncertainty in the assignment of the SE maximum position. The two different experiment series were conducted at different days and are therefore distinguished in the graph to emphasize the reproducibility of the measurements. The error bar, which is shown at $D = 0.8$ cm^2/s of the simulation series with the ^{3}He gradient values, reflects the typical deviation of the ^{3}He SE simulations from the experimental values (see Fig. 4.17).

The simulations with the optimized gradient parameters reflect quite well the trend of the experimental data. The deviation increases for larger D, but the values still lie within the experimental error margins. Even the deflection of the values for the gradient parameters of the ^{3}He calculations is still reason-

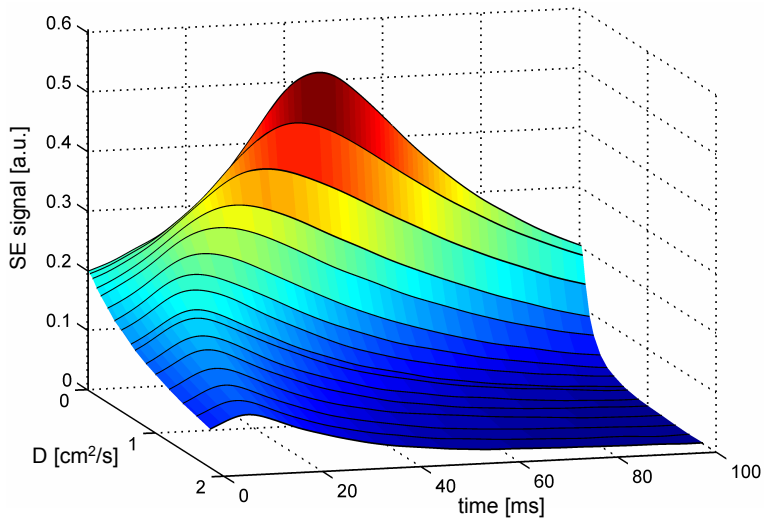

Figure 4.16: Simulated time evolution of the NMR signal for a spin echo sequence starting at the inversion pulse (at time t = 0 s) for different diffusion coefficients D. The echo is usually expected at a time $\tau = 50$ ms.

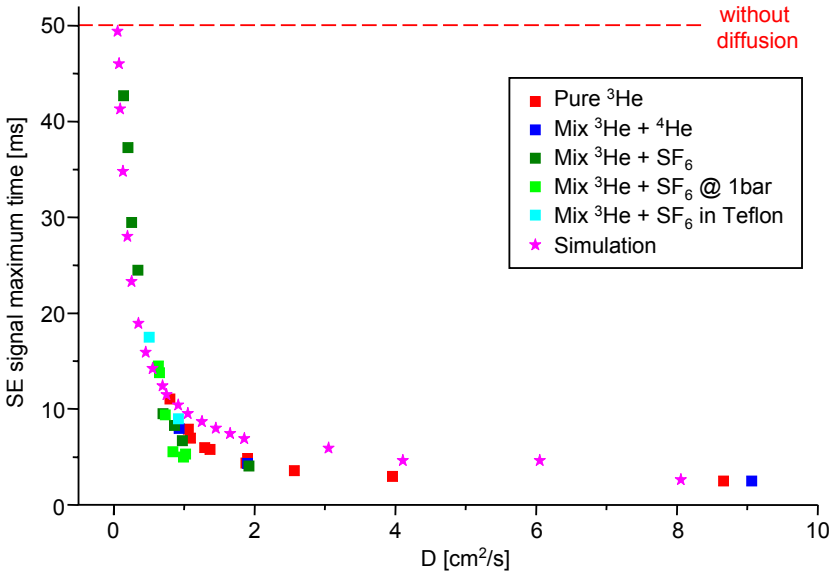

Figure 4.17: Comparison of simulated SE maximum times in ^{3}He with experimental results. Simulated values are marked by magenta stars. Experimental results are labeled as in Fig. 4.14.

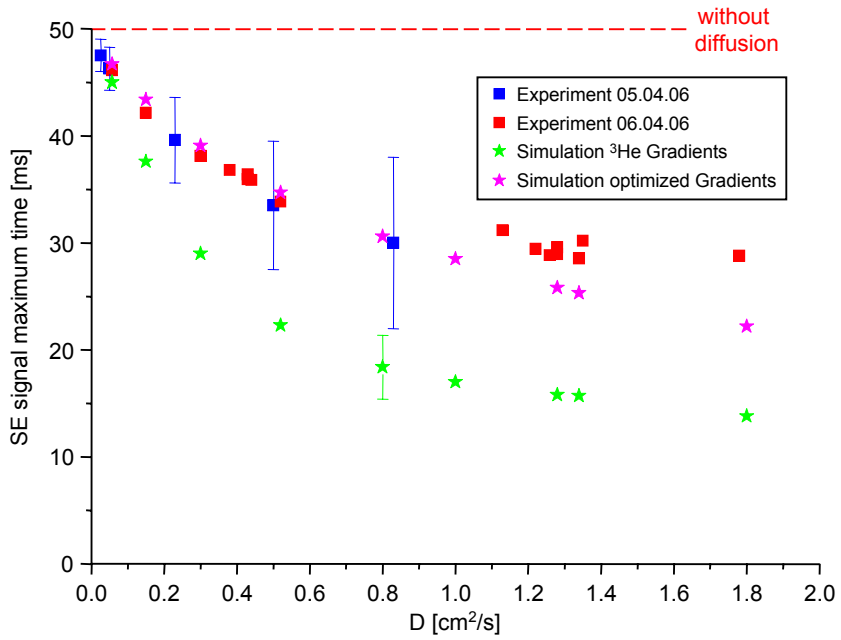

Figure 4.18: Comparison of simulated SE maximum times with experimental results of HP ^{129}Xe measurements. Simulated values are marked by green and magenta stars that differ by gradient parameters. Two different series of experiments conducted at different dates are marked by blue and red boxes. Error bars of the experimental values are shown for the first series. The typical deviation of the simulated values from the experimental helium values is depicted as one error bar.

able, when the typical error of the ^{3}He simulations is considered. Anyway, the signal maximum times changed about 30% for the two different simulation series, where the gradient values were altered about 30–50%. Therefore, an accurate gradient optimization is crucial for the correct outcome of the simulations and has to be repeated for each new experiment series with changed shim values.

In conclusion, the simulations reproduce well the experimental results, also for different nuclei, which implies that also for non-linear gradients and spherical geometries the pseudo spin echo effect is understood and can be predicted by calculations. Further information on the reliability of the simulations, as well as the structure of the program can be found in Appendix B.

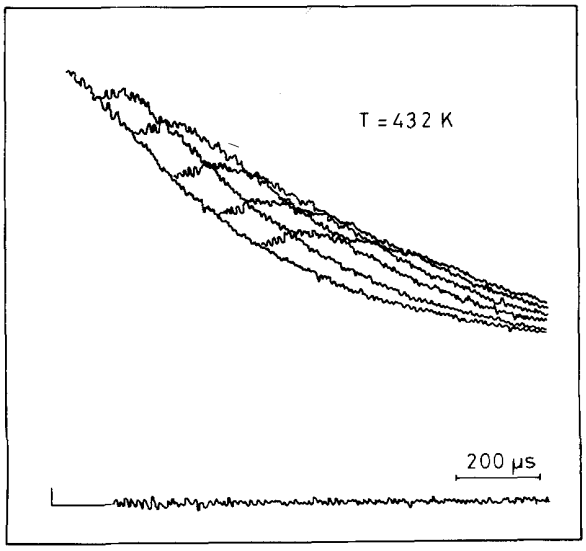

Figure 4.19: ^{2}H pseudo solid echoes of molten LPE for various echo times τ. The echoes for τ = 100, 200, 300, 400, and 500 μs, as well as the FID ($\tau = 0$), are superimposed. The maxima of the pseudo solid echo do not occur at $t = 2\tau$, revealing a correlation time of ca. 100 μs. (Figure adapted from [Spiess 83])

4.4.4 Comparison with pseudo solid echoes

In this section the discovered effect of diffusion on SEs in gases is compared to the *pseudo solid echo* phenomenon, reported in 1981 in deuteron NMR of molten LPE [Collignon 81, Spiess 83, Cohen Addad 93]. It was shown that the coherence of the spin phases during a solid echo experiment ($\pi/2 - \tau - \pi/2$ – Acq) is lost due to motional effects within a certain correlation time of about 0.1 ms (see Fig. 4.19). To quantify this time constant, different measurements with varying echo times τ were conducted. Along these lines, experiments in HP ^{3}He were performed, to figure out if the concept of correlation times also applies for gases. While for experiments in molten LPE, this time constant is given by molecular properties, which cannot easily be changed, in gases it depends on the diffusion coefficient, which can be varied precisely with the developed setup.

Therefore, the full time evolution of the magnetization during a spin echo sequence, starting directly after the excitation pulse, was measured in

a mixture of ^{3}He and SF_6 with a diffusion coefficient $D = 0.35$ cm^2/s (see Fig. 4.20 A). As a guide for the eye, the usual echo time without diffusion suppression 2τ was marked as a small arrow in the graphs. For short times τ, the signal maximum still appears at the expected positions, although the amplitude is already reduced, while for increasing times τ, the signal at the echo time is suppressed significantly, leading to earlier signal maximum times. This experiment series was also simulated to verify the measurements (see Fig. 4.20 B). The simulations resemble almost perfectly the experimental results, approving the high accuracy of the simulations. Note that despite the diffusion suppression, the intersection of two SEs with different echo time τ_1 and τ_2 still occurs at $\tau_1 + \tau_2$, as it would be the case for unsuppressed signals.

For a quantitative analysis of these experiments, the signal maximum times were extracted and plotted versus the expected echo time τ for both experiment and simulation (see Fig. 4.22 A). Additionally, the same experiment and simulation series were repeated with a diffusion coefficient $D = 1.8$ cm^2/s, which corresponds to pure ^{3}He gas at ambient pressure. The SEs are shown in Fig. 4.21, while the extracted maximum values are presented in Fig. 4.22 B. As expected, for smaller diffusion coefficients, the signal maximum time reaches larger values than for faster diffusion. In both cases, experimental and simulated values show the same trend, leveling off at a certain time. As a rough approximation, this value can be used to determine the correlation times for the different diffusion coefficients, which amounts to about 20 ms for $D = 0.35$ cm^2/s and to about 8 ms for $D = 1.8$ cm^2/s.

4.5 Conclusions

The effect of diffusion on usual SEs in gases was studied for different motional regimes. It was verified that the observed change of the SE signal in terms of amplitude, shape and maximum position (known as *pseudo SE* effect) arises from fast translational motion of the spins on the timescale of the NMR experiment. The pseudo SE signals were reproduced by an extension of the Stejskal-Tanner equation to arbitrary times, for the special case of linear gradients and samples with a rectangular shape in direction of the magnetic field. The almost perfect agreement of the calculated signals with the experimental data for different diffusion coefficients shows the validity

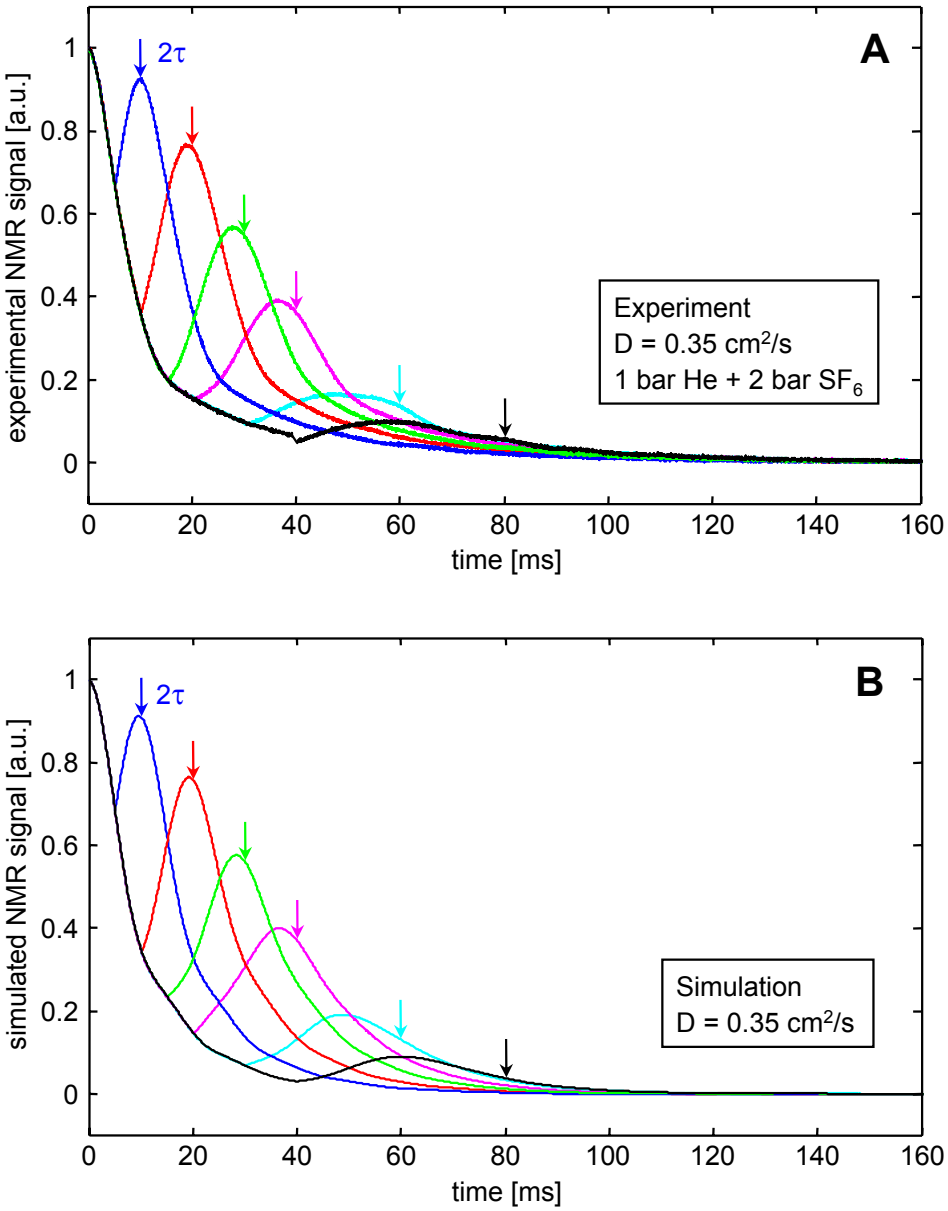

Figure 4.20: **A:** Experimental detected spin echoes in a mixture of ^{3}He and SF_6 with $D = 0.35$ cm^2/s for different echo times τ between 5 and 40 ms. **B:** Simulated spin echoes for the same parameters. The expected echo times 2τ without diffusion are marked by arrows in the corresponding colors.

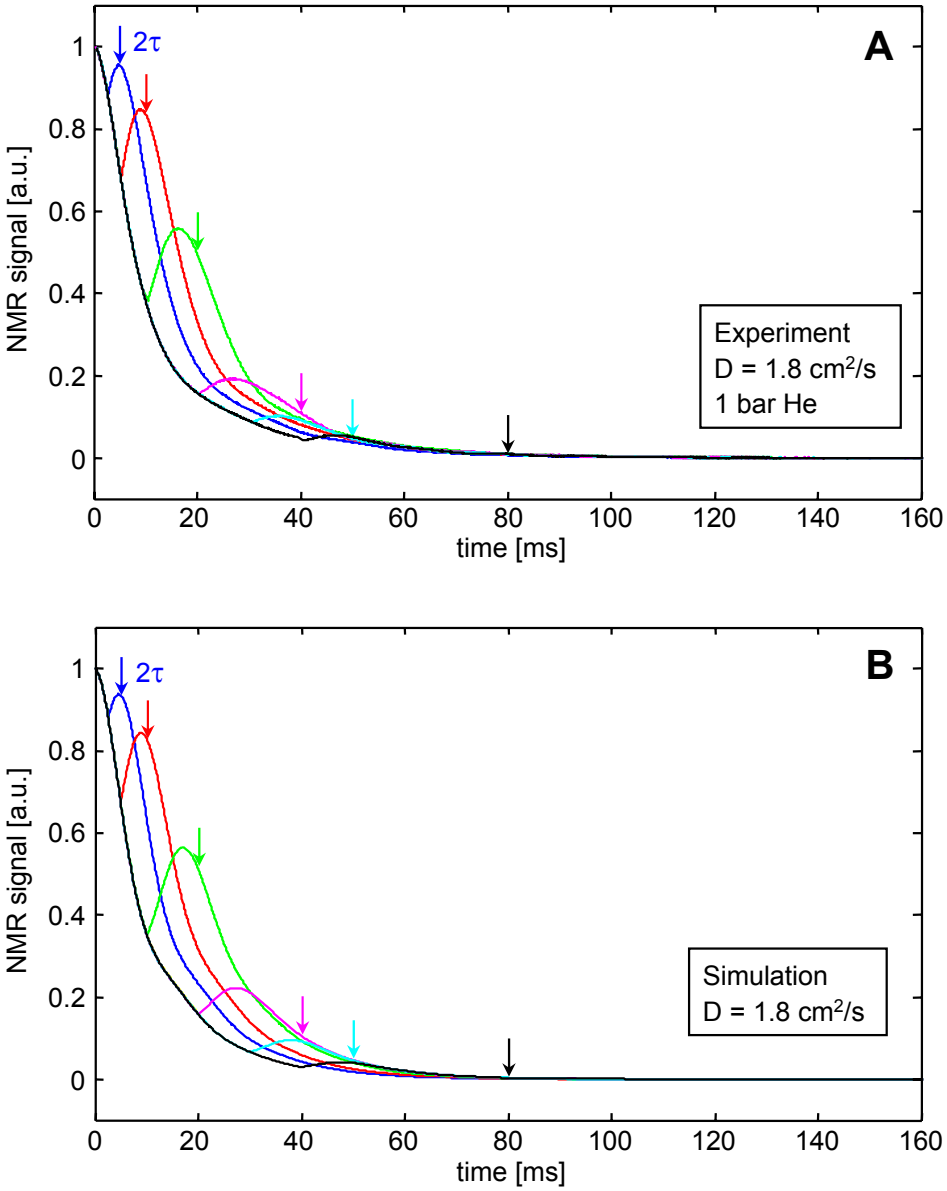

Figure 4.21: **A:** Experimental detected spin echoes in pure ^{3}He with $D = 1.8$ cm^2/s for different echo times τ between 5 and 40 ms. **B:** Simulated spin echoes for the same parameters. The expected echo times 2τ without diffusion are marked by arrows in the corresponding colors.

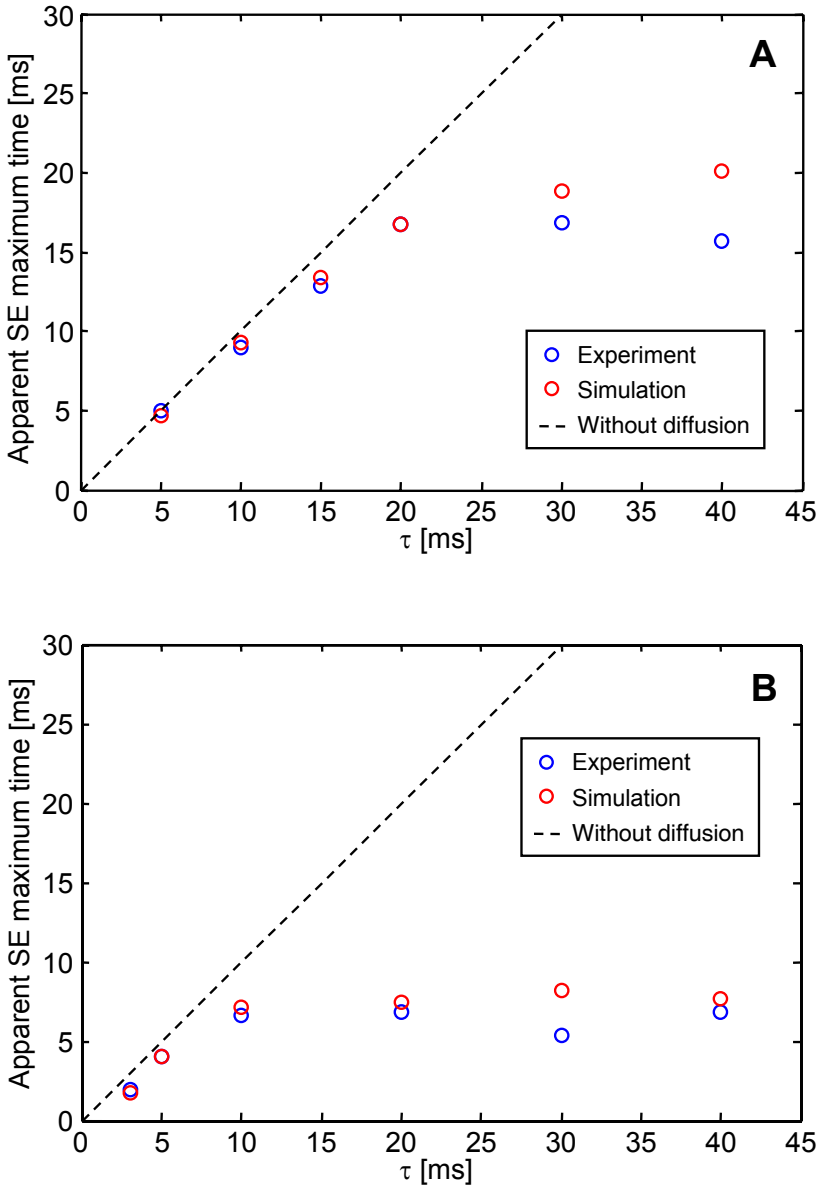

Figure 4.22: SE signal maximum times in dependence of the inter pulse delay time τ. **A:** $D = 0.35$ cm^2/s; **B:** $D = 1.8$ cm^2/s; blue: Experimental values; red: Simulated values; dashed line: Expected values without diffusion suppression.

of the extended theory. The more general case of non-linear gradients and spherical sample shapes, which can not be solved analytically, was simulated using computer calculations.

Although the suppression of the SE is a considerable effect, it was not reported in literature yet for different reasons. First, SEs in gases can conveniently only be studied by using polarization enhancement techniques, as the signal from thermally polarized samples is much too weak (see Appendix A). Second, the SE maximum shift can only be recognized easily in ^{3}He, while in ^{129}Xe it is usually overlooked, as it amounts only to a few percent offset from the expected maximum position. Third, most experiments with HP gases, especially with ^{3}He, are conducted using small flip angles and short timings, which circumvents the observation of this effect. Further investigations of this effect also require an accurate gas mixing system to vary diffusion coefficients in a large range with high accuracy and reproducibility.

The understanding of this strong, time-dependent diffusion suppression effect opens the way to different new applications, like e.g. SE sequences in MRI of HP gases or the measurement of intermolecular double quantum coherences in gases, as shown in the following chapter. The effect may also be used as an alternative method for diffusion measurements in linear gradients within one scan only, by fitting the analytical calculations to the detected signal.

Chapter 5

Intermolecular multiple-quantum coherences in gases

5.1 Diffusion effects on iMQCs

Since the first measurements of intermolecular multiple-quantum coherences (iMQCs) in liquids in the early 90's [He 93, Warren 93], which arise from the distant dipolar field (DDF) created by the spins, great progress has been made in understanding the physical basis and the characteristics of iMQCs [Lee 96, Jeener 00]. The effects have been explored for biomedical spectroscopic or imaging purposes, resulting in several novel applications [Warren 98, Zhong 04]. But still, both the theoretical basis and issues related to the practical implementation are objects of current research. Numerous efforts have been published, concerning the effect of diffusion on the iMQCs [Barros Jr. 06, Ardelean 00, Chen 01b]. Diffusion coefficients in liquids are small and cannot be easily varied. Therefore, studying iMQCs in gases is interesting, because the diffusivity is much higher and can be changed over several orders of magnitude. Nevertheless, to detect iMQCs in gases, different obstacles have to be overcome.

The first problem arises from the low spin density in gases. The effect of iMQCs requires a strong DDF, which is built up by the aligned spins. In the case of thermal polarization, the DDF is much too small for measurable

effects. By using HP noble gases, like ^{3}He or ^{129}Xe, the magnetization can be increased by several orders of magnitude, leading to a strong DDF, which is independent of the static magnetic field.

Second, the diffusion in gases is about 5 orders of magnitude higher than in liquids, which involves a strong suppression of the NMR signal (see Chapter 4), but also increases the zone where the short range dipolar couplings between individual spins is averaged out. This problem can be addressed by lowering the diffusion by admixing the spin-bearing gas with a heavier buffer gas. Thereby, the diffusion coefficient can be varied over a range of 0.1 to 10 cm^2/s. With these two major obstacles under control, iMQCs in gases can be studied.

5.2 iDQCs in H_2O

First of all, simple experiments in water were conducted to show the general capability of our setup to detect iDQCs due to DDF effects. By comparing the results with those from literature, the reliability of our setup was validated prior to the detection of new effects in HP ^{3}He.

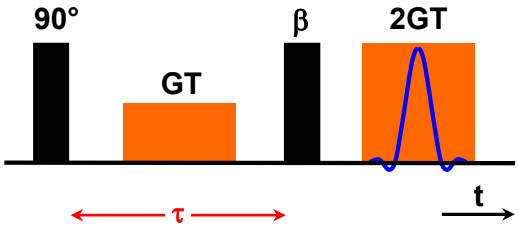

Figure 5.1: CRAZED sequence with signal acquisition inside of second gradient to check correct gradient ratio to select iDQCs.

Therefore, a simple CRAZED experiment was set up to check the correct ratio of gradients to select only iDQCs (see Fig. 5.1). The following experimental parameters were used for all measurements in water: Gradient time $T = 2$ ms, gradient amplitude $G = 42$ mT/m for first pulse, $2G = 84$ mT/m for the second one, r.f. pulse delay time $\tau = 2.5$ ms, duration of 90° pulse 12.5 μs, number of acquired points 2048, dwell time 100 μs and a repetition time of 1 s. The water was doped with copper sulfate to shorten the relaxation times to allow a fast repetition rate ($T_1 = 61$ ms, $T_2 = 52$ ms). The

NMR signal was acquired using a birdcage coil with an inner diameter (ID) of 22 mm and a spherical sample container (ID 12 mm) at a magnetic field of 4.7 T.

In order to insure that the signal after the second gradient pulse arises only from iDQCs and not from a "leakage" of the SQ echo, first the signal inside of the gradient pulse was checked. If the ratio of the two gradient pulses is correct, the SQ echo will be refocused in the center of the second gradient and no signal will remain at the end of the gradient.

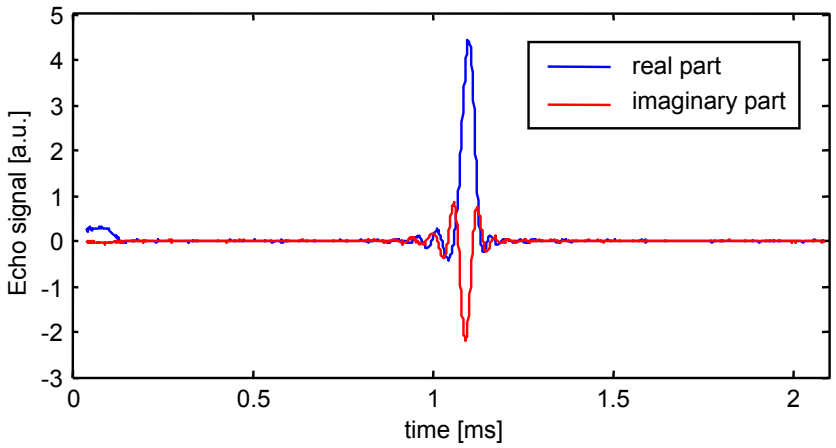

Figure 5.2: Quadrature detected single quantum signal inside of the second gradient measured in H_2O (ratio of gradients 1:2). The echo is refocused in the center of second gradient.

The experimental results in Fig. 5.2 show that this is indeed the case, as the SQ signal builds up exactly at the center of the second gradient pulse without any signal left at the end of the gradient. If one chooses equal amplitudes for both gradient pulses, the SQ signal is completely refocused at the end of the second gradient (see Fig. 5.3). Hence, the proper functioning of the double quantum (DQ) filter was shown with our setup.

Then, the time domain signal directly after the DQ filter was acquired. While Fig. 5.4 shows the real and imaginary part of the signal, the absolute value is shown in Fig. 5.5. The signal is strong, with a high signal-to-noise ratio (SNR). The typical behaviour of an iDQC signal, of building up from zero, is clearly visible. Due to the temporal field distortions and the eddy currents in the surrounding metal, created by the rapid ramp down

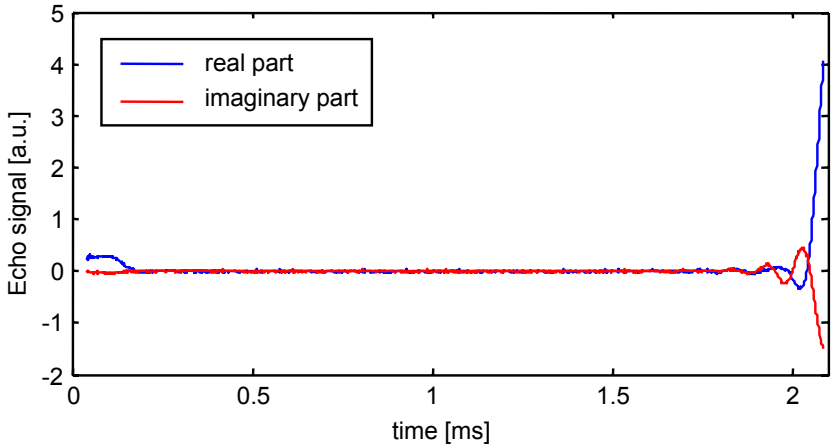

Figure 5.3: Quadrature detected single quantum signal inside of second gradient for water (ratio of gradients is 1:1). Signal is refocused at the end of second gradient.

of the gradient, no signal can be detected within the first few ms after the gradient pulse. The signal is suppressed by T_2^* relaxation before it can reach its theoretical maximum at $2.2\,\tau_d \approx 440$ ms, as $T_2^* \approx 10$ ms, in this case.

The whole time evolution of the signal without T_2^* relaxation can be measured with an experiment described in [Marques 05] (see Fig. 5.6), which allows the simultaneous determination of the diffusion coefficient D and the relaxation time T_2 [Barros Jr. 06]. The used pulse sequence minimizes all effects that contribute to the signal attenuation of the iMQC echo, which thus tend to mask the effect of the DDF. Besides T_2^* relaxation, diffusion, field inhomogeneity and radiation damping have also to be taken into account, which is accomplished by the modified CRAZED sequence in Fig. 5.6.

The effects of field inhomogeneity were minimized by inserting a 180° RF pulse in the t_1 period, thus ensuring that the transverse magnetization is refocused at the time of application of the second 90° RF pulse. A 180° RF pulse was also applied approximately half-way through the t_2 period to refocus signal dephasing, due to field inhomogeneity, and thus eliminate T_2^* decay. The final 180° RF pulse is usually a soft pulse, which selects only a slice of spins that form the signal. By this means, the magnetic-field gradient which is sensed by the contributing spins is further reduced. In our experiment, a hard 180° RF pulse without slice selection was used, as only

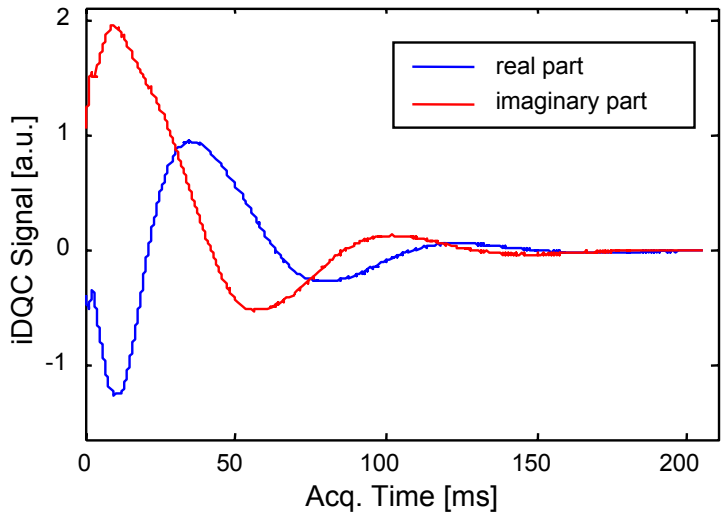

Figure 5.4: Quadrature detected iDQC signal acquired in water with a CRAZED experiment.

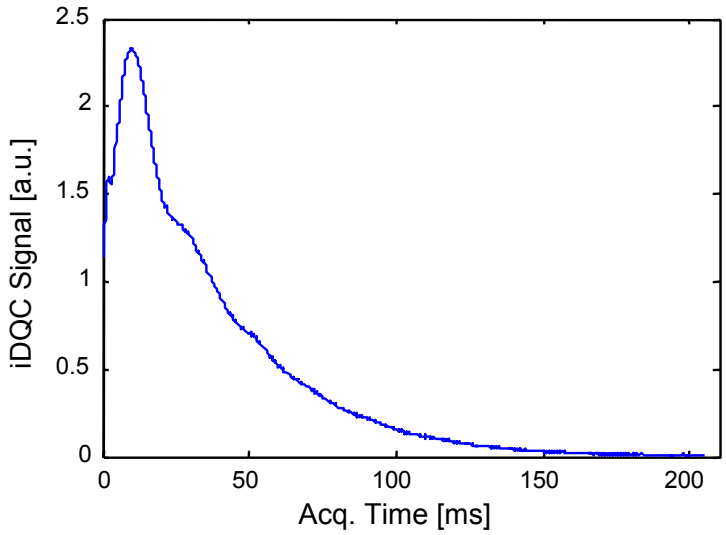

Figure 5.5: Magnitude of the iDQC signal acquired in water with a CRAZED experiment.

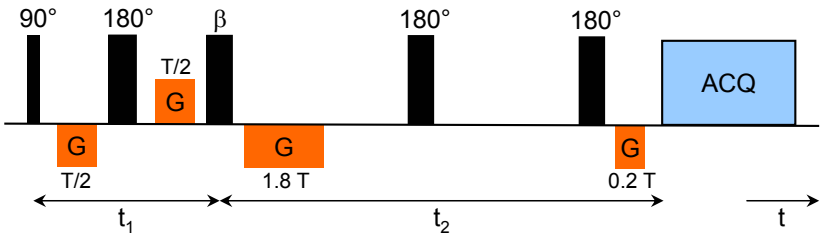

Figure 5.6: Modified CRAZED sequence to acquire the full time evolution of the iDQC echo without signal reduction by radiation damping and magnetic-field inhomogeneity.

the general capability of our setup to record the full time evolution of the iDQC signal should be demonstrated.

Radiation damping occurs as a result of currents induced in the RF coil by significant amounts of precessing magnetization. It was avoided during the t_2 period by ensuring that the transverse magnetization remained dephased during this time. Therefore, the second gradient pulse was split into two parts: The first one, with an area of $1.8GT$, is applied directly after the pulse with flip angle β; the second one, with an area of $0.2GT$, is applied just before the signal acquisition.

The experiment was conducted with a repetition time of 15 s, a signal acquisition time of 0.82 s per t_2 step, t_1 = 5 ms and a gradient time of T = 2 ms. The value of t_2 was incremented between the experiments, using 30 ms steps. The one-dimensional time evolution was calculated by Fourier transforming the acquired signal at each value of t_2 and using the integral over the spectral peak in the magnitude spectrum. Further information can be found in [Marques 05]. Fig. 5.7 shows the measured time evolution of the iDQC signal in water, measured at a magnetic field of 4.7 T. The theoretically expected maximum value at 2.2τ is marked by the dashed line. The experimental maximum almost reaches this value, the small deviation arises from the diffusion of water molecules, the missing slice selection or the unconsidered T_2 relaxation.

In order to verify that the detected signal arises from an iDQC, the signal dependence on the flip angle β of the second pulse was measured. As it was shown from theory in Section 2.5.5, the maximum iDQC signal is expected at $\beta = 120°$. Fig. 5.8 depicts the intensity of the measured iDQC signal

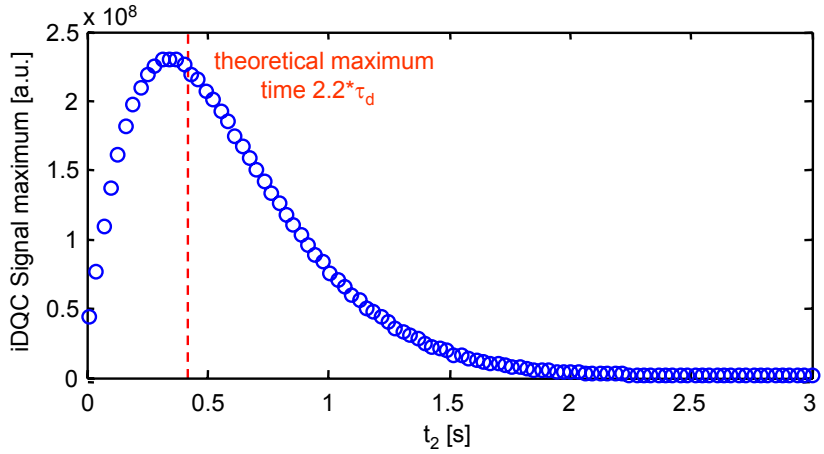

Figure 5.7: Time evolution of the iDQC signal in water at a magnetic field of 4.7 T. The theoretically expected maximum position is marked by the dashed red line.

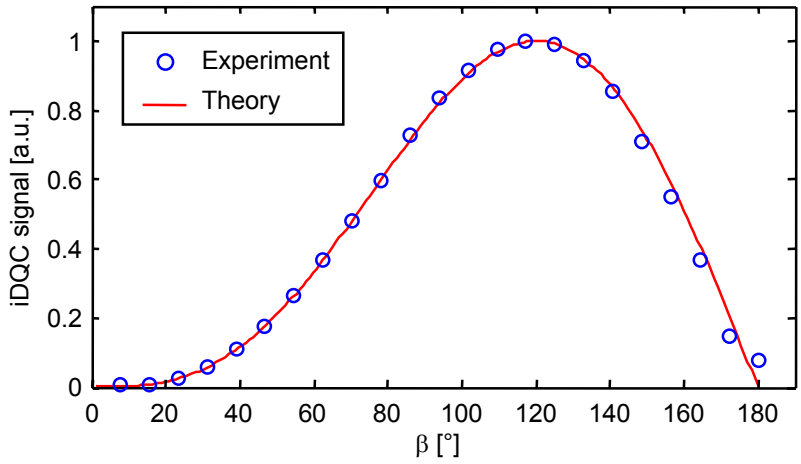

Figure 5.8: Signal intensity of the iDQC signals as a function of the flip angle β measured in water at 200 MHz. The red line shows the theoretical curve, calculated by Eq. 2.103, with a predicted maximum at $\beta = 120°$.

depending on β, in comparison to the theoretical curve given by Eq. 2.103. The characteristics of the curve show perfect agreement with the theoretical values, with the maximum at $\beta = 120°$. Hereby, the capability of the used setup to excite and detect iDQC signals, also in their full time evolution, was shown, making the following experiments in the gas phase reliable.

5.3 iDQCs in HP ^{3}He

As it was shown in Chapter 4, the fast spin motion in gases strongly affects the signal of echo experiments. Therefore, suppressing diffusion by gas admixing is the key for the detection of echo signals in gases, especially for long echo times. Calculations, using the theory in Section 2.5, show that the iDQC signal in HP ^{3}He gas with a pressure of 1 bar and a polarization of 60% reaches its maximum at a time of about 53 ms after the second r.f. pulse. This signal is additionally suppressed by T_2^* relaxation, due to magnetic field inhomogeneities with a time constant of 14 ms for the present conditions. As the estimated motional correlation time for a mixture of 1 bar ^{3}He and 2 bar SF_6 is already above this value (about 20 ms, see Section 4.4.4), it should be possible to suppress the effect of diffusion well enough to detect the rising slope of the iDQC signal. Therefore, in the following experiments, the diffusion coefficient was reduced as much as possible by increasing the total pressure of the gas mix to 7 bar by admixing SF_6 as a buffer gas.

First of all, a nutation spectrum was acquired to calibrate the flip angle dependence on the r.f. pulse length. Hereby, the approach described in Section 3.6 was used, resulting in a duration of 29 μs for a 90° pulse. Before conducting the iDQC measurement in ^{3}He, a CRAZED experiment with detection of the SQ signal inside of the second gradient was accomplished to optimize the parameters and to check the experimental setup. The measurements were conducted parallel to the experiments in H_2O, described in Section 5.2 (pulse sequence depicted in Fig. 5.1). The gradient ratio was chosen in a manner, that the SQ signal is refocused exactly in the middle of the second gradient. In order to minimize the loss of signal by diffusion suppression during the gradient pulses, the timings were chosen as short as possible, in this case a duration of $T = 300$ μs. For such short durations, the impedance of the gradient coils delays the buildup of the currents. This

leads to a deviation between the adjusted gradient parameters and real gradient amplitudes. Hence, instead of the expected 1:2 ratio of the gradients, the second gradient had to be set about five times larger than the first one to center the SQ signal. Additionally, a four-step phase cycling was implemented to suppress the remaining SQ signals while adding up the iDQC echo. The first r.f. pulse is cycled (x, y, -x, -y), the receiver (x, -x, x, -x), while all other pulse phases were left unchanged. As the measurements in Fig. 5.9 show, under these conditions the SQ signal is refocused at the middle of the gradient pulse and the individual phase cycling steps exactly sum up to zero. Also within one single phase step, no SQ signal is left at the end of the

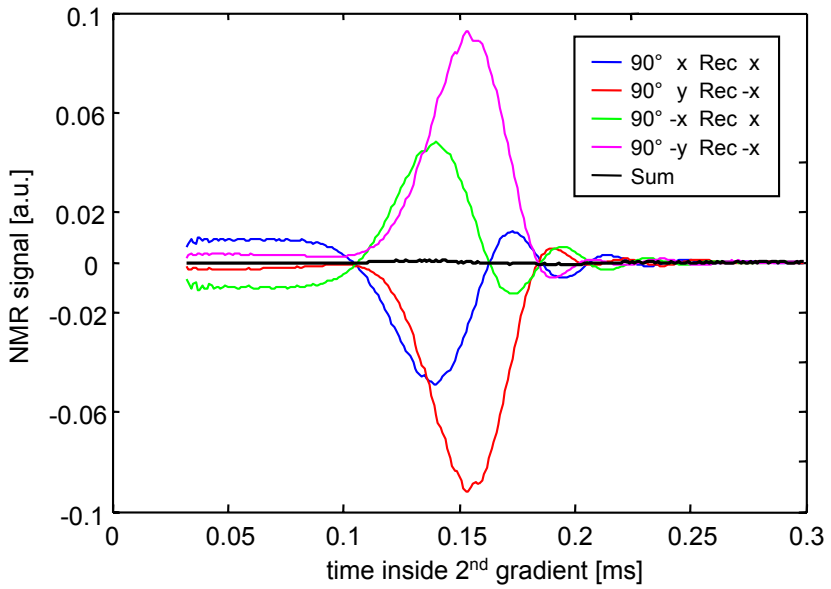

Figure 5.9: SQ signal acquired inside the second gradient of a CRAZED sequence in HP ^{3}He. Different colors show the single phase cycling steps; the sum is plotted in black.

gradient. Note that each phase cycling step is a separate experiment with a new gas mixture. The procedure of evacuating, gas mixing and acquisition of the signal takes about one minute per phase cycling step. The four different phase steps are measured consecutively and can be controlled automatically by the spectrometer PC; they are added up later during data processing. By this approach, it was assured that no SQ signal is passing the DQ filter of the sequence.

In exactly the same manner, the signal was acquired directly after the second gradient. The four different phase steps and the resulting sum are presented in Fig. 5.10. While Fig. 5.10 A shows the real parts of the quadrature detected signals, Fig. 5.10 B presents the magnitude values. The detected signal builds up from zero, while the remaining SQ signal is averaged out almost completely by the phase cycle. The signal amplitude clearly exceeds the noise level of the measurement.

For this first experiment series, the gas mixing was accomplished by manually switching the valves and the phase cycling by starting each measurement individually with the respective phases. The accuracy of the measurements could be clearly improved in a second series, using the automated gas mixing system and the possibility of acquiring one whole phase cycle as one experiment. The reproducibility of the obtained gas mix is much higher and the measurements are not anymore prone to operational errors of the experimenter. The following steps were now subsequently automatically conducted by the experiment program for each phase cycling step:

1. Gas mixing procedure to fill the sample container with 1 bar HP ^{3}He and 6 bar SF_6 as described in Section 3.5.

2. Diffusion measurement by a PGSE sequence using small flip angles to check if the gas mixing operated correctly.

3. Obtaining a FID signal with a small flip angle as a measure for the relative polarization of the HP ^{3}He to normalize the iDQC signal.

4. CRAZED sequence to detect the iDQC signal.

5. Obtaining a FID signal with a small flip angle as a measure for the leftover relative polarization of the HP ^{3}He to normalize the following measurement.

6. CRAZED sequence with acquisition inside of the second gradient to check that the gradient ratios are set correctly, and the phase cycling works properly.

The whole setup was calibrated and tested thoroughly to get reproducible results from different sample fillings, to ensure that the automatic averaging procedure works reliably.

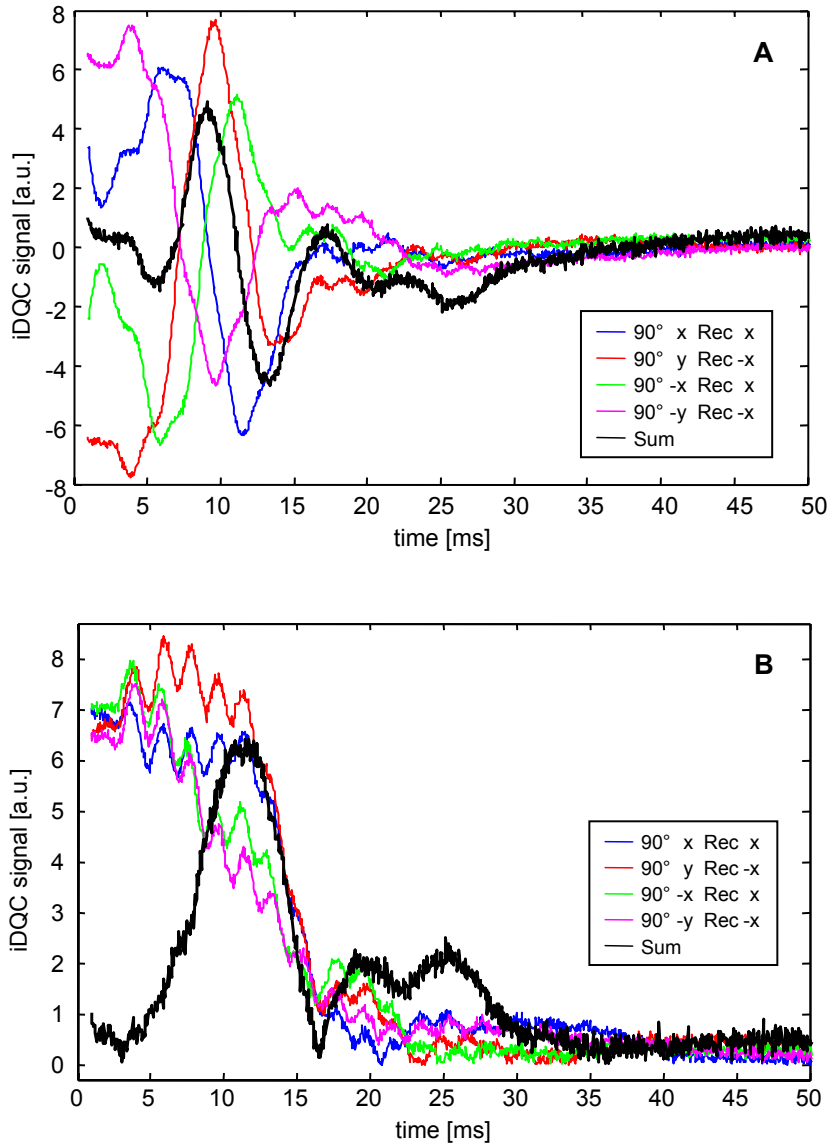

Figure 5.10: First iDQC signal in gases, measured with manual gas mixing and phase cycling in a mixture of 2 bar HP ^{3}He and 5 bar SF_6. Different colors show the separate phase cycling steps; the sum is plotted in black. **A:** Quadrature detected real parts of signal; **B:** Magnitude of signals.

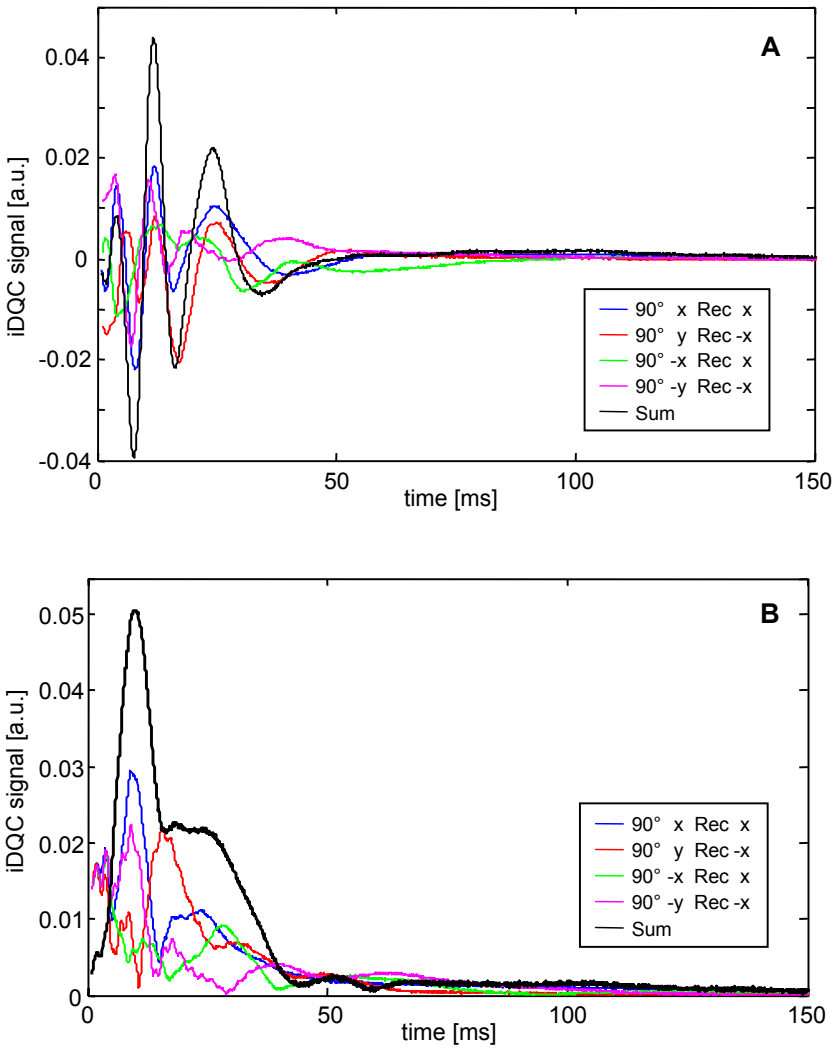

Figure 5.11: Improved iDQC signal in HP ^{3}He gas, measured with automated gas mixing and phase cycling within a mixture of 2 bar HP ^{3}He and 5 bar SF_6. Different colors show the separate phase cycling steps; the sum is plotted in black. **A:** Quadrature detected real parts of signal; **B:** Magnitude of signals.

Additionally to the automation of the experiment, the gradient amplitudes were lowered by a factor of 2/3 to have less signal suppression due to diffusion. This changes led to a much higher SNR, as the signals depicted in Fig. 5.11 show. The amplitude of the iDQC signal even exceeds the remaining SQ signal in a single scan. This residual SQ signal was averaged out by the phase cycle, showing the theoretically expected buildup curve of the iDQC echo. The signal reaches its absolute maximum at a time of about 10 ms after the gradient pulse. The theoretical maximum time for a polarization of 60% and a pressure of 2 bar ^{3}He without considering T_2^* relaxation is calculated to be 27 ms (see theory in Section 2.5.4). Taking T_2^* relaxation into account and the fact that the maximum of the integrated signal intensity occurs at ca. 20 ms, the experimental value agrees well with the theoretically predicted one. Further experiments showed that the signal is reproducible in terms of shape and amplitude.

One more series of experiments was accomplished to verify the authenticity of the iDQC signal in HP ^{3}He gas. Therefore, the iDQC signal was measured in dependence of the flip angle β of the second r.f. pulse. As it was shown from theory in Section 2.5 and from the experiments in H_2O (see Fig. 5.8), the amplitude of the signal maximizes for $\beta = 120°$. Therefore, a whole set of CRAZED experiments in ^{3}He with varying β was conducted; the results are presented in Fig. 5.12. For these series, a gas mix containing 1 bar ^{3}He and 6 bar SF_6 was used to get enough comparable gas fillings from one transport cell of ^{3}He. Using this mix, 69 fillings of the sample volume with 1 bar ^{3}He could be provided. The strongest amplitudes clearly arose for $\beta = 120°$ and 130°. In order to check this in more detail, the measured signals for each β were Fourier transformed and the integral over the peak was plotted versus the flip angle β in Fig. 5.13. Additionally, the theoretically expected curve was calculated by Eq. 2.103. The experimental values follow the theoretical curve quite well. The deviations can be traced back to B_1 field inhomogeneities, which are leading to errors in the flip angle distribution and as well to statistical errors. Also, the assumption for the theoretical curve of $\xi = \mu_0 \gamma M_0 t_2 \sin\beta \ll 1$ (Eq. 2.101) is not strictly valid anymore due to the high magnetizations of ^{3}He used in our experiments. The exact formula in Eq. 2.104 results in a curve, which comes closer to values for small β, but features a larger difference at the values of bigger β. Therefore, it is not

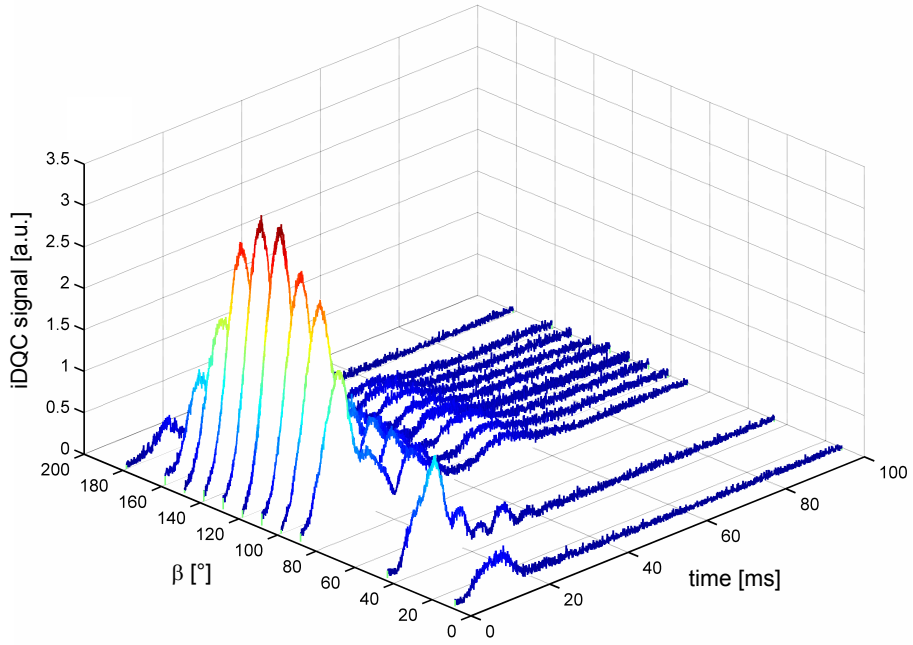

Figure 5.12: Different iDQC signals in ^{3}He for varying flip angles β of the second pulse in the CRAZED sequence.

shown here.

Most importantly, it was clearly shown, that the signal vanishes for $\beta = 180°$. If the detected signal was related to remaining SQ coherences, it would reach its maximum value at 180°. Therefore, these measurement represent, as far as we know, the first experimental evidence of iDQCs in the gas phase, arising from the DDF in HP ^{3}He.

In order to check the influence of diffusion on the iDQC echo, three experiments were conducted with different gas mixtures. While for all experiments the same amount of 1 bar ^{3}He was used, different portions of SF_6 with a pressure of 6, 3 and 1 bar were added, leading to diffusion coefficients of $D = 0.09$, 0.21 and 0.95 cm^2/s. All measurements were accomplished with a flip angle of $\beta = 120°$. As shown in Fig. 5.14, the signal is clearly reduced with rising D, as it was predicted by the measurements of the pseudo SEs in Chapter 4. The signal suppression by diffusion also leads to a shift of the detected signal maximum, to shorter times with increasing D. But still the echo signal is detectable for the highest diffusion coefficient, even though

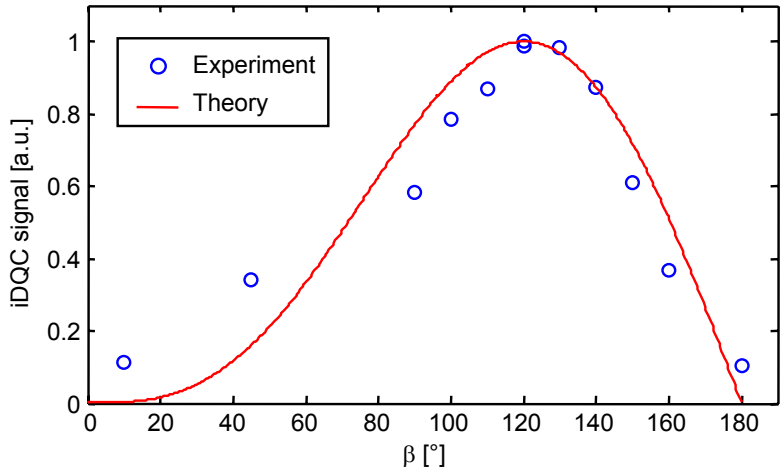

Figure 5.13: Comparison of the measured iDQC signal maxima depending on the flip angle β of second the pulse and the theoretical curve calculated from Eq. 2.103.

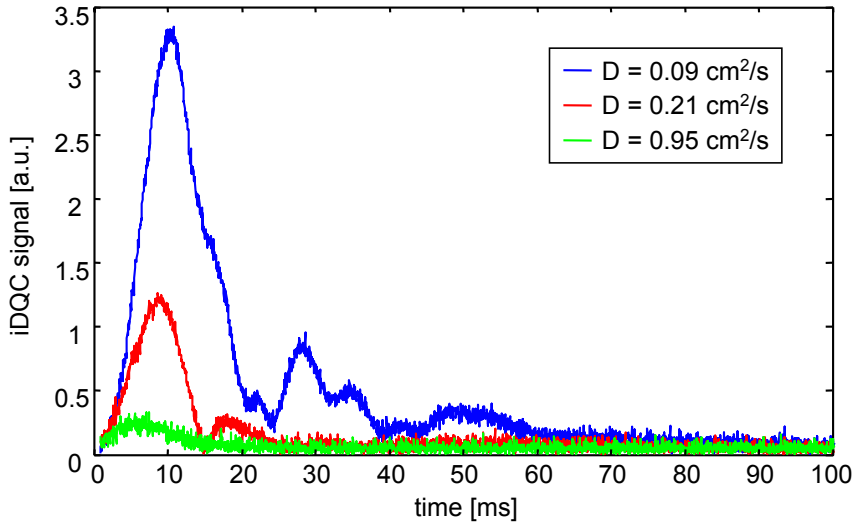

Figure 5.14: iDQC signals measured with a CRAZED pulse sequence in HP ^{3}He for different diffusion coefficients. The flip angle $\beta = 120°$ for all experiments.

with a poor SNR. Here, D is only half the value of diffusion in pure ^{3}He at ambient pressure. If the SNR is enhanced by further developments of the experiment technique, future experiments in pure ^{3}He without gas mixing will be feasible. Possible improvements could be accomplished e.g. by shorter and stronger gradient pulses, which would lead to a smaller diffusion suppression of the signal (see Eq. 2.69) or by larger sample volumes to increase the amount of magnetization.

5.4 Conclusions

For the first time, iDQCs in the gas phase were detected, which arise from the DDF formed by the ^{3}He spins. On the one hand, this allows detailed studies of the underlying effect in principle. Especially the influence of the polarization and the diffusion on iDQC signals can be well examined, because these parameters can be easily changed in HP gases. The acquisition of the whole time evolution of the signal without T_2^* relaxation will also reveal new insights.

On the other hand, this high sensitivity of the iDQCs to diffusion and spatial restrictions might open the way for different new applications. As it was already shown in liquids, iDQCs might be useful to evaluate properties of porous samples [Bouchard 04]. In comparison to liquids, HP gases would allow the investigation of larger structures over a bigger range of pore sizes, as the dipolar coupling distance exceeds the one in liquids and can be varied easily by changing the amount of polarization. Such studies might also be useful in medical MRI, e.g. in lung imaging.

Chapter 6

Solutions of HP ^{129}Xe

6.1 Enhancing NMR and MRI by solutions of HP ^{129}Xe

Hyperpolarized noble gases hold an enormous potential for enhancing the sensitivity and contrast of a variety of NMR and MRI experiments. As already shown in Section 2.4 ^{129}Xe, unlike ^{3}He, can be dissolved amongst others in different biologically compatible solvents and is therefore not only suitable for void space imaging, e.g. in lungs [Albert 94, Mugler III 97], but also as a vascular contrast agent in medical MRI [Goodson 97, Möller 99]. Conventional MRI contrast agents (e.g. Gd-DTPA or superparamagnetic iron particles) do (and must) not pass membranes in the body due to their large size [Brasch 83, Sorensen 97, Caravan 99], while xenon atoms are small enough to pass such barriers (e.g. the blood-brain barrier or blood-gas barrier in lung). Therefore, dissolved HP xenon is an interesting candidate for a new (free diffusive) MRI contrast agent [Goodson 99] or to enhance functional contrast in the brain.

Different methods are available to bring HP xenon into the blood stream for the usage as a MRI contrast agent. The easiest way is to dissolve it via inhalation over the lungs. This becomes quite problematic due to the depolarization caused by the presence of oxygen and the slow passage into the cardiovascular system. Hence, it is mainly demonstrated in small animals, as here the transport is much shorter in the range of a few seconds compared to tens of seconds in humans. Fig. 6.1 A shows an image of a rat brain acquired

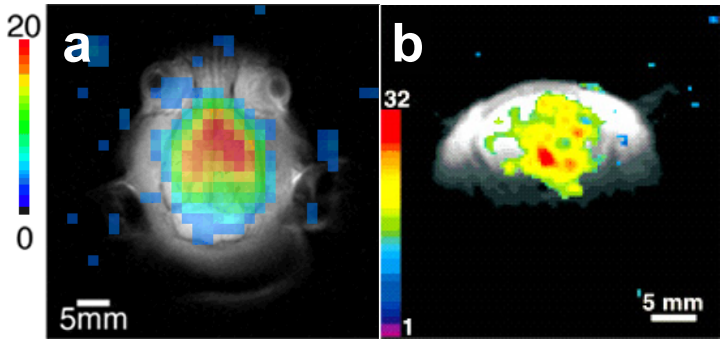

Figure 6.1: HP ^{129}Xe MR images of a rat brain. HP ^{129}Xe was supplied by different methods. **A:** By inhalation of pure xenon gas for 40 s [Swanson 97]. **B:** By injection of a xenon carrier liquid into the carotid artery [Duhamel 01].

after 40 s ventilation with HP xenon [Swanson 97]. The SNR is quite poor but it clearly verifies that brain imaging is possible with HP ^{129}Xe. A better SNR is obtained if the HP ^{129}Xe is predissolved in a carrier liquid which is then injected into the carotid artery of the rat [Duhamel 01]. In this case, HP ^{129}Xe reaches the brain much faster, around 1 s after the injection, with a much higher polarization (see Fig. 6.1 B). To dissolve xenon in the carrier liquid, HP xenon is typically accumulated by freezing it in liquid nitrogen, vaporized in the presence of the liquid afterwards and dissolved by vigorous shaking. This process is hard to control and certainly not suitable for later application in routine examinations in hospital.

NMR spectroscopy of dissolved ^{129}Xe has also gained considerable interest, where it serves as a zero-background probe for studying chemical properties and structures, such as guest-host interactions [Song 97], novel microporous systems [Soldatov 04], surfaces [Raftery 91] and most importantly biomolecules [Rubin 00, Landon 01, Lowery 05]. Most such studies are carried out in solutions, particularly in aqueous solutions. Also here, the dissolution process of HP ^{129}Xeis a major problem. The drawback of single-batch experiments is the limited time available for experiments, since the HP ^{129}Xe loses its polarization on the time scale of the longitudinal relaxation time T_1 (usually tens of seconds). Therefore, the depolarized xenon

should be continuously replaced with freshly polarized gas, which in analogy to surface NMR spectroscopy, could be realized by continuous-flow experiments [Haake 97, Brunner 98, Nossov 03]. Han et al. recently developed a system which enables HP ^{129}Xe to be dissolved under stopped flow [Han 05]. Microbubbles of HP xenon are injected into the solution via microcapillaries. During the NMR experiment, however, the flow is switched off in order to maintain the spectral resolution, which otherwise would be reduced by the large change in magnetic susceptibility at the gas/liquid interface even in the micro bubbles. Recent studies of the interaction between xenon and phospholipid bicelles explicitly report problems related to the dissolution of xenon via shaking and foam formation [Li 06]. Therefore, the sample preparation in such experiments is absolutely critical for success, in particular in the biochemical and biomedical areas.

6.2 Principle of membrane dissolution method

A new method was developed to dissolve HP ^{129}Xe, avoiding the problems of the established methods described in the previous section. Commercially available hollow fibre membranes were used (CELGARD® X50, Membrana GmbH, Wuppertal, Germany) for the gas transfer into the solvent of interest. These microporous fibers are thin-walled, opaque and made from polypropylene (PP) with a nominal internal diameter of 220 μm and an effective pore size of 0.04 μm. PP is a hydrophobic polymer, so the solvent does not pass the membrane walls. The single fibers are knit into a fabric array to have an evenly spacing, to maximize the active exchange area and to ease the practical handling of the membrane bundles (see Fig. 6.2). Usually these capillaries are used for blood oxygenation as artificial lungs ("oxygenators") in heart-lung machines during heart surgeries. Therefore, they are optimized for the gas transfer of oxygen into aqueous solutions. As most of the solvents of interest for biomedical ^{129}Xe NMR and MRI are aqueous solutions as well, the membranes should also simplify the xenon dissolution process.

The principle of our setup is shown in Fig. 6.3. A nonmagnetic pump circulates the solvent through the oxygenator module and a reservoir inside the NMR coil. The HP ^{129}Xe counter flows the liquid and dissolves through

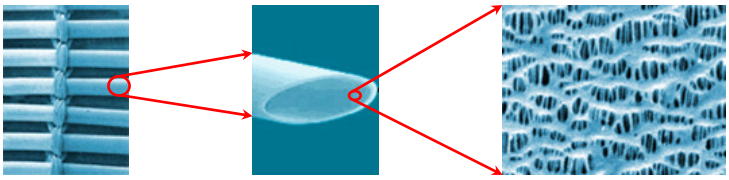

Figure 6.2: Structure of the CELGARD® microporous hollow fiber membranes used for xenon dissolution.

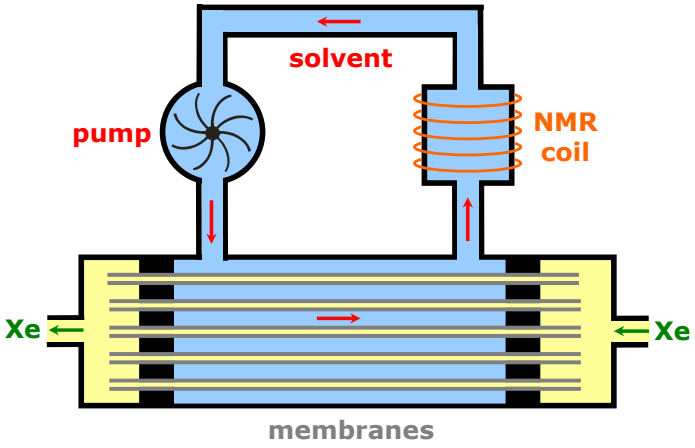

Figure 6.3: Principle of xenon dissolution process using hollow fiber membrane modules [Zänker 05].

the pores of the membranes. This process can be monitored by ^{129}Xe NMR spectroscopy in a NMR coil. By this method of gas dissolution a continuous flow of xenon into a liquid can be provided without any physical disturbance of the solvent system [Zänker 05].

A first simple setup was built (see Fig. 6.4) to investigate the abilities of this approach and to check if the polarization of HP ^{129}Xe maintains while penetrating through the very small pores of the membrane walls. Instead of a pump, two syringes were used to move the solvent manually back and forth through the oxygenator module. The gas side of the module was connected directly to the polarizer outlet, which provided a continuous flow of a gas mix with 1% of xenon at a flow rate of ca. 250 ml/min. The pressure of the

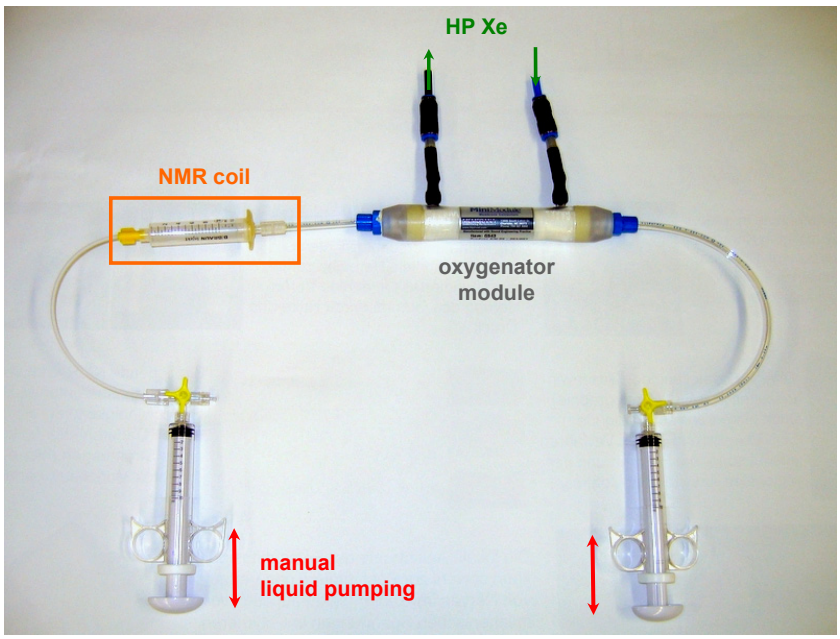

Figure 6.4: First setup to investigate xenon dissolution process through porous membranes. The solvent is driven manually by two syringes through the oxygenator module into a reservoir inside the NMR coil, where the dissolved HP ^{129}Xe is detected.

gas stream was reduced by a teflon needle valve from 7 to about 1.5 bar. As the membranes were originally designed for applications with blood, the first experiments were conducted with human blood as a solvent, stabilized with heparin against coagulation. The liquid volume was carefully filled completely, paying special attention to remove all remaining air bubbles. The gas volume was evacuated shortly for a few seconds only, to avoid a damage of the membranes. Then it was flushed with nitrogen to remove all residual oxygen, which would destroy the polarization of ^{129}Xe.

Fig. 6.5 shows the ^{129}Xe NMR spectra, acquired of the syringe reservoir during the pumping process. In whole blood within 128 scans two resonance lines are detected, which are due to ^{129}Xe dissolved in blood plasma (196 ppm) and bound to blood cells (222 ppm). The spectrum in blood plasma only was recorded within 32 scans and features only one line with a much higher SNR. The plasma was obtained from the whole blood by removing the cells with centrifugation. The lower SNR of the whole blood is due to

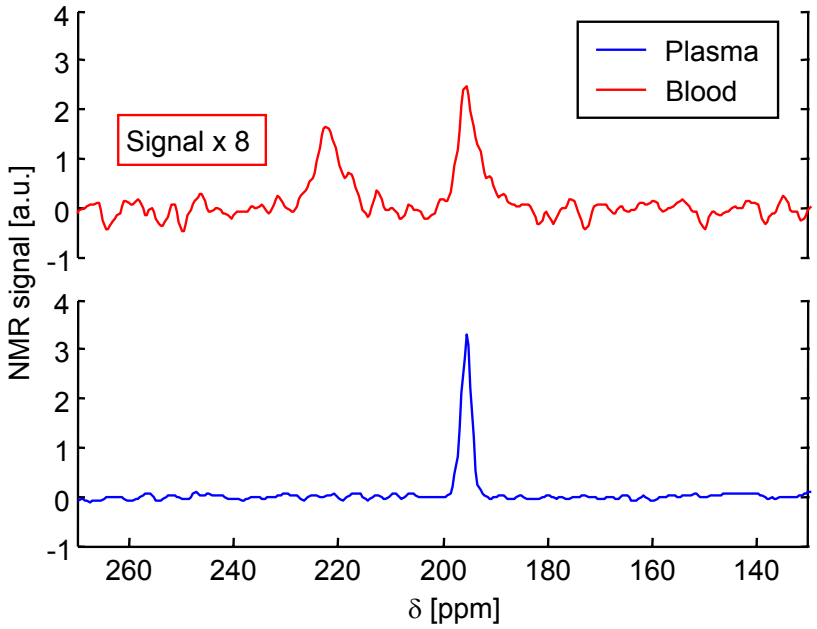

Figure 6.5: First ^{129}Xe NMR spectra acquired using the membrane dissolution method. **Top:** Signal in whole blood within 128 scans; **Bottom:** Signal in blood plasma within 32 scans;

the shorter T_1 relaxation time of about 3 s in there, compared to a $T_1 \approx$ 14 s in blood plasma [Wolber 99]. This difference results from the strong relaxivity of deoxyhaemoglobin on ^{129}Xe in venous blood. Some cells in the whole blood might also block the membrane pores, hampering the gas dissolution efficiency. The chemical shifts of the spectra are referenced on the ^{129}Xe gas resonance at 0 ppm measured in a calibration experiment in advance. As there is no other possibility for HP ^{129}Xe to reach the sample volume besides the passage through the membranes, it is proved that the new method of xenon dissolution is working properly without destroying the non-thermal magnetization completely. No signal is detected at the gas resonance frequency, which shows that no gas bubbles pass the membrane or form afterwards and that the gas is directly dissolved into the blood. The shift values of the detected peaks agree nicely with the ones reported in [Bifone 96].

For further evaluation of different HP ^{129}Xe carrier liquids, a more sophisticated setup was developed (see Fig. 6.6). The syringes for manually

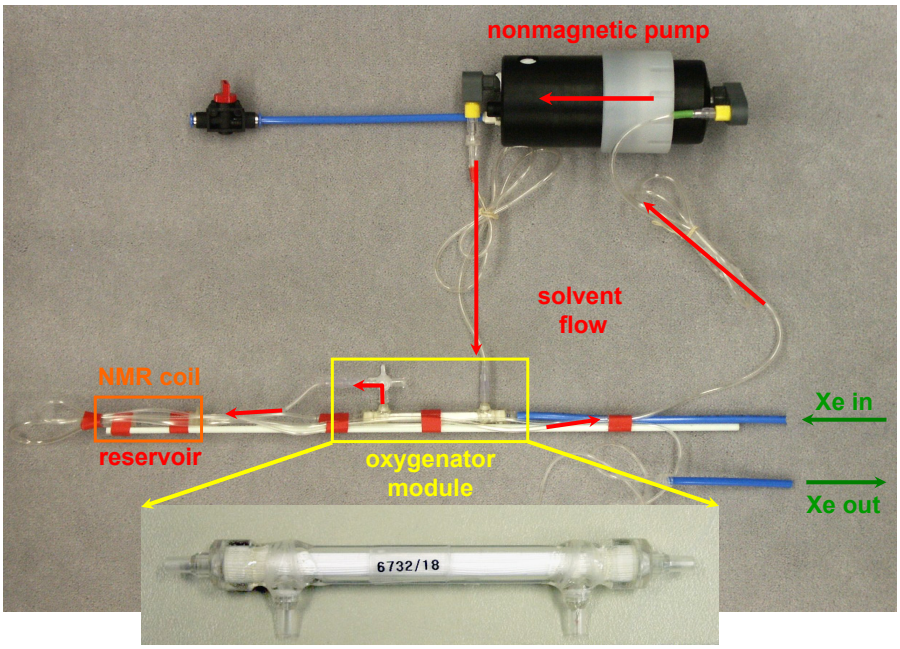

Figure 6.6: Improved setup for evaluation of different carrier liquids. The solvent is cycled by a completely nonmagnetic diaphragm pump through a specially designed mini-membrane module (enlarged). An additional gas tube (connected to the outlet of the membrane module) for referencing is also put into the NMR coil.

pumping were exchanged by a pneumatic non-magnetic diaphragm pump (AD 6 series, ALMATEC GmbH, Kamp-Lintfort, Germany), which features no moving metal parts that would lead to eddy currents. This setup allows a continuously flow of the solvent. The flow rate is controlled by the pressure of the compressed air, which drives the pump. The oxygenator module and the reservoir were assembled in a space-saving manner onto a fiber glass rod to fit the whole setup into the bore of a standard vertical NMR spectrometer and to ease the handling of the system. Thus, the carrier liquid does not leave the homogeneous magnetic field, which results in longer T_1 relaxation times. A gas tube connected to the outlet of the oxygenator module was also put into the NMR coil, in addition to the reservoir. Its gas signal was used for chemical shift referencing and normalization of the obtained ^{129}Xe spectra on the present ^{129}Xe polarization.

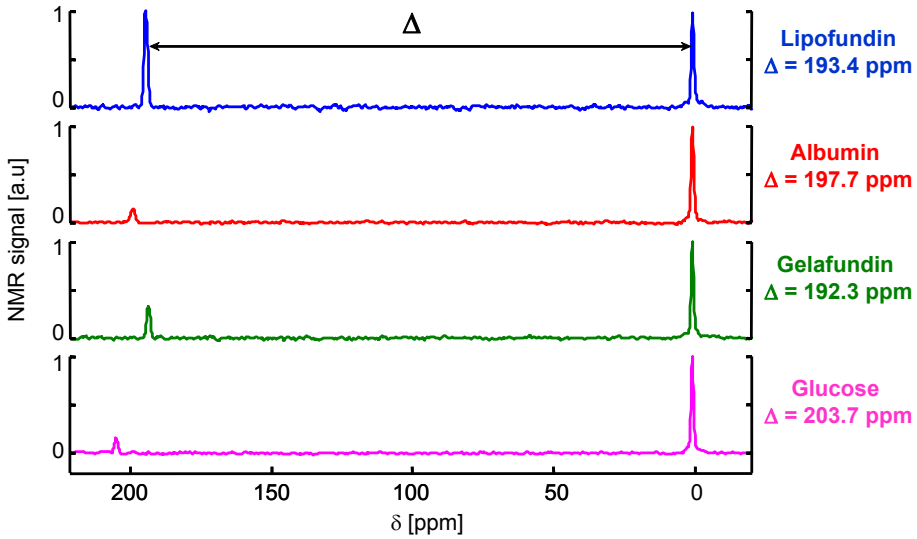

Figure 6.7: ^{129}Xe spectra of different xenon carrier liquids. All spectra are referenced and normalized to the gas peak at 0 ppm. Each spectrum is collected within 128 scans and an experiment time of 64 s.

Four different potential carrier liquids were compared in a series of experiments. The obtained spectra are shown in Fig. 6.7. The best SNR is achieved in Lipofundin® 20% N (B. Braun Melsungen AG, Melsungen, Germany), an aqueous suspension of lipid vesicles known to be well tolerated biologically. In fact these emulsions, also named as Intralipid in other countries, are used clinically as nutrient supplements in hospitals. They are one of the most promising candidate for HP ^{129}Xe carrying contrast agents and were already used in several studies [Goodson 99, Möller 99, Duhamel 01]. The other solvents were: a human albumin solution (*Humanalbumin® 20%*, Biotest Pharma GmbH, Dreieich, Germany), a saline/gelatin solution, which is usually used as blood plasma expander (*Gelafundin® 4%*, B. Braun Melsungen AG, Melsungen, Germany), and a saturated glucose solution. The signal amplitudes of the different measurements were normalized to the gas peak at 0 ppm. The signal of dissolved ^{129}Xe is detected in all liquids, showing that the membrane method is working for different types of aqueous solutions. The strongest signal is detected in Lipofundin because xenon is

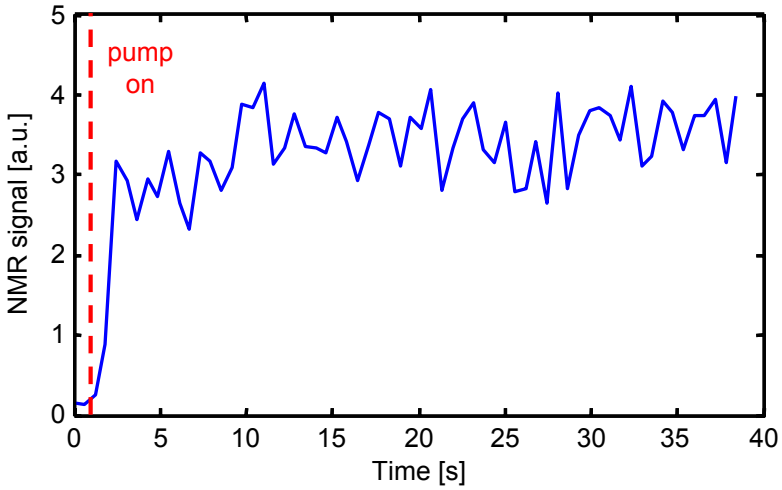

Figure 6.8: Development of dissolved ^{129}Xe signal amplitude in Lipofundin when dissolution process is started. The turn on time of the pump is marked by the red line.

lipophlic and Lipofundin has the highest fat content of the compared solutions. The chemical shift values vary for the different spectra as the large electron cloud of xenon is easily influenced by its surrounding molecules (see Section 2.4). The lowest chemical shift is measured in Gelafundin (192.3 ppm), which comes very close to the chemical shift of ^{129}Xe in pure water (192 ppm), as this solvents features the highest water content. The highest chemical shift is detected in glucose solution (203.7 ppm). This is due to the influence of the electronic-steric system of the molecular ring structure in glucose on the xenon electrons when xenon approaches the vicinity of the glucose molecule.

The time scale of the dissolution process was checked by a time dependent measurement of the dissolved ^{129}Xe signal in Lipofundin. Fig. 6.8 shows the development of this signal when the cycling of the liquid is started. The signal appears already 2 s after activating the pump. This value corresponds approximately to the time the liquid needs for flowing from the oxygenator module into the NMR coil. The signal stabilizes after 10 s at a certain level. We can conclude that the dissolution process occurs very fast on a time scale of less than a second. The small rise in signal amplitude at 10 s may be due to solvent, which is circled through the module at least twice, therefore

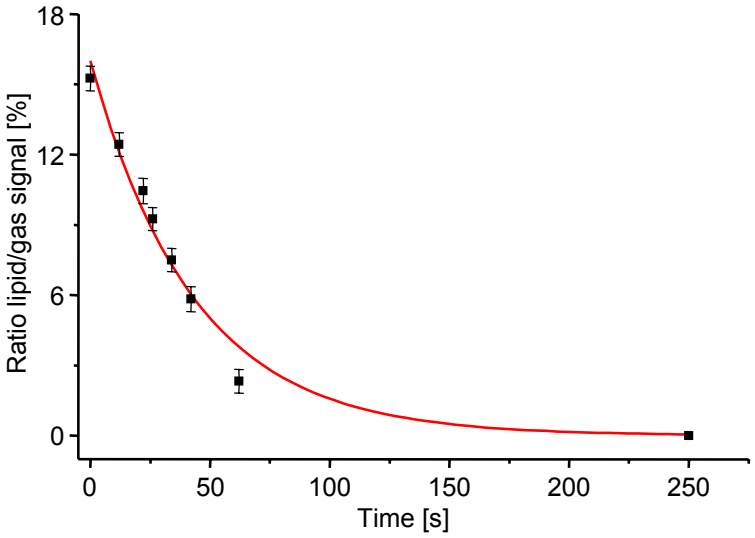

Figure 6.9: Relaxation of ^{129}Xe magnetization in Lipofundin at a field of 4.67 T. The signal is normalized on the signal of an additional gas tube inside of the coil. The red line shows the exponential fit of the data. These measurements were conducted at the RWTH Aachen in cooperation with S. Appelt and K. Münnemann.

taking up a larger amount of polarized ^{129}Xe. Additional, more accurate studies of the dissolution process dynamics, using the membrane method, are presented in Section 6.5.

Another important property to quantify is the T_1 relaxation time of HP ^{129}Xe in Lipofundin in this setup, as this might limit the usage as a contrast agent in clinical applications. To measure T_1 relaxation, the same procedure was accomplished as in the previous experiments. The liquid was cycled through the membrane module for a time long enough to be saturated with HP ^{129}Xe (ca. 20 s). Then the pump was stopped, and after a certain time the NMR spectrum was detected. Fig. 6.9 shows the dependence of the ratio, between the dissolved signal and the gas signal of the reference gas tube in the coil, on the waiting time after the switch-off of the pump. As there is no signal detected anymore after 250 s the ratio was set to zero for this time. An exponential fit of the measured points gives a value for $T_1 = (43 \pm 2)$ s which is in good agreement with the values obtained by [Bifone 96, Goodson 99]. This time is sufficient for the preparation, injection

and delivery of the contrast to point of interest. This makes Lipofundin a good candidate as a carrier liquid for HP ^{129}Xe in clinical applications, with limitations due to possible fat embolism at too high local concentrations (usual clinical limitation maximum 0.75 ml/kg·h).

6.3 Solubility quantification by partial pressure analysis

NMR measurements of HP ^{129}Xe to quantify the gas dissolution efficiency of different methods are not really reliable. In HP ^{129}Xe experiments, the NMR signal amplitude is determined mainly by the amount of dissolved gas and the polarization of ^{129}Xe. The polarization can fluctuate up to a few percent, depending on different not time-stable polarizer-settings, like cell temperature, flow rate, amount of alkali metal, etc. [Mühlbauer 07]. Different dissolution techniques might also influence the polarization in different ways, resulting in wrong dissolution efficiencies. Therefore, the xenon concentration was determined by a simple partial pressure measurement.

The setup is shown in Fig. 6.10. A sample tube similar to Fig. 6.17 was filled with 2 ml of the solvent, which was degassed by three times freezing, evacuating and thawing. Afterwards, xenon gas with a pressure of 1 bar was admitted to the solution by four different methods for a time of 4 min:

1. Diffusion, i.e. just waiting. (A)
2. Vigorous shaking. (A)
3. Bubbling the gas through the solvent with a small pipette. (B)
4. Flowing the gas through a membrane loop in the solvent (similar to Fig. 6.17). (C)

Subsequently, the solution was shock frozen in a dry ice/acetone bath with a temperature of -78°C. At this temperature xenon is still gaseous (boiling point -108°C) and the non-dissolved gas can be easily removed. The whole system was evacuated, including the analyzing volume V_a which consists of an U-shaped pipe. The dissolved xenon was transferred into V_a by heating up the frozen solution while immersing the U-tube into liquid nitrogen (-196°C).

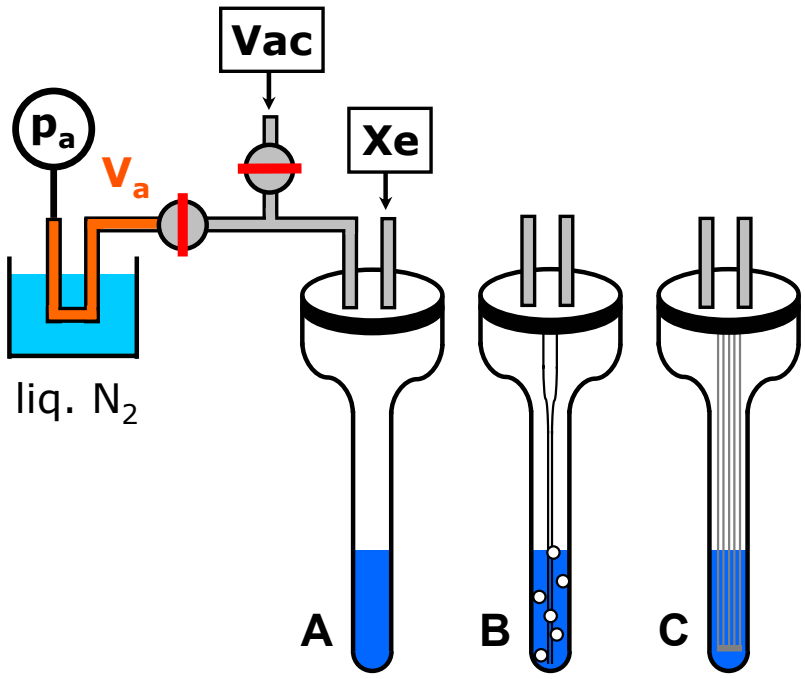

Figure 6.10: Setup to compare the efficiency of different dissolution methods by partial pressure analysis. **A:** Setup for diffusion and shaking, **B:** Bubbling, and **C:** Membrane method.

Thus, the dissolved xenon was cryopumped from the solution into V_a. The valve between V_a and the sample tube was then closed, the U-tube heated up to ambient temperature and the pressure p_a in the analyzing volume was measured. p_a is the sum of two partial pressures: one component p_a^{Xe} resides from the xenon partial pressure in the solution, while the other addend p_a^{sol} arises from the vapor pressure of the solvent. Therefore, for each measuring point the whole procedure was repeated without the admission of xenon gas to determine p_a^{sol} alone. The obtained value was subtracted from p_a to obtain p_a^{Xe}. The theoretical maximum partial pressure of a dissolved gas in a saturated solution can be calculated by the Ostwald solubility coefficient L. This coefficient is derived from the volume, at standard temperature and pressure, of a gas that can be dissolved in 1 l of liquid at 1 atm of gas pressure. It can also be expressed by the ratio of the partial pressure of a substance in the gas phase p_{gas} to the partial pressure of a saturated solution p_{dis} in

thermal equilibrium:

$$L = p_{dis}/p_{gas} \ . \tag{6.1}$$

As the volumes V_a and the solvent volume V_{liq} are known, the maximum obtainable value for p_a^{Xe} can be calculated by

$$p_a^{Xe,max} = \frac{L p_{gas} V_{liq}}{V_a} \ . \tag{6.2}$$

The measurements were accomplished for water and Lipofundin with Ostwald solubilities of $L_{H_2O} = 0.11$ and $L_{Lipo} = 0.4$ [Goodson 99]. The measured values and the calculated theoretical maxima are presented in table 6.1. All

Method	p_a^{Xe}(Lipofundin)	p_a^{Xe}(H_2O)
Diffusion	8 mbar	7 mbar
Shaking	227 mbar	60 mbar
Bubbling	85 mbar	69 mbar
Membrane	262 mbar	40 mbar
Theoretical maximum	277 mbar	76 mbar

Table 6.1: Comparison of measured xenon pressures in analyzing volume for different dissolution methods and maximum theoretical value assuming saturated solutions. The experimental error is about ± 5 mbar for each value.

values were at least measured twice to check the reproducibility and to calculate a mean value. Still, the experimental error is up to 70% for the smallest values, so that only qualitative conclusions might be drawn from these measurements.

For Lipofundin, the membrane technique comes closest to the maximum value, while shaking and especially bubbling are less effective. In water, the membrane approach transports less xenon into the solution than shaking and bubbling, however it is still much more effective than the diffusion approach. However, the membrane value in water bears a larger experimental error than all others, as the volume expansion of ice during freezing leads to small gas cavities between the membrane bundles, which could not be evacuated. Therefore, the measured values were much bigger than the theoretical maximum value. To avoid this error, the membrane loop was removed before

freezing the solution. Thereby, a certain amount of solvent was lost, which could not be really quantified, leading to a too small pressure value. The diffusion method transfers only a very small amount of gas into the liquid for both solvents and poses no real option for the gas dissolution at all.

In conclusion, these measurements showed that the xenon concentration in solution achieved by the membrane method is comparable to the used methods of shaking and bubbling, while being much more practical and without physical disturbance. This result is in good agreement with the observations reported in [Baumer 06a].

6.4 Applications in ^{129}Xe MRI

6.4.1 Experimental details

A new prototype for HP ^{129}Xe dissolution was developed to test the abilities of the membrane method in real clinical MRI applications (see Fig. 6.11). In comparison to the first prototype in Fig. 6.6, larger oxygenator modules were used to increase the efficiency of the dissolution process (Liqui-Cel® 1.7 x 5.5 Mini-Module®, Membrana GmbH, Wuppertal, Germany). These

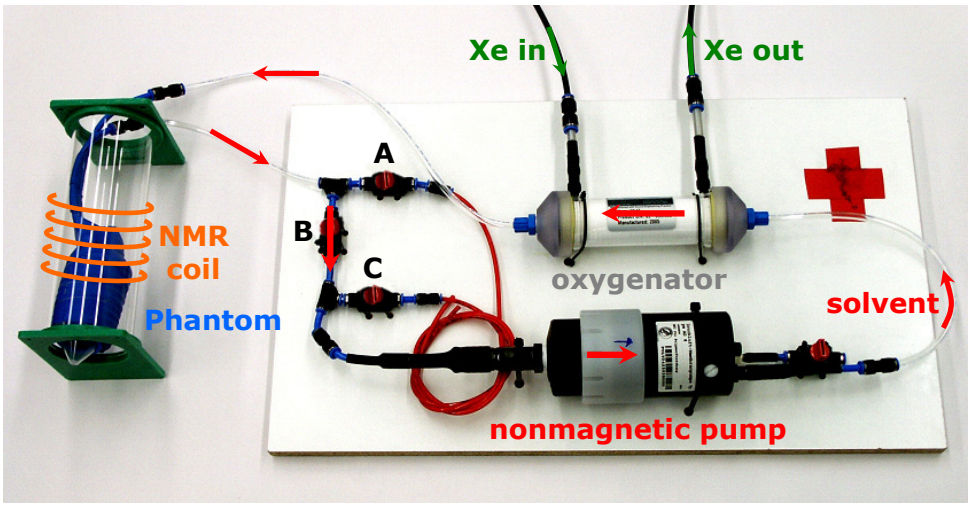

Figure 6.11: Improved setup for production of polarized xenon liquids as clinical contrast agents. Further description see text.

modules can hold up to a maximum gas pressure of 4 bar. The pressure of the gas mixture leaving the polarizer was reduced therefore to 2–3 bar by two successive hose clamps. The whole setup was mounted onto a solid support to ease transport and handling. The filling procedure of the system was simplified by usage of the valves A, B and C. The liquid was filled into the system through the red tubing connected to C while B is closed and A opened to serve as an outlet. The liquid was pumped through the cycle until all remaining air bubbles were removed. Then, A and C were closed and B was opened to have a closed cycle. For first calibration and test experiments the solvent was pumped through a phantom inside of the NMR coil. In later applications, the liquid was cycled for a certain time through the oxygenator, until the solution was saturated with HP ^{129}Xe, then it was extracted into a syringe through valve A for immediate injection.

6.4.2 ^{129}Xe spectroscopy in the clinical scanner

As the experiments in Section 6.2 showed, the most promising candidate from the few available and approved biocompatible carrier liquids of HP ^{129}Xe is Lipofundin®. Therefore, it was used for all experiments in the clinical scanner.

Three different simple one pulse NMR spectra were acquired to check the experiment setup and the proper functioning of the polarizer, scanner and dissolution method. The spectra are shown in Fig. 6.12 and were all measured within 100 scans. First, gaseous xenon was flown continuously through a single tube in the NMR coil, leading to a single peak which served as a chemical shift reference at 0 ppm for the other measurements (see Fig. 6.12 A). The gas tube was directly connected to the outlet of the polarizer without any pressure reduction.

Second, the HP ^{129}Xe was dissolved into Lipofundin by the setup shown in Fig. 6.11 and the liquid was cycled through the NMR coil. The spectrum in Fig. 6.12 B features two signals at different chemical shifts: One at about 200 ppm, corresponding to the dissolved xenon, and one at 0 ppm, due to an additional gas tube connected to the gas outlet of the oxygenator module. The gas peak splits up into two different signals, which could be due to the different environment of gas inside the lumen of the membrane fibers and gas inside of the membrane pores.

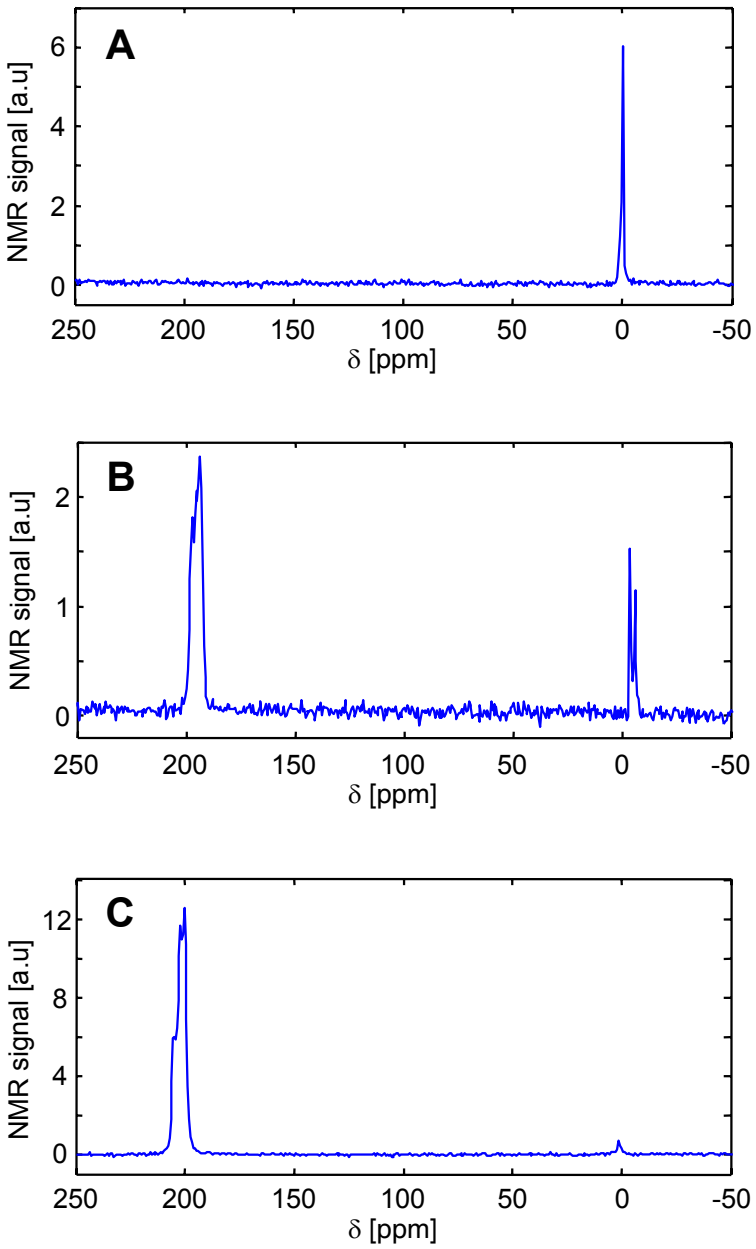

Figure 6.12: ^{129}Xe spectra acquired in a clinical scanner with a frequency of 17.59 MHz within 100 scans. **A:** Spectrum of a single gas tube; **B:** Spectrum of two tubes, one containing ^{129}Xe dissolved in Lipofundin and one gaseous xenon as a reference; **C:** Spectrum of a single tube with ^{129}Xe dissolved in Lipofundin.

For the third spectrum the gas tube was removed from the NMR coil and the signal of gaseous ^{129}Xe vanished almost completely (see Fig. 6.12 C). This means, that almost no gaseous xenon is passing the membranes and no gas bubbles are contained in the liquid. The small remaining signal at 0 ppm could be further reduced by an even more careful filling procedure. The amplitude of the dissolved signal is larger than for the previous experiment as this spectrum was measured with a larger flip angle. A nutation spectrum of the signal to calibrate the flip angle dependence could not be recorded correctly, because the r.f. pulse amplitude and length was restricted by the hardware of the scanner and only pulses with a flip angle of less than 90° could be accomplished.

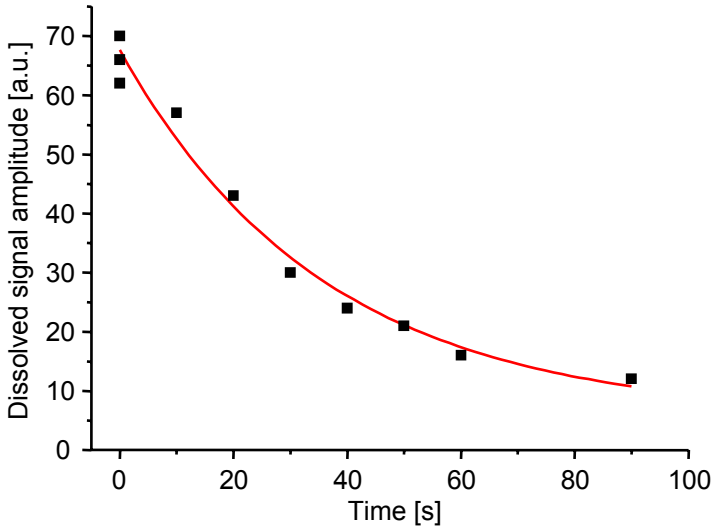

Figure 6.13: Relaxation of ^{129}Xe magnetization in Lipofundin at a field of 1.49 T. The red line shows the exponential fit of the data with a time constant of (36 ± 7) s.

The T_1 relaxation time of the dissolved ^{129}Xe was measured also for this setup, as a field dependence of the relaxation was assumed in [Goodson 99]. The experiment was conducted following the same procedure as already described in Section 6.2. The intensity of the dissolved ^{129}Xe signal depends on the waiting time before starting the measurement, as shown in Fig. 6.13.

An exponential decay function is fitted to the acquired data with a time constant of $T_1 = (36 \pm 7)$ s. This value agrees with the obtained value at

higher fields of 4.67 T of $T_1 = (43 \pm 2)$ s within the range of the experimental error, and lies in the same range as the ones reported in [Goodson 99], namely $T_1 = 40$ s at 9.4 T and $T_1 = 49$ s at 4.7 T. Although the relaxation time is shorter for the field of the used scanner, it is still long enough for clinical applications of this method.

6.4.3 First images using membrane method

First, in vitro images of HP ^{129}Xe solutions were acquired to check the feasibility of the membrane dissolution method in real clinical applications, and for comparison with the conventional shaking approach for gas dissolution. The setup for the first experiment is shown in Fig. 6.11. The phantom consists of two layers of PE hose (OD 6 mm), which are wound one over the other on a cylindrical support with an outer diameter of 50 mm (see Fig. 6.14 A). The liquid is cycled from the membrane module through the phantom inside of the solenoid coil (setup see Fig. 3.1) while the image is taken. Fig. 6.14 B depicts a projection image of the phantom acquired within an experiment time of 256 s. The two different layers of tubing are pictured nicely, the outer layer with a higher intensity, as the freshly polarized ^{129}Xe enters the

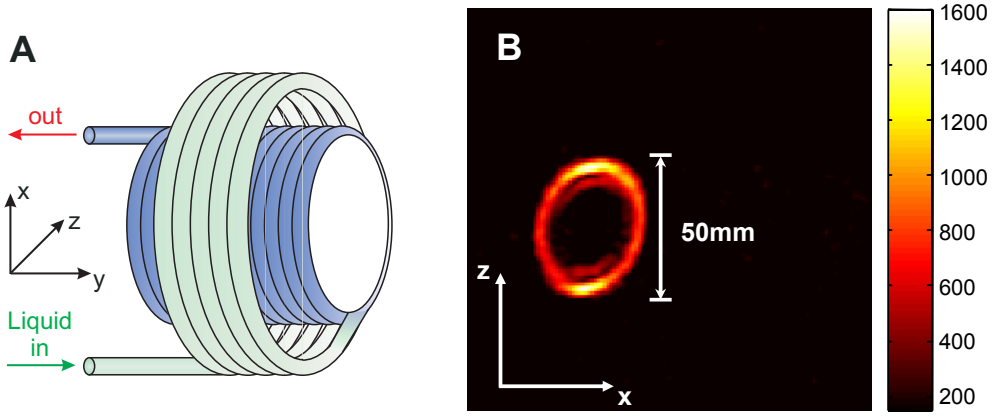

Figure 6.14: **A:** Sketch of phantom consisting of two layers of wound tube on top of each other which is flown by HP ^{129}Xe dissolved in Lipofundin. **B:** Projection image of the phantom in the xz plane. The image is taken during liquid flow with a FLASH sequence and the parameters: FOV 200 mm, 64x64 pixels, TR 1 s, NS 4, SNR 24.0.

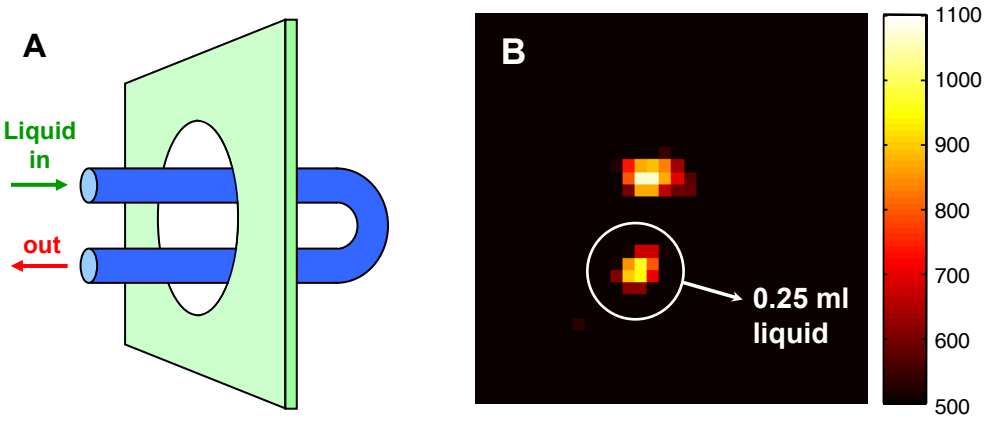

Figure 6.15: A: Only two narrow slices of the tubes are excited by the RF pulses. **B:** Obtained FLASH image of the tubes filled with ^{129}Xe dissolved in Lipofundin. Imaging parameters: FOV 100 mm, 16x16 pixels,TR 100 ms, NS 2, SNR of 5.5.

phantom there. When the liquid arrives at the inner windings, it is already depolarized to a certain amount by the RF pulses. Because this effect is only due to the flow of the liquid during the experiment, it does not occur in images where the liquid is stopped during the imaging sequence. These images are not shown here, as they feature a much worse SNR and resolution. However, the general feasibility and the achievable resolution of our method were shown by the acquired image.

Images of very small amounts of liquid were obtained using the surface coil shown in Fig. 3.2. A loop of the solvent bearing tube was fed through the coil so that approximately two straight sections of the tube are in the active region of the coil (see Fig. 6.15 A). The B_1 field of the coil excites only spins in a cylindrical volume with a diameter of 30 mm and a width of about 20 mm. Consequently, only about 0.25 ml of liquid volume are excited by the RF pulses in each tube. The liquid was cycled for about 10 s to dissolve HP ^{129}Xe, then the flow was stopped and the image was acquired. To increase the amount of xenon in the solution, a gas mixture with a fraction of 16% xenon was polarized. The image in Fig. 6.15 B shows that both tubes can be well distinguished. This means that also quite small amounts of carrier liquids can be detected. The imaged liquid volume is only one tenth of the amount of contrast agent, which is usually used in small

animal studies without the danger to cause a fat embolism. Therefore, such experiments should be feasible with the developed membrane method.

In order to apply the membrane method in in vivo experiments, the solvent has to be extracted from the membrane system into a syringe and injected into the object of interest to serve as a contrast agent. A reassuring step before performing such experiments is to image the syringe containing the extracted carrier liquid. If this image can be recorded with a reasonable SNR, one can assume that in vivo images are also feasible. Images of the syringe were acquired using the membrane dissolution method as well as the conventional shaking technique. To have equal conditions, pure HP xenon gas was used for both approaches, which was accumulated in a glass vessel by running the polarizer in the batch mode.

For the membrane dissolution approach, the xenon reservoir was attached directly to the previously evacuated gas volume of the oxygenator. After the membrane module was filled with HP ^{129}Xe gas, the liquid was cycled for about 10 s, then the flow was stopped and the solvent was extracted into the syringe, which was put into the coil as fast as possible (about 10 s after the cycling was stopped). Subsequently, the imaging sequence was started. Fig. 6.16 A shows the obtained projection image.

In order to dissolve the xenon gas by the shaking technique, the xenon reservoir was attached to another evacuated vessel containing 10 ml of Lipofundin. The xenon gas was then transferred into the solvent by thoroughly shaking the glass container. Afterwards, the liquid was extracted into a syringe and immediately put into the imaging coil. This solvent transfer was accomplished through valves and tubes similar to the ones used for the membrane method. This whole procedure took up to 30 s longer than the membrane technique, the obtained image is presented in Fig. 6.16 B.

Both images picture clearly the round shape of the syringe. The image is stretched a little bit along the y-direction because the syringe was not perfectly aligned in the coil, which leads to this distortion in the projection image. For comparison of the two different techniques, the maximum SNR of the images was determined and normalized on the magnetization of the HP ^{129}Xe gas. Therefore, a FID of the glass vessel with a small flip angle was measured in advance of the dissolution procedure. The integrated NMR signal was taken as a measure for the relative polarization of the gas. Includ-

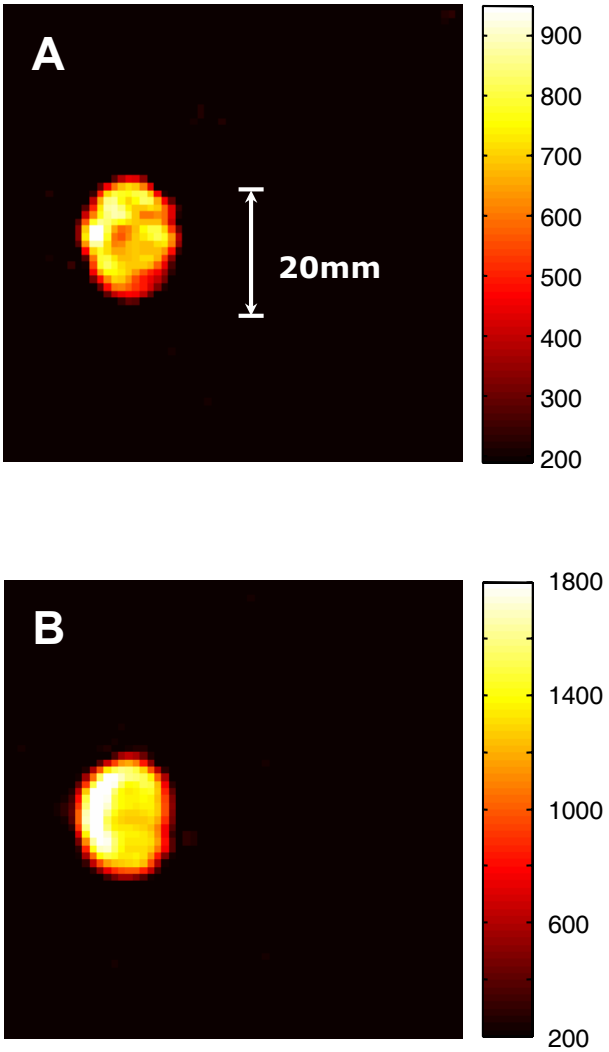

Figure 6.16: FLASH images of a syringe filled with 5 ml Lipofundin containing dissolved HP ^{129}Xe. Imaging parameters: FOV 100 mm, 32x32 pixels, TR 100 ms, NS 2. **A:** Gas dissolved by membrane method. Preparation time 10 s, SNR 12.7. **B:** Gas dissolved by shaking technique. Preparation time 40 s, SNR 23.4.

ing this normalization, the maximum SNR of the image acquired with the shaking approach exceeds the one taken with the membrane technique about a factor of 2.8. Another comparison from similar measurements revealed a factor of 2.3. From these two results, it can be concluded, that up to now the membrane technique achieves about 30–50% of the maximum signal amplitude in clinical application, in comparison to the conventional technique. This percentage can be further increased by several possible improvements in the experimental setup. The dissolution efficiency could be enhanced by using multiple oxygenator modules in a row or by an additional module to degas the solvent, which is another application of the membrane modules besides oxygenation. If the depolarized ^{129}Xe was removed from the liquid cycle, it could absorb more freshly polarized gas. These ideas are subjects of current work to perfect the dissolution procedure before conducting in vivo experiments.

6.5 Enhancing ^{129}Xe NMR spectroscopy

6.5.1 Improved setup for spectroscopy

Applications of dissolved HP ^{129}Xe are not restricted to contrast agents in MRI alone. Therefore, we developed a continuous flow system based on the membrane dissolution technique, which preserves the spectral resolution without the need of interrupting the flow to perform ^{129}Xe NMR spectroscopy experiments. The polarized xenon coming from the polarizer is transferred into the solution through a membrane loop inside of an NMR tube. At the used flow rates for the gas mixture of about 250 ml per minute, it took ca. 2 min for the polarized gas to cover the distance between polarizing cell and the NMR tube. A schematic view of the principle is shown in Fig. 6.17 A. In the constructed device about 50 CELGARD® membrane fibers were bundled and arranged inside a 10 mm NMR tube to form a loop (see Fig. 6.17 B). One end of a membrane bundle is divided into two threads, which are sealed into a 6 mm OD polyurethane tubing. The other end of the bundle is sealed in a small cap, in which a hollow space is left to allow the inversion of the gas flow. The two tubings are glued into a PVC flange and connected to the gas outlet of the polariser. The membrane part and the NMR tube are held together by a nonmagnetic clamp. By this means, the whole setup is leak-tight up to a pressure of 8 bar. Therefore, the gas mixture leaving the polarizer can be fed directly into the sample volume without any pressure reduction, which usually leads to a loss of polarization and signal.

Another problem, which often arises during gas dissolution in systems of interest for NMR spectroscopy (e.g. solutions of amphiphilic molecules, proteins, etc.), is the formation of stable foams. Our method also circumvents this problem, because the gases are dissolved in the liquids in a more "direct way". This is because the gas is diffusing continuously through the nanopores of the membrane into the liquid without bubbling, shaking or other mechanical disturbances. In order to demonstrate the capabilities of our new approach, we have studied HP ^{129}Xe in water, DMSO, and a solution containing phospholipid bicelles used in high resolution NMR studies of proteins [Baumer 03], which is particularly prone to foam formation.

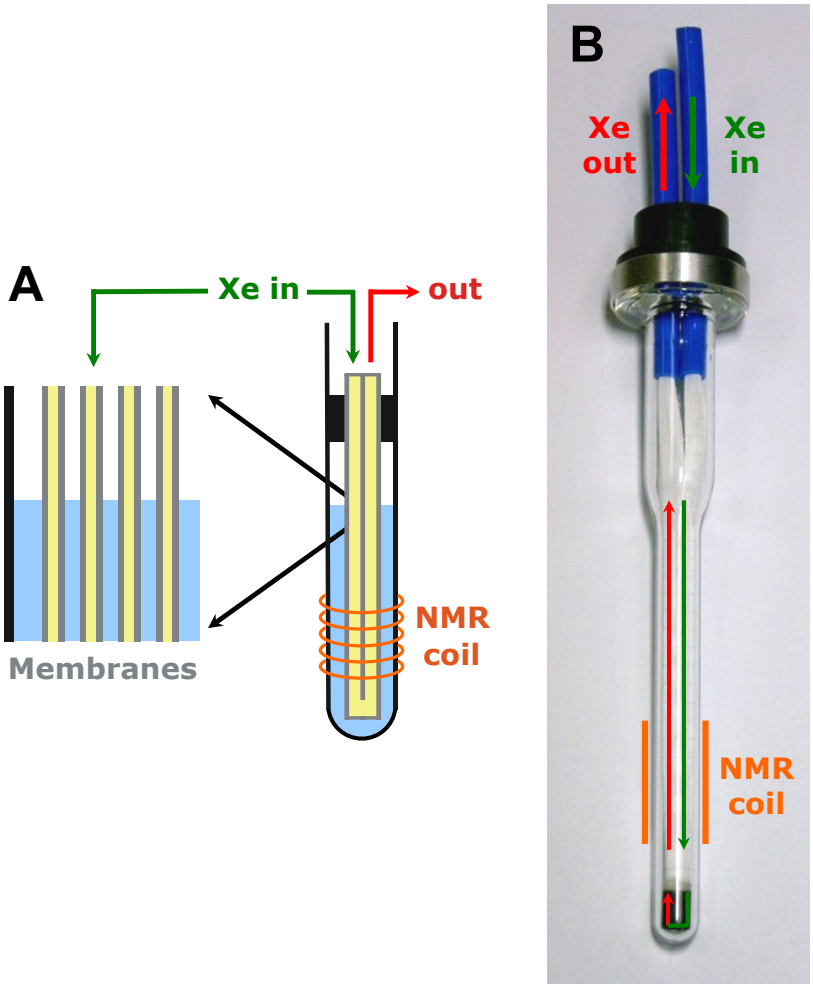

Figure 6.17: Improved setup for membrane dissolution technique inside of a NMR tube. **A:** Schematic view of the approach. The gas flows through the membrane bundle and dissolves into the solvent of interest. **B:** Membrane device for continuous gas dissolution during NMR experiments, leak tight up to 8 bar.

6.5.2 Proof of principle in H_2O and DMSO

Fig. 6.18 shows two simple NMR spectra obtained with the new developed setup of ^{129}Xe dissolved in pure water (top) and in DMSO (bottom). The measurements were conducted within two scans with a flip angle of 90° leading to a measurement time of only 2 s. The line width of the signals belonging to the dissolved xenon is only 0.3 to 0.4 ppm (insets of Fig. 6.18), allowing chemical shift measurements with an accuracy of 0.03 to 0.04 ppm. The gas peaks on the right hand side of the spectra originate from the rapidly diffusing gas inside the heterogeneous physical environment (membrane/free gas) of the hollow fibers. Therefore, they are much broader than the signals of the dissolved ^{129}Xe. As in the experiments before (see Section 6.2), no gaseous xenon passes the membranes and no gas bubbles are contained in the liquid. The signal residing from gaseous xenon inside of the hollow membranes is used for internal referencing of the spectra. A chemical shift of 0.12 ppm is

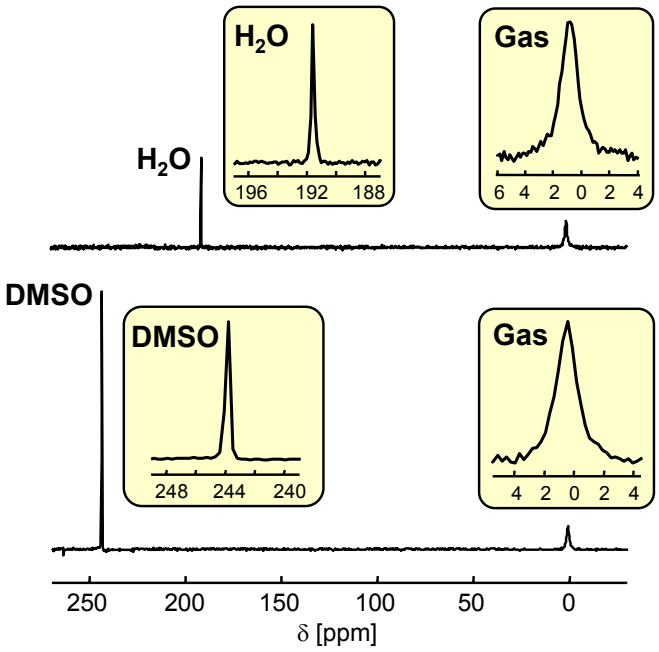

Figure 6.18: ^{129}Xe NMR spectra of HP ^{129}Xe dissolved in H_2O (top) and DMSO (bottom) obtained with two scans at T = 298 K. Chemical shifts are referenced to the gas signal. The line width of the signals is given in the insets.

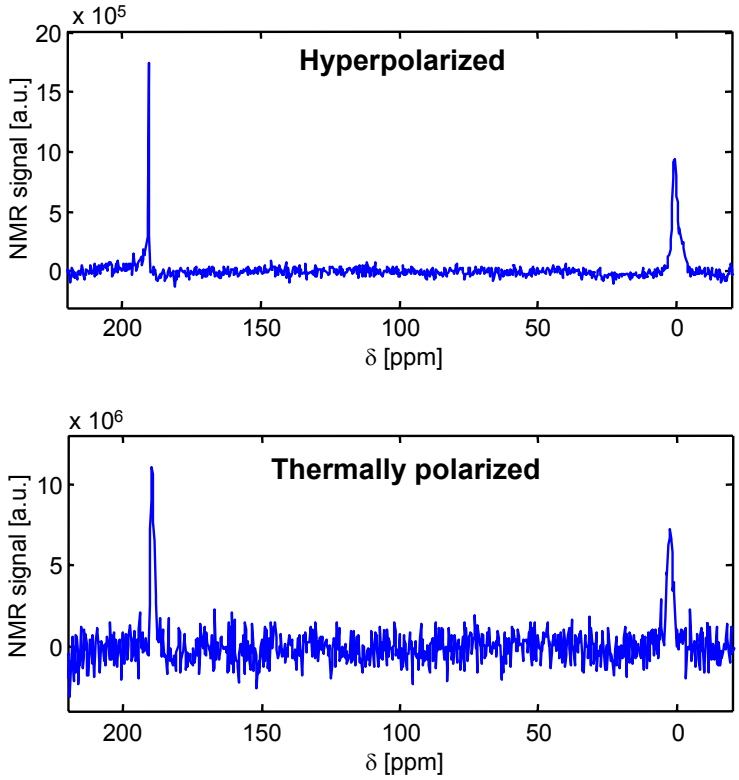

Figure 6.19: ^{129}Xe NMR spectra of xenon dissolved in H_2O to determine the polarization of dissolved and gaseous ^{129}Xe. **Top:** Acquired with HP ^{129}Xe within two scans. **Bottom:** Recorded with thermally polarized xenon in equilibrium with the solvent within 1488 scans.

expected at a xenon partial pressure of 0.03 MPa [Jameson 73, Baumer 03]. The influence of helium and nitrogen in the gas mixture is negligible as it was shown in [Jameson 70] and from measurements in the following section.

For the calculation of the ^{129}Xe polarization in the liquid and gas phase, two spectra were recorded subsequently using HP and thermally polarized ^{129}Xe. Both measurements were conducted with the same experimental settings to have equal conditions. For the thermal experiment, instead of the gas mixture, pure xenon at a pressure of 7 bar had to be used to obtain a sufficient SNR. The two spectra are compared in Fig. 6.19. The SNR obtained in the HP experiment (top) is a bit lower than in Fig. 6.18, as it was recorded at another date with slightly different shim and polarizer settings.

The thermally polarized spectrum was recorded within 1488 scans and a repetition time of 150 s, leading to a total measurement time of 62 h. Due to this long measurement time, the solution can be assumed as saturated with xenon. The ratio of the dissolved to the gas signal is the same for the HP and the thermally measurement. Two conclusions can be drawn from that: First, the assumption of saturated solutions for membrane approach is true. This also approves the results of the partial pressure analysis in Section 6.3. Secondly, no measurable loss of polarization occurs during the dissolution of the xenon gas through the pores of the membranes. This validates the assumption from the very first experiments in Section 6.2, which stated that the magnetization is conserved using the membrane technique. Other dissolution approaches, like bubbling, do not preserve the ^{129}Xe polarization during the phase transition, as reported in [Han 05].

The polarization of xenon in gas and liquid phase is calculated by the ratio of the SNR of the different signals from the following equation

$$P_{HP} = \frac{SNR_{HP} \cdot p_{th} \cdot x_{th} \cdot \sin \alpha_{th}}{SNR_{th} \cdot p_{HP} \cdot x_{HP} \cdot \sin \alpha_{HP}} \sqrt{\frac{NS_{th}}{NS_{HP}}} \cdot P_{th} \tag{6.3}$$

with P_{th} following from Eq. 2.19 as

$$P_{th} = \frac{1 - e^{-h\nu_{Xe}/k_B T}}{1 + e^{-h\nu_{Xe}/k_B T}} \quad . \tag{6.4}$$

The different quantities that determine the polarization are the pressure p, the fraction of xenon in the gas mixture x, the flip angle α and the number of scans NS. Inserting the experimental values, we obtain a polarization of (1.6 ± 0.2) % for the gas and of (1.7 ± 0.2) % for the dissolved ^{129}Xe, which is the same in the range of the experimental errors. For the experiment in Fig. 6.18, a polarization of (2.0 ± 0.2) % is calculated. This value lies within the normal range achieved in recent dissolution studies of ^{129}Xe [Hilty 06]. A further increase up to a factor of 2 can be achieved by optimization of the currently used xenon polarizer [Mühlbauer 07]. By using other polarizers especially designed for continuous flow applications, a signal improvement of up to a factor of 25 should be possible [Knagge 04, Ruset 06].

As the dissolution process occurs much faster than T_1, which is about 60 s in H_2O and 100 s in DMSO [Goodson 99], the dissolved xenon reaches the maximum possible spin polarization. The amount of needed sample is

quite small for our technique (ca. 2 ml), compared to another approach to dissolve HP ^{129}Xe for NMR spectroscopy, which was just recently reported by [Hilty 06]. Their technique produces a continuous stream of polarized liquid, which is then flown over the immobilized sample of interest. Therefore, a lot of solvent is needed, which makes the technique unsuitable for measurements where only a small amounts of solvent is available, e.g. in protein solutions. Thus, our new membrane system indeed allows biomolecular high-resolution NMR spectroscopy with continuously flowing HP ^{129}Xe. In order to demonstrate the advantages of our approach, two specific applications are shown in the following sections.

6.5.3 HP ^{129}Xe in lipid solutions

Lipid bicelles are receiving increasing interest [Li 06] from two fields of research. On one hand, they can be considered as models for biomembranes because these membranes partly consist of lipid-bilayers. On the other hand, many biomolecular NMR experiments are nowadays carried out in solutions containing lipid bicelles in order to partially orient the molecules [Tjandra 97]. When using thermally polarized xenon, one has to apply large gas pressures (up to 20 bar) to get sufficient signal intensity. However, the physically relevant parameter is the chemical shift extrapolated to zero xenon partial pressure, since this reflects the unbiased xenon-bicelle interaction. To extract this quantity with thermally polarized xenon, a set of experiments at various pressures is required to get an experimental curve, which can be extrapolated to zero pressure reliably. This is an extremely time-consuming procedure. Instead, HP ^{129}Xe offers the possibility to directly measure the chemical shift at very low xenon partial pressure (here 0.2 bar) in a single experiment.

Along these lines, we have measured the NMR chemical shift of thermally polarized ^{129}Xe in an aqueous solution of the two phospholipids DHPC/DMPC[1] as a function of the xenon pressure from 2.5 bar to 20 bar (preparation see [Baumer 06b]) and compared these measurements with the data, obtained by using HP ^{129}Xe under continuous flow at 0.2 bar (see Fig. 6.20). The measured chemical shift increases linearly with the pressure,

[1]Dimyristoyl Phosphatidylcholine/Dihexanoyl Phosphatidylcholine

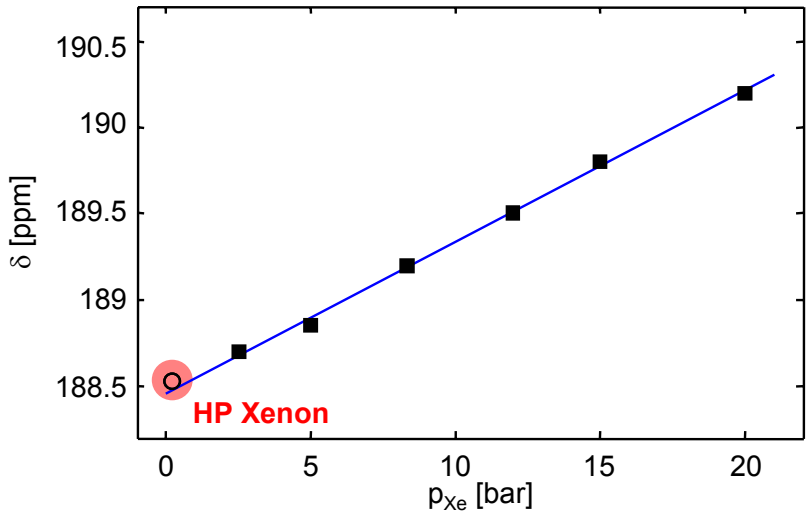

Figure 6.20: The chemical shift of ^{129}Xe versus the partial pressure at T = 308 K, measured in an aqueous DMPC/DHPC bicelle solution. The open circle indicates the measurement with HP ^{129}Xe under continuous flow using the membrane method, the other points are recorded with thermally polarized ^{129}Xe.

i.e. increasing concentration of xenon. For the ^{129}Xe chemical shift δ at 305 K we found the relationship given in Eq. 6.5, where p is the xenon partial pressure.

$$\delta\,[\text{ppm}] = 188.46 + 0.088\ p\,[\text{bar}] \tag{6.5}$$

The shift at low pressure (0.2 bar), which was measured by using HP ^{129}Xe (188.5 ppm), excellently fits into the regression line determined for the data measured in thermal equilibrium (see Fig. 6.20). This confirms the reliability and accuracy of chemical shift measurements, using HP ^{129}Xe under continuous flow in the membrane system.

Also the comparison of the chemical shifts of HP ^{129}Xe in H_2O (190.9 ppm) and in DHPC/DMPC (188.5 ppm) proves that xenon interacts with the bicelles. A chemical shift change of -2.4 ppm is induced by the lipid bicelles at 305 K. This chemical shift can be used to investigate xenon-molecule interactions and to determine specific and nonspecific interactions [Rubin 00]. The relaxation time T_1 measured for xenon in the bicelle-containing sample amounts to 40 s at 311 K. It should be noted, however, that the experiment

with HP ^{129}Xe took about 5 minutes for signal averaging only, while a single data point of the pressure dependent measurements on average took 2 hours leading to a total measurement time of about 12 hours.

6.5.4 2D ^{129}Xe exchange spectroscopy

The reduced measuring time also enables us to record two-dimensional NMR spectra [Jeener 79] for the first time under continuous flow conditions in solution. While in surface NMR, 2D exchange spectroscopy (EXSY) of adsorbed HP ^{129}Xe has become an increasingly used method [Nossov 03, Brunner 99], 2D experiments in solution were not feasible due to the low SNR and a missing, practical gas dissolution technique. By using the newly developed membrane approach, as a first example, the dissolution process of HP ^{129}Xe in H_2O could be visualized by a 2D EXSY experiment (see theory in Section 2.1.6). While usual 1D NMR experiments can only show if a gas transport is taking place in general, 2D experiments can also reveal the direction of the exchange, and quantify the dynamic timescale of the process.

The measurements were conducted with the following parameters: Flow rate of the polarized gas ca. 260 ml/min, 16 scans per evolution time step, repetition time of 1 s, 2048 points in direct dimension with a dwell time of 20 μs, 128 points in indirect dimension with a time step of 25 μs and a total experiment time of 68 min. To have constant ^{129}Xe polarization during the acquisition, polarized gas was flown through the setup for ca. 10 min before starting the measurement. In the data processing, a Gaussian filter was applied to the time domain data before the Fourier transformation. The spectrum shown in Fig. 6.21 was acquired using a mixing time of 1 ms.

The diagonal peak at ca. 0 ppm represents xenon gas in the microcapillaries, the one at ca. 190 ppm xenon dissolved in water. Apart from that, only one cross-peak is detected. This signal above the diagonal arises from xenon, that is dissolved during the mixing time of the experiment after staying in the gas phase during the evolution period. In contrast to 2D NMR spectra of thermally polarized and fully relaxed spin systems, the cross-peaks above and below the diagonal in 2D NMR spectra of hyperpolarized spins do not necessarily have identical intensity. The cross-peak below the diagonal represents xenon, which – after being dissolved during evolution – enters the gas phase during the mixing time. This cross-peak is practically invisible in

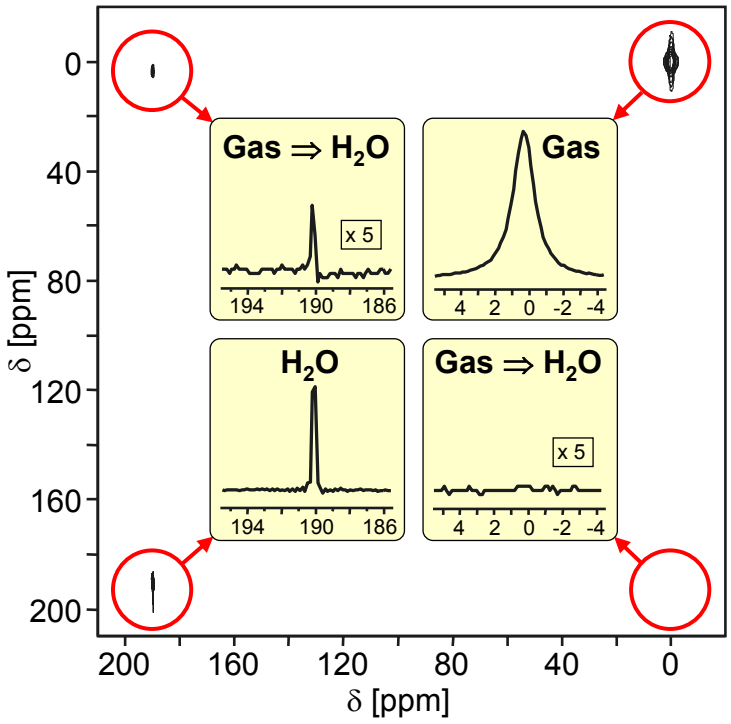

Figure 6.21: Two-dimensional EXSY spectrum (contour plot) of HP ^{129}Xe dissolved in H_2O at T = 308 K and t_{mix} = 1 ms. Experiment time is 68 min. The insets show the horizontal slices through the detected diagonal and cross peaks.

Fig. 6.21, because the NMR coil covers only a small part of the sample tube (see. Fig. 6.17 B), which leads to a high probability for this exchange outside of the detecting volume (e.g. at the water surface). Also, the time scale for this process is much longer than the used mixing time of 1 ms, as the xenon is diffusing much slower in water than in the gas phase. While the gaseous xenon in the membranes is flowing a distance in the range of millimeters during the mixing time, the dissolved xenon diffuses only about 2 μm.

These results indicate that the dissolution process happens on a timescale of milliseconds, even much faster than estimated by the measurements in Fig. 6.8, which could only limit the dissolution time to be smaller than one second. EXSY experiments with longer mixing times show other signals at

a chemical shift of ca. 30 ppm, which may be due to a metastable state of the xenon in the pores of the membranes. The dynamics of the dissolution process and also of the xenon in the membranes can be studied by varying the mixing time for different EXSY experiments. The preliminary results are not shown here, because all the experiments were conducted during continuous gas flow, which distorts the results for mixing times longer than 1 ms. As a simple calculation shows, the gas inside of the membrane fibers covers already a distance of about 1.5 mm during a time of 1 ms. During a time of 20 ms the distance is already 3.1 cm which means that all the gas which was in the fibers at the beginning of the experiment has left the NMR coil at the time of detection. Therefore, experiments with times longer than 1 ms mixing time make no sense, as they are distorted by the gas flow. Subject of current work is an experiment setup, where the gas flow is stopped during the pulse sequence in synchronization with the spectrometer. As the gas handling system and the pneumatic valves are operating already in other setups in synchronization with the pulse sequence (see description in sec. 3.5), experiments with longer mixing times should be feasible in near future.

The 2D EXSY technique of HP ^{129}Xe using the membrane method will be very useful to study systems where a slow exchange of xenon between different chemical environments happens in solution. The situation occurs, for example, in blood between the cells and the plasma [Bifone 96] or in aqueous emulsions. The accessible dynamic range covers about four orders of magnitude from 1 ms to 10 s.

6.6 Conclusions

A new method was developed to dissolve HP ^{129}Xe via commercially available, hollow fiber membranes with the following important advantages: The dissolution process is fast, reliable, and robust, without the need of special sample preparation. The new system prevents the formation of bubbles and foams. There is no observable loss of polarisation or shortening of T_1 and the continuous operation under various pressures allows signal averaging and, therefore, e.g. multidimensional NMR measurements. In addition, the membranes are stable in most liquids (water, alcohols, fat emulsions, DMSO) used as potential contrast agents in MRI or solvents in NMR spectroscopy.

That means, that the method simplifies the application of HP ^{129}Xe (or other gases with physical properties of short lifetimes) in spectroscopic methods by improving the dissolution process. Although laser-polarization increases the NMR signal sufficiently to study small concentrations of adsorbed xenon in biomolecules or host structures, applications remain rare so far with the dissolution process as the main obstacle. It was demonstrated that the proposed procedure allows the application of HP ^{129}Xe in biomolecular high-resolution NMR under continuous flow conditions at low xenon pressures. Therefore, it can also be used to record 2D NMR spectra in solution under continuous flow.

For the purpose of MRI, it was shown that the method allows the preparation of injectable contrast agents. Images of different phantoms were obtained at a clinical MRI scanner, which demonstrate the feasibility of the method in clinical applications. Hereby, small amounts of minimum 0.25 ml of contrast agent could be imaged. In comparison to the conventional dissolution approach, the membrane method is easy to control, and a SNR ratio of up to 50% of the conventional method was accomplished with a first prototype. This ratio can be further improved by different enhancements of the setup to perfect the dissolution procedure before conducting the first in vivo experiments in small animals.

Hopefully, this new method will widen the applications of hyperpolarized gases in NMR spectroscopy and medical MRI.

Chapter 7

Conclusions

In this work, different aspects of magnetic resonance, using hyperpolarized noble gases, were studied. While the first part of this thesis mainly examined new fundamental effects in NMR of *hyperpolarized* (HP) gases in theory and experiment, the second part was focused on the development of a new method for the practical dissolution of HP ^{129}Xe, with applications in medical and biological NMR spectroscopy and MRI.

Pseudo spin echoes in gases

The effect of translational diffusion on the *spin echo* (SE) formation in gases was studied for different motional regimes. It was verified, that the observed change of the SE signal in terms of amplitude, shape and maximum position arises from fast translational motion of the spins on the timescale of the NMR experiment. These signals, referred to as *pseudo SEs*, were theoretically described for linear gradients and rectangular sample shapes in the direction of the magnetic field, by an extension of the Stejskal-Tanner equation to arbitrary times. The almost perfect agreement of the calculated signals with the experimental data for different diffusion coefficients shows the validity of the extended theory. The more general case of non-linear gradients and spherical sample shapes, which cannot be solved analytically, was simulated using computer calculations.

The understanding of this strong, time-dependent diffusion suppression opens the way to different new applications, like SE sequences in MRI of HP gases or the measurement of intermolecular double quantum coherences

in gases. The effect may also be used as an alternative method for diffusion measurements in linear gradients within one scan only, by fitting the analytical calculations to the detected signal.

Intermolecular double-quantum coherences in gases

With these diffusion effects under control, for the first time *intermolecular double-quantum coherences* (iDQCs) in the gas phase were detected which arise from the *distant dipolar field* (DDF), formed by the ^{3}He spins. On the one hand, these measurements allow detailed studies of the fundamental principles of the effect. Especially the influence of the polarization and the diffusion on iDQC signals can be well examined, because these parameters can be easily changed in HP gases. The acquisition of the whole time evolution of the signal without T_2^* relaxation will also reveal new insights.

On the other hand, the high sensitivity of the iDQCs to diffusion and spatial restrictions might open the way for different new applications. As it has already been shown in liquids, iDQCs might be useful for evaluating the properties of porous samples [Bouchard 04]. In comparison to liquids, HP gases would allow the investigation of larger structures over a bigger range of pore sizes, as the dipolar coupling distance exceeds the one in liquids and can be varied easily by changing the amount of polarization. Such studies might also be useful in medical MRI, e.g. in lung imaging, particularly as further improvements of the experiment setup will allow the detection of the effect also at ambient pressures.

Solutions of HP ^{129}Xe

A new method was developed to dissolve HP ^{129}Xe via commercially available, hollow fiber membranes with the following important advantages: The dissolution process is fast, reliable, and robust, without the need of special sample preparation. The new system prevents the formation of bubbles and foams. There is no observable loss of polarisation or shortening of T_1 and the continuous operation under various pressures allows signal averaging and, therefore, e.g. multidimensional NMR spectroscopy. In addition, the membranes are stable in most liquids (water, alcohols, fat emulsions, DMSO) used as potential contrast agents in MRI or solvents in NMR spectroscopy.

That means, the method simplifies the application of HP ^{129}Xe (or other gases with physical properties of short lifetimes) in spectroscopic methods by improving the dissolution process. Although laser-polarization increases the NMR signal sufficiently to study small concentrations of adsorbed xenon in biomolecules or host structures, applications remain rare so far with the dissolution process as the main obstacle. As specific examples, the proposed procedure allows the application of HP ^{129}Xe in biomolecular high-resolution NMR at low xenon pressures, and the detection of 2D NMR spectra in solution under continuous flow to study dynamical exchange processes.

For the purpose of MRI, it was shown that the method allows the preparation of injectable contrast agents. Images of different phantoms were obtained at a clinical MRI scanner that demonstrate the feasibility of the method in clinical applications. Hereby, small amounts of minimum 0.25 ml contrast agent could be imaged. In comparison to the conventional dissolution approach, the membrane method is easy to control, and a SNR ratio of up to 50% of the conventional method was accomplished with a first prototype. This ratio will be further increased by different improvements of the setup to optimize the dissolution procedure before conducting the first in vivo experiments in small animals.

Thus, the work presented in this thesis covers both fundamental and applied aspects of magnetic resonance in HP gases, hereby combining different fields of research. Hopefully, these new techniques and experiments will widen the development and application of HP gases in NMR spectroscopy and medical MRI.

Appendix A

Spin echoes in thermally polarized ^{3}He

Here, a short estimation is given if a SE signal from a thermally polarized ^{3}He sample can be detected. Therefore, a NMR spectrum of a thermally polarized ^{3}He sample was measured within 14 scans and a repetition time of 25 min, which sums up to a total experiment time of 5 h 50 min (see Fig. A.1). As the T_1 relaxation time is in the order of minutes, such long repetition times are mandatory. The signal-to-noise ratio (SNR) here amounts to ca. 9.9. To get an idea of the estimated measurement time for a SE with similar SNR from a thermally polarized sample, we compare the SNR of a FID and a SE experiment with HP ^{3}He. For a echo time $\tau = 50$ ms, the FID signal is about 347 times larger than the SE signal. This means, that to obtain an similar SNR as in Fig. A.1 one has to measure about 1680000 scans, which would correspond to an experiment time in the order of years. This makes the detection of SE signals in thermally polarized samples impossible.

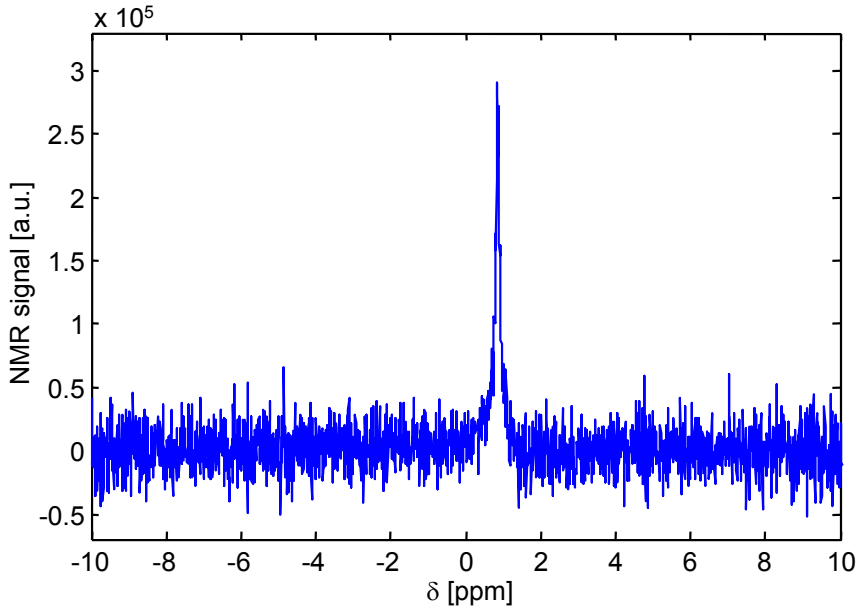

Figure A.1: Spectrum of thermally polarized ^{3}He gas at ambient pressure and temperature. Obtained within 14 scans and a time of 5 h 50 min.

Appendix B

Structure of SE simulations

The computer simulations of the diffusion suppressed SEs are implemented using the algorithm below. First of all, an ensemble of n "pseudo-particles" with an initial spin phase distribution (usually phase $\phi = 0$ for all particles) is initialized. The particles are randomly distributed in a given geometry (cylindrical or spherical), which is characterized by z_{min} and z_{max} or R respectively. For each time step dt of the simulation, the new positions of all particles are obtained, using a Gaussian distribution with the width $\sqrt{2Ddt}$ according to free diffusion (see Eq. 2.59), and the accumulated phases during dt are calculated for each particle. The whole magnetization, which corresponds to the detected NMR signal, is given by the sum over the phases of all particles for each time step. At time $t = \tau$, all phases are inverted to resemble the effect of the 180° pulse. Afterwards, the simulation continues as before until the maximum simulation time is reached.

```
Initialize ensemble(n_particles, initial_phases, zmin, zmax)
While time < tau{
    for n = 1 to n_particles{
        dz = draw_random_gaussian(Diff,dt)
        move_particle(n,dz)
        calc_phase(n,z,dz,dt)
    }
    M(time) = sum_up_phases(ensemble)
    time = time + dt
}
invert_all_phases(ensemble)
While time < time_max{
```

```
    for n = 1 to n_particles{
        dz = draw_random_gaussian(Diff,dt)
        move_particle(n,dz)
        calc_phase(n,z,dz,dt)
    }
    M(time) = sum_up_phases(ensemble)
    time = time + dt
}
```

Bibliography

[Abragam 61] A. Abragam. Principles of Nuclear Magnetism. Clarendon Press, Oxford (1961).

[Abragam 78] A. Abragam, M. Goldman. Principles of Dynamic Nuclear Polarisation. *Reports on Progress in Physics* **41**(3), 395–467 (1978).

[Acosta 06a] R. H. Acosta, L. Agulles-Pedrós, S. Komin, D. Sebastiani, H. W. Spiess, P. Blümler. Diffusion in binary gas mixtures studied by NMR of hyperpolarized gases and moelcular dynamics simulations. *Physical Chemistry Chemical Physics* **8**, 4182–4188 (2006).

[Acosta 06b] R. H. Acosta, P. Blümler, L. Agulles-Pedrós, A. E. Morbach, J. Schmiedeskamp, A. Herweling, U. Wolf, A. Scholz, W. G. Schreiber, W. Heil, M. Thelen, H. W. Spiess. Controlling Diffusion of ^{3}He by Buffer Gases: A Structural Contrast Agent in Lung MRI. *Journal of Magnetic Resonance Imaging* **24**, 1291–1297 (2006).

[Agulles-Pedró 04] L. Agulles-Pedrós. Influence of Diffusion on Contrast and Sensitivity in MRI of Gases. Diplomarbeit, Johannes Gutenberg-Universität Mainz (2004).

[Albert 94] M. S. Albert, G. D. Cates, B. Driehuys, W. Happer, B. Saam, C. S. Springer Jr., A. Wishnia. Biological magnetic resonance imaging using laser-polarized ^{129}Xe. *Nature* **370**, 199–201 (1994).

[Albert 00] Mitchell S. Albert, Dilip Balamore, Daniel F. Kacher, Arvind K. Venkatesh, Ferenc A. Jolesz. Hyperpolarized

^{129}Xe T_1 in oxygenated and deoxygenated blood. *NMR in Biomedicine* **13**, 407–414 (2000).

[Appelt 98] S. Appelt, A. Ben-Amar Baranga, C. J. Erickson, M. V. Romalis, A. R. Young, W. Happer. Theory of Spin-Exchange Optical Pumping of ^{3}He and ^{129}Xe. *Physical Review A* **58**, 1412–1439 (1998).

[Appelt 04] S. Appelt. *From Photon Spin to Magnetic Resonance Imaging.* Habilitation, RWTH Aachen (2004).

[Ardelean 00] Ioan Ardelean, Rainer Kimmich. Diffusion measurements with the pulsed gradient nonlinear spin echo method. *Journal of Chemical Physics* **112**(12), 5275–5280 (2000).

[Aue 76] W. P. Aue, E. Bartholdi, R. R. Ernst. Two-dimensional spectroscopy. Application to nuclear magnetic resonance. *Journal of Chemical Physics* **64**(5), 2229–2246 (1976).

[Balinov 93] Balin Balinov, Bengt Jönsson, Per Linse, Olle Södermann. The NMR Self-Diffusion Method Applied to Restricted Diffusion. Simulation of Echo Attenuation from Molecules in Spheres and between Planes. *Journal of Magnetic Resonance A* **104**, 17–25 (1993).

[Barros Jr. 06] Wilson Barros Jr., John C. Gore, Daniel F. Gochberg. Simultaneous measurement of D and T_2 using the distant dipolar field. *Journal of Magnetic Resonance* **178**, 166–169 (2006).

[Batz 05] M. Batz, S. Baeßler, W. Heil, E. W. Otten, D. Rudersdorf, J. Schmiedeskamp, Y. Sobolev, M. Wolf. ^{3}He Spin Filter for Neutrons. *Journal of Research of the National Institute of Standards and Technology* **110**, 293–298 (2005).

[Baumer 03] D. Baumer, A. Fink, E. Brunner. Measurement of the ^{129}Xe NMR Chemical Shift of Supercritical Xenon. *Zeitschrift für Physikalische Chemie* **217**, 289–293 (2003).

[Baumer 06a] Daniela Baumer. *Herstellung von hyperpolarisiertem Xenon-129 und Anwendungen in der Flüssigkeits-NMR-Spektroskopie.* Dissertation, Universität Regensburg (2006).

[Baumer 06b] Daniela Baumer, Eike Brunner, Peter Blümler, Paul P. Zänker, Hans W. Spiess. NMR Spectroscopy of Laser-Polarised ^{129}Xe Under Continuous Flow: A Method To Study Aqueous Solutions of Biomolecules. *Angewandte Chemie Int. Ed.* **45**, 7282–7284 (2006).

[Becker 98] J. Becker, J. Bermuth, M. Ebert, T. Grossmann, W. Heil, D. Hofmann, H. Humblot, M. Leduc, E. W. Otten, D. Rohe, R. Surkau. Interdisciplinary Experiments with Polarized ^{3}He. *Nuclear Instruments and Methods in Physics Research A* **402**, 327–336 (1998).

[Beek 03] E. J. R. van Beek, J. Schmiedeskamp, J. M. Wild, M. N. J. Paley, F. Filbir, F. Knitz, G. H. Mills, N. Woodhouse, A. Swift, W. Heil, M. Wolf, E. W. Otten. Hyperpolarized 3-helium MR imaging of the lungs: testing the concept of a central production facility. *European Radiology* **13**, 2583–2586 (2003).

[Bifone 96] A. Bifone, Y.-Q. Song, R. Seydoux, R. E. Taylor, B. M. Goodson, T. Pietrass, T. F. Budinger, G. Navon, A. Pines. NMR of laser-polarized xenon in human blood. *Proceedings of the National Academy of Sciences* **93**, 12932–12936 (1996).

[Bloch 46] F. Bloch, W. W. Hansen, M. Packard. The Nuclear Induction Experiment. *Physical Review* **70**, 474–485 (1946).

[Blümich 00] B. Blümich. NMR Imaging of Materials. Oxford University Press (2000).

[Blümler 93] P. Blümler. *Kontrast- und Auflösungssteigerung für die NMR-Bildgebung an Polymeren.* Dissertation, Johannes Gutenberg-Universität Mainz (1993).

[Bouchard 04] Louis-S. Bouchard, Warren S. Warren. Reconstruction of porous material geometry by stochastic optimization based on bulk NMR measurements of the dipolar field. *Journal of Magnetic Resonance* **170**, 299–309 (2004).

[Bouchiat 60] M. A. Bouchiat, T. R. Carver, C. M. Varnum. Nuclear Polarization in ^{3}He Gas Induced by Optical Pumping and

Dipolar Exchange. *Physical Review Letters* **5**, 373–375 (1960).

[Brasch 83] R. C. Brasch. Work in Progress: Methods of Contrast Enhancement for NMR Imaging and Potential Applications. *Radiology* **147**, 781–788 (1983).

[Brunner 98] E. Brunner, R. Seydoux, M. Haake, A. Pines, J. A. Reimer. Surface NMR Using Laser-Polarized ^{129}Xe under Magic Angle Spinning Conditions. *Journal of Magnetic Resonance* **130**, 145–148 (1998).

[Brunner 99] Eike Brunner. Enhancement of Surface and Biological Magnetic Resonance Using Laser-Polarized Noble Gases. *Concepts in Magnetic Resonance* **11**, 313–335 (1999).

[Callaghan 91] P. T. Callaghan. Principles of Nuclear Magnetic Resonance Microscopy. Clarendon Press (1991).

[Caravan 99] P. Caravan, J. J. Ellison, T. J. McMurry, R. B. Lauffer. Gadolinium(III) Chelates as MRI Contrast Agents: Structure, Dynamics, and Applications. *Chemical Reviews* **99**, 2293–2352 (1999).

[Carr 54] H. Y. Carr, E. M. Purcell. Effects of Diffusion on Free Precession in Nuclear Magnetic Resonance Experiments. *Physical Review* **94**(3), 630–638 (1954).

[Cates 88] G. D. Cates, S. R. Schaefer, W. Happer. Relaxation of spins due to field inhomogeneities in gaseous samples at low magnetic fields and low pressures. *Physical Review A* **37**, 2877–2885 (1988).

[Chann 02] B. Chann, I. A. Nelson, L. W. Anderson, B. Driehuys, T. G. Walker. ^{129}Xe-^{129}Xe Molecular Spin Relaxation. *Physical Review Letters* **88**(11), 113201 (2002).

[Chen 01a] Zhong Chen, Shaokuan Zheng, Jianhui Zhong. Optimal RF flip angle for multiple spin-echos and iMQCs of different orders with the CRAZED pulse sequence. *Chemical Physics Letters* **347**, 143–148 (2001).

[Chen 01b] Zhong Chen, Jianhui Zhong. Unconventional diffusion behaviors of intermolecular multiple-quantum coherences in nuclear magnetic resonance. *Journal of Chemical Physics* **114**(13), 5642–5653 (2001).

[Cohen Addad 93] J. P. Cohen Addad. NMR and Fractal Properties of Polymeric Liquids and Gels. *Progress in Nuclear Magnetic Resonance Spectroscopy* **25**, 1–316 (1993).

[Colegrove 63] F. D. Colegrove, L. D. Schearer, G. K. Walters. Polarization of He^3 Gas by Optical Pumping. *Physical Review* **132**(6), 2561–2572 (1963).

[Collignon 81] J. Collignon, H. Sillescu, H. W. Spiess. Pseudo-solid echos of proton and deuteron NMR in polyethylene melts. *Colloid & Polymer Science* **259**, 220–226 (1981).

[Conradi 06] M. S. Conradi, B. T. Saam, D. A. Yablonskiy, J. C. Woods. Hyperpolarized ^{3}He and perfluorocarbon gas diffusion MRI of lungs. *Progress in Nuclear Magnetic Resonance Spectroscopy* **48**, 63–83 (2006).

[Crank 85] J. Crank. The Mathematics of Diffusion. Clarendon Press, Oxford (1985).

[Deninger 06] A. Deninger, W. Heil, E. W. Otten, M. Wolf, R. K. Kremer, A. Simon. Paramagnetic relaxation of spin polarized ^{3}He at coated glass surfaces. *European Physical Journal D* **38**, 439–443 (2006).

[Driehuys 95] B. Driehuys, G. D. Cates, W. Happer. Surface Relaxation Mechanisms of Laser-Polarized ^{129}Xe. *Physical Review Letters* **74**, 4943–4946 (1995).

[Driehuys 96] B. Driehuys, G. D. Cates, E. Miron, D. K. Walter, W. Happer. High-volume production of laser-polarized ^{129}Xe. *Applied Physics Letters* **69**(12), 1668–1670 (1996).

[Duhamel 01] Guillaume Duhamel, Philippe Choquet, Emmanuelle Grillon, Laurent Lamalle, Jean-Louis Leviel, Anne Ziegler, André Constantinesco. Xenon-129 MR Imaging and Spectroscopy of Rat Brain Using Arterial Delivery of Hyper-

polarized Xenon in a Lipid Emulsion. *Magnetic Resonance in Medicine* **46**, 208–212 (2001).

[Ebert 96] M. Ebert, T. Grossmann, W. Heil, E. W. Otten, R. Surkau, M. Thelen, M. Leduc, P. Bachert, M. V. Knopp, L. R. Schad. Nuclear magnetic resonance imaging with hyperpolarised helium-3. *The Lancet* **347**(9011), 1297–1299 (1996).

[Einstein 05] Albert Einstein. Über die von der molekularkinetischen Theorie der Wärme geforderten Bewegung von in ruhenden Flüssigkeiten suspendierten Teilchen. *Annalen der Physik* **17**, 549–560 (1905).

[Ernst 87] R. R. Ernst, G. Bodenhausen, A. Wokaun. Principles of Nuclear Magnetic Resonance in One and Two Dimensions. Clarendon Press, Oxford (1987).

[Ernst 92] R. R. Ernst. Nuclear Magnetic Resonance Fourier Transform Spectroscopy (Nobel Lecture). *Angewandte Chemie Int. Ed.* **31**(7), 805–930 (1992).

[Gamblin 65] R. L. Gamblin, T. R. Carver. Polarization and Relaxation Processes in He^3 Gas. *Physical Review* **138**(4A), A946–A960 (1965).

[Gatzke 93] M. Gatzke, G. D. Cates, B. Driehuys, D. Fox, W. Happer, B. Saam. Extraordinarily slow nuclear spin relaxation in frozen laser-polarized ^{1}29Xe. *Physical Review Letters* **70**, 690–693 (1993).

[Goodson 97] B. M. Goodson, Y.-Q. Song, R. E. Taylor, V. D. Schepkin, K. M. Brennan, G. C. Chingas, T. F. Budinger, G. Navon, A. Pines. In vivo NMR and MRI using injection delivery of laser-polarized xenon. *Proceedings of the National Academy of Sciences USA* **94**, 14725–14729 (1997).

[Goodson 99] Boyd M. Goodson. Using Injectable Carriers of Laser-Polarized Noble Gases for Enhancing NMR and MRI. *Concepts in Magnetic Resonance* **11**(4), 203–223 (1999).

[Goodson 02] Boyd M. Goodson. Nuclear Magnetic Resonance of Laser-Polarized Noble Gases in Molecules, Materials, and Organisms. *Journal of Magnetic Resonance* **155**, 157–216 (2002).

[Grossmann 00] T. Grossmann. *Realisierung der ^{3}He-Kreislaufs zur ^{3}He-Magnet-Resonanz-Tomographie.* Dissertation, Johannes Gutenberg-Universität Mainz (2000).

[Gudbjartsson 95] Hákon Gudbjartsson, Samuel Petz. NMR Diffusion Simulation Based on Conditional Random Walk. *IEEE Transactions on Medical Imaging* **14**(4), 636–642 (1995).

[Haacke 99] E. M. Haacke, R. W. Brown, M. R. Thompson, R. Venkatesan. Magnetic Resonance Imaging - Physical Principles and Sequence Design. Wiley-Liss (1999).

[Haake 97] M. Haake, A. Pines, J. A. Reimer, R. Seydoux. Surface-Enhanced NMR Using Continuous-Flow Laser-Polarized Xenon. *Journal of the American Chemical Society* **119**(11711-11712) (1997).

[Haase 86] A. Haase, J. Frahm, D. Matthaei, W. Hänicke, K.-D. Merboldt. FLASH Imaging. Rapid NRM Imaging Using Low Flip-Angle Pulses. *Journal of Magnetic Resonance* **67**, 258–266 (1986).

[Hahn 50] E. L. Hahn. Spin Echoes. *Physical Review* **80**, 580–594 (1950).

[Han 05] Song-I Han, Sandra Garcia, Thomas J. Lowery, E. Janette Ruiz, Juliette A. Seeley, Lana Chavez, David S. King, David E. Wemmer, Alexander Pines. NMR-Based Biosensing with Optimized Delivery of Polarized ^{129}Xe to Solutions. *Analytical Chemistry* **77**, 4008–4012 (2005).

[Happer 72] W. Happer. Optical Pumping. *Reviews of Modern Physics* **44**, 169–249 (1972).

[Happer 84] W. Happer, E. Miron, D. Schreiber, W. A. van Wijngaarden, X. Zeng. Polarization of the nuclear spins of noble-gas atoms by spin exchange with optically pumped alkali-metal atoms. *Physical Review A* **29**(6), 3092–3110 (1984).

[He 93] Quihong He, Wolfgang Richter, Sujatha Vathyam, Warren S. Warren. Intermolecular multiple-quantum coherences and cross correlations in solution nuclear magnetic

resonance. *Journal of Chemical Physics* **98**(9), 6779–6800 (1993).

[Hilty 06] Christian Hilty, Thomas J. Lowery, David E. Wemmer, Alexander Pines. Spectrally Resolved Magnetic Resonance Imaging of a Xenon Biosensor. *Angewandte Chemie Int. Ed.* **45**, 70–73 (2006).

[Hirschfelder 64] J. O. Hirschfelder, C. F. Curtiss, R. B. Bird. Molecular Theory of Gases and Liquids. Wiley, New York (1964).

[Jameson 70] A. K. Jameson, C. J. Jameson, H. S. Gutowsky. Density dependence of ^{129}Xe Chemical Shifts in Mixtures of Xenon and Other Gases. *Journal of Chemical Physics* **53**(6), 2310–2321 (1970).

[Jameson 73] C. J. Jameson, A. K. Jameson, S. M. Cohen. Temperature and density dependence of ^{129}Xe chemical shift in xenon gas. *Journal of Chemical Physics* **59**(8), 4540–4546 (1973).

[Jameson 88] C. J. Jameson, A. K. Jameson, J. K. Hwang. Nuclear spin relaxation by intermolecular magnetic dipole coupling in the gas phase. ^{129}Xe in oxygen. *Journal of Chemical Physics* **89**(7), 4074–4081 (1988).

[Jeener 72] J. Jeener. NMR excitation with two pulses. In Ampere International Summer School, Basko Polje, Yugoslavia (1972).

[Jeener 79] J. Jeener, B. H. Meier, P. Bachmann, R. R. Ernst. Investigation of exchange processes by two-dimensional NMR spectroscopy. *Journal of Chemical Physics* **71**(11), 4546–4553 (1979).

[Jeener 00] J. Jeener. Equivalence between the "classical" and the "Warren" approaches for the effect of long range dipolar couplings in liquid nuclear magnetic resonance. *Journal of Chemical Physics* **112**(11), 5091–5094 (2000).

[Kadlecek 05] S. J. Kadlecek, K. Emami, M. C. Fischer, M. Ishii, J. Yu, J. M. Woodburn, M. NikKhah, V. Vahdat, D. A. Lipson, J. E. Baumgardner, R. R. Rizi. Imaging physiological parameters with hyperpolarized gas MRI. *Progress in Nuclear Magnetic Resonance Spectroscopy* **47**, 187–212 (2005).

[Kampen 92] N. G. van Kampen. Stochastic Process in Physics and Chemistry. Elsevier Science B.V., Amsterdam (1992).

[Kastler 50] A. Kastler. Quelques suggestions concernant la production optique et la détection optique d'une inégalité de population des niveaux de quantification spatiale des atomes. *Journal de Physique et le Radium* **11**(6) (1950).

[Kauczor 96] H.-U. Kauczor, D. Hofmann, K.-F. Kreitner, H. Nilgens, R. Surkau, W. Heil, A. Potthast, M. V. Knopp, E. W. Otten, M. Thelen. Normal and abnormal pulmonary ventilation: visualization at hyperpolarized He-3 MR imaging. *Radiology* **201**, 564–568 (1996).

[Kauczor 98] H.-U. Kauczor, R. Surkau, T. Roberts. MRI using hyperpolarized noble gases. *European Radiology* **8**, 820–827 (1998).

[Kimmich 97] R. Kimmich. NMR - Tomography, Diffusometry, Relaxometry. Springer-Verlag, Berlin (1997).

[Kingsley 95] Peter B. Kingsley. Product Operators, Coherence Pathways, and Phase Cycling. Part III. *Concepts in Magnetic Resonance* **7**(3), 167–192 (1995).

[Knagge 04] K. Knagge, J. Prange, D. Raftery. A continuously recirculating optical pumping apparatus for high xenon polarization and surface NMR studies. *Chemical Physics Letters* **397**, 11–16 (2004).

[Landon 01] C. Landon, P. Berthault, F. Vovelle, H. Desvaux. Magnetization transfer from laser-polarized xenon to protons located in the hydrophobic cavity of the wheat nonspecific lipid transfer protein. *Protein Science* **10**, 762–770 (2001).

[Lauterbur 73] P. C. Lauterbur. Image Formation by Induced Local Interactions: Examples Employing Nuclear Magnetic Resonance. *Nature* **242**, 190–191 (1973).

[Lee 96] S. Lee, W. Richter, S. Vathyam, W. S. Warren. Quantum treatment of the effects of dipole-dipole interactions in liquid nuclear magnetic resonance. *Journal of Chemical Physics* **105**(3), 874–900 (1996).

[Levitt 96] M. H. Levitt. Demagnetization field effects in two-dimensional solution NMR. *Concepts in Magnetic Resonance* **8**(2), 77–103 (1996).

[Levitt 01] Malcom H. Levitt. Spin Dynamics:basics of nuclear magnetic resonance. John Wiley & Sons, Ltd. (2001).

[Li 06] X. Li, C. Newberry, I. Saha, P. Nikolaou, N. Whiting, B. M. Goodson. Interactions between xenon and phospholipid bicelles studied by ^{2}H/^{129}Xe/^{131}Xe NMR and optical pumping of nuclear spins. *Chemical Physics Letters* **419**, 233–239 (2006).

[Lowery 05] T. J. Lowery, M. Doucleff, E. J. Ruiz, S. M. Rubin, A. Pines, D. E. Wemmer. Distinguishing multiple chemotaxis Y protein conformations with laser-polarized ^{129}Xe NMR. *Protein Science* **14**, 848–855 (2005).

[Lynch 00] C. Lynch, J. Baum, R. Tenbrinck. Xenon Anesthesia. *Anesthesiology* **92**, 865–870 (2000).

[Mair 02] R. W. Mair, P. N. Sen, M. D. Hürlimann, S. Patz, D. G. Cory, R. L. Walsworth. The Narrow Pulse Approximation and Long Length Scale Determination in Xenon Gas Diffusion NMR Studies of Model Porous Media. *Journal of Magnetic Resonance* **156**, 202–212 (2002).

[Mansfield 77] P. Mansfield. Multi-planar image formation using NMR spin echoes. *Journal of Physics C* **10**, L55–L58 (1977).

[Marion 83] D. Marion, K. Wüthrich. Application of Phase Sensitive Two-Dimensional Correlated Spectroscopy (COSY) for Measurements of ^{1}H–^{1}H Spin-Spin Coupling Constants in Proteins. *Biochemical and Biophysical Research Communications* **113**(3), 967–974 (1983).

[Marques 05] J. P. Marques, S. Grant, S. Blackband, R. W. Bowtell. Intermolecular multiple quantum coherences at high magnetic field: The nonlinear regime. *Journal of Chemical Physics* **123**, 164311 (2005).

[Martin 97] C. C. Martin, R. F. Williams, J.-H. Gao, L. D. H. Nickerson, J. Xiong, P. T. Fox. The pharmacokinetics of hyperpolarized xenon: Implications for cerebral MRI. *Journal of Magnetic Resonance Imaging* **7**(5), 848–854 (1997).

[Meiboom 58] S. Meiboom, D. Gill. Modified Spin-Echo Method for Measuring Nuclear Relaxation Times. *Review of Scientific Instruments* **29**(8), 688–691 (1958).

[Middleton 95] H. Middleton, R. D. Black, B. Saam, G. D. Cates, G. P. Cofer, R. Guenther, W. Happer, L. W. Hedlund, G. A. Johnson, K. Juvan, J. Swartz. MR Imaging with Hyperpolarized ^{3}He Gas. *Magnetic Resonance in Medicine* **33**(2), 271–275 (1995).

[Möller 99] Harald E. Möller, Mark S. Chawla, X. Josette Chen, Bastiaan Driehuys, Laurence W. Hedlund, Charles T. Wheeler, G. Allan Johnson. Magnetic Resonance Angiography With Hyperpolarized ^{129}Xe Dissolved in a Lipid Emulsion. *Magnetic Resonance in Medicine* **41**, 1058–1064 (1999).

[Mugler III 97] J. P. Mugler III, B. Driehuys, J. R. Brookeman, G. D. Cates, S. S. Berr, R. G. Bryant, T. M. Daniel, E. E. de Lange, J. H. Downs III, C. J. Erickson, W. Happer, D. P. Hinton, N. F. Kassel, T. Maier, C. D. Phillips, B. T. Saam, K. L. Sauer, M. E. Wagshul. MR imaging and spectroscopy using hyperpolarized ^{129}Xe gas: preliminary human results. *Magnetic Resonance in Medicine* **37**(6), 809–15 (1997).

[Mühlbauer 07] Frank Mühlbauer. Polarimetrie an hyperpolarisiertem ^{129}Xenon. Diplomarbeit, Johannes Gutenberg-Universität Mainz (2007).

[Natterer 97] J. Natterer, J. Bargon. Parahydrogen Induced Polarization. *Progress in Nuclear Magnetic Resonance Spectroscopy* **31**, 293–315 (1997).

[Nossov 03] A. Nossov, F. Guenneau, M.-A. Springuel-Huet, E. Haddad, V. Montouillout, B. Knott, F. Engelke, C. Fernandez, A. Gédéon. Continuous flow hyperpolarized ^{129}Xe-MAS

NMR studies of microporous materials. *Physical Chemistry Chemical Physics* **5**, 4479–4483 (2003).

[Peled 96] S. Peled, F. A. Jolesz, C. H. Tseng, L. Nascimben, M. S. Albert, R. L. Walsworth. Determinants of tissue delivery for ^{129}Xe magnetic resonance in humans. *Magnetic Resonance in Medicine* **36**(3), 340–344 (1996).

[Purcell 46] E. M. Purcell, H. C. Torrey, R. V. Pound. Resonance Absorption by Nuclear Magnetic Moments in a Solid. *Physical Review* **69**, 37–38 (1946).

[Raftery 91] D. Raftery, H. Long, T. Meersmann, P. J. Grandinetti, L. Reven, A. Pines. High-Field NMR of Adsorbed Xenon Polarized by Laser Pumping. *Physical Review Letters* **66**, 584–587 (1991).

[Raich 04] H. Raich, P. Blümler. Design and Construction of a Dipolar Halbach Array with a Homogeneous Field from Identical Bar Magnets: NMR Mandhalas. *Concepts in Magnetic Resonance B* **23(B)**(1), 16–25 (2004).

[Rich 02] J. R. Rich, T. R. Gentile, T. B. Smith, A. K. Thompson, G. L. Jones. Spin exchange optical pumping at pressures near 1 bar for neutron spin filters. *Applied Physics Letters* **80**(12), 2210–2212 (2002).

[Richter 00] Wolfgang Richter, Warren S. Warren. Intermolecular Multiple Quantum Coherences in Liquids. *Concepts in Magnetic Resonance* **12**(6), 393–409 (2000).

[Romalis 97] M. V. Romalis, E. Miron, G. D. Cates. Pressure broadening of Rb D_1 and D_2 lines by ^{3}He, ^{4}He, N_2 and Xe: Line cores and near wings. *Physical Review A* **56**(6), 4569–4578 (1997).

[Rubin 00] S. M. Rubin, M. M. Spence, B. M. Goodson, D. E. Wemmer, A. Pines. Evidence of nonspecific surface interactions between laser-polarized xenon and myoglobin in solution. *Proceedings of the National Academy of Sciences* **97**(17), 9472–9475 (2000).

[Ruset 06] I. C. Ruset, S. Ketel, F. W. Hersman. Optical Pumping System Design for Large Production of Hyperpolarized ^{129}Xe. *Physical Review Letters* **96**, 053002 (2006).

[Saam 95] B. Saam, W. Happer, H. Middleton. Nuclear relaxation of ^{3}He in the presence of O_2. *Physical Review A* **52**, 862–865 (1995).

[Schearer 65] L. D. Schearer, G. K. Walters. Nuclear Spin-Lattice Relaxation in the Presence of Magnetic-Field Gradients. *Physical Review A* **139**, A1398–A1402 (1965).

[Schmidt 07] J. Schmidt. personal communication. Max Planck Institute for Polymer Research, Mainz (2007).

[Schmiedeskamp 04] J. Schmiedeskamp. *Weiterentwicklung einer Produktionsanlage und der Speicherungs- bzw. Transportkonzepte für hochpolarisiertes ^{3}He - Anwendungen in Kernspintomographie und physikalischer Grundlagenforschung.* Dissertation, Johannes Gutenberg-Universität Mainz (2004).

[Schmiedeskamp 06a] J. Schmiedeskamp, H.-J. Elmers, W. Heil, E. W. Otten, Yu. Sobolev, W. Kilian, H. Rinneberg, T. Sander-Thömmes, F. Seifert, J. Zimmer. Relaxation of spin polarized ^{3}He by ferromagnetic contaminants. *European Physical Journal D* **38**, 445–454 (2006).

[Schmiedeskamp 06b] J. Schmiedeskamp, W. Heil, E. W. Otten, R. K. Kremer, A. Simon, J. Zimmer. Paramagnetic relaxation of spin polarized ^{3}He at bare glass surfaces. *European Physical Journal D* **38**, 427–438 (2006).

[Shah 00] N. J. Shah, T. Ünlü, H.-P. Wegener, H. Halling, S. Appelt. Measurement of rubidium and xenon absolute polarization at high temperatures as a means of improved production of hyperpolarized ^{129}Xe. *NMR in Biomedicine* **13**, 214–219 (2000).

[Smoluchowski 06] M. von Smoluchowski. Zur kinetischen Therie der Brownschen Molekularbewegung und der Suspension. *Annalen der Physik* **326**(14), 756–780 (1906).

[Soldatov 04] D. V. Soldatov, I. L. Moudrakovski, J. A. Ripmeester. Dipeptides as Microporous Materials. *Angewandte Chemie* **116**, 6468–6471 (2004).

[Song 97] Y.-Q. Song, B. M. Goodson, R. E. Taylor, D. D. Laws, G. Navon, A. Pines. Selective Enhancement of NMR Signals for α-Cyclodextrin with Laser-Polarized Xenon. *Angewandte Chemie* **109**, 2464–2466 (1997).

[Sorensen 97] A. G. Sorensen, A. L. Tievsky, L. Ostergaard, R. M. Weisskopf, B. R. Rosen. Contrast Agents in Functional MR Imaging. *Journal of Magnetic Resonance Imaging* **7**, 47–55 (1997).

[Spiess 81] H. W. Spiess, H. Sillescu. Solid Echoes in the Slow-Motion Region. *Journal of Magnetic Resonance* **42**, 381–389 (1981).

[Spiess 83] Hans W. Spiess. Molecular dynamics of solid polymers as revealed by deuteron NMR. *Colloid & Polymer Science* **261**, 193–209 (1983).

[States 82] D. J. States, R. A. Haberkorn, D. J. Ruben. A Two-Dimensional Nuclear Overhauser Experiment with Pure Absorption in Four Quadrants. *Journal of Magnetic Resonance* **48**, 286–292 (1982).

[Stejskal 65] E. O. Stejskal, J. E. Tanner. Spin Diffusion Measurements: Spin Echoes in the Presence of a Time-dependent Field Gradient. *Journal of Chemical Physics* **42**(1), 288–292 (1965).

[Swanson 97] S. D. Swanson, M. S. Rosen, B. W. Agranoff, K. P. Coulter. Brain MRI with Laser-Polarized ^{129}Xe. *Magnetic Resonance in Medicine* **38**, 695–698 (1997).

[Tjandra 97] N. Tjandra, A. Bax. Direct Measurement of Distances and Angles in Biomolecules by NMR in a Dilute Liquid Crystalline Medium. *Science* **278**(5340), 1111–1114 (1997).

[Torrey 56] H. C. Torrey. Bloch Equations with Diffusion Terms. *Physical Review* **104**(3), 563–565 (1956).

[Tugarinov 02] V. Tugarinov, R. Muhandiram, A. Ayed, L. E. Kay. Four-Dimensional NMR Spectroscopy of a 723-Residue Protein: Chemical Shift Assignments and Secondary Structure of Malate Synthase G. *Journal of the American Chemical Society* **124**(34), 10025–10035 (2002).

[Vold 68] R. L. Vold, J. S. Waugh, M. P. Klein, D. E. Phelps. Measurement of Spin Relaxation in Complex Systems. *Journal of Chemical Physics* **48**, 3831–3832 (1968).

[Walker 97] T G. Walker, W. Happer. Spin-exchange optical pumping of noble-gas nuclei. *Reviews of Modern Physics* **69**, 629–642 (1997).

[Warren 93] Warren S. Warren, Wolfgang Richter, Amy Hamilton Andreotti, Bennett T. Farmer II. Generation of Impossible Cross-Peaks Between Bulk Water and Biomolecules in Solution NMR. *Science* **262**, 2005–2009 (1993).

[Warren 98] Warren S. Warren, Sangdoo Ahn, Marlene Mescher, Michael Garwood, Kamil Ugurbil, Wolfgang Richter, Rahim R. Rizi, Jeff Hopkins, John S. Leigh. MR Imaging Contrast Enhancement Based on Intermolecular Zero Quantum Coherences. *Science* **281**, 247–251 (1998).

[Wilke 50] C. R. Wilke. Diffusional properties of multicomponent gases. *Chemical Engineering Progress* **42**, 95–104 (1950).

[Wittenberg 86] L. J. Wittenberg, J. F. Santarius, G. L. Kulcinski. Lunar source of ^{3}He for commercial fusion power. *Fusion Technology* **10**, 167–178 (1986).

[Wolber 99] Jan Wolber, Andrea Cherubini, Andrzej S. K. Dzik-Jurasz, Martin O. Leach, Angelo Bifone. Spin-lattice relaxation of laser-polarized xenon in human blood. *Proceedings of the National Academy of Sciences* **96**, 3664–3669 (1999).

[Wolf 04] M. Wolf. *Erzeugung höchster ^{3}He Kernspinpolarisation durch metastabiles optisches Pumpen.* Dissertation, Johannes Gutenberg-Universität Mainz (2004).

[Wüthrich 03] K. Wüthrich. NMR Studies of Structure and Function of Biological Macromolecules (Nobel Lecture). *Angewandte Chemie Int. Ed.* **42**(29), 3340–3363 (2003).

[Zänker 05] Paul P. Zänker, Peter Blümler, Horst-Dieter Lemke, Detlef Krieter, Frank Wiese, Hans W. Spiess. Verfahren zum Lösen von Gasen mit kurzlebigen physikalischen Eigenschaften in einer Flüssigkeit. German patent application DE 102005026604A1 (June 2005).

[Zhong 04] Jianhui Zhong, Zhong Chen, Scott D. Kennedy. Properties and Applications of Intermolecular Dipole-dipole Interactions in Biomedical NMR. *Recent Res. Devel. Chem. Physics* **5**, 23–55 (2004).

[Zook 02] A. L. Zook, B. B. Adhyaru, C. R. Bowers. High capacity production of >65% spin polarized xenon-129 for NMR spectroscopy and imaging. *Journal of Magnetic Resonance* **159**, 175–182 (2002).